

**EXPANDING THE ROLE OF FUNCTIONAL MRI IN
REHABILITATION RESEARCH**

A Dissertation
Presented to
The Academic Faculty

by

Christopher B. Glielmi

In Partial Fulfillment
of the Requirements for the Degree
Doctor of Philosophy in
Bioengineering through the
School of Biomedical Engineering

Georgia Institute of Technology
May 2009

**EXPANDING THE ROLE OF FUNCTIONAL MRI IN
REHABILITATION RESEARCH**

Approved by:

Dr. Xiaoping Hu, Advisor
School of Biomedical Engineering
Georgia Institute of Technology
School of Medicine
Emory University

Dr. Krish Sathian
Departments of Neurology, Rehabilitation
Medicine & Psychology
Emory University
VA Rehabilitation R&D Center of
Excellence
Atlanta Veterans Affairs Medical Center

Dr. Paul Benkeser
School of Biomedical Engineering
Georgia Institute of Technology

Dr. Shella Keilholz
School of Biomedical Engineering
Georgia Institute of Technology
School of Medicine
Emory University

Dr. Ronald Schuchard
VA Rehabilitation R&D Center of
Excellence
*Atlanta Veterans Affairs Medical
Center*
Department of Neurology
Emory University

Date Approved: April 2, 2009

ACKNOWLEDGEMENTS

I would like thank my advisor, Dr. Xiaoping Hu, for his guidance and support. His encouragement of my broad research interests has enriched my graduate school experience. I am also grateful to my committee, Dr. Shella Keilholz, Dr. Paul Benkeser, Dr. Krish Sathian and Dr. Ron Schuchard for their advice throughout my dissertation research. In particular, Dr. Ron Schuchard has been a critical mentor in the field of vision rehabilitation.

I have been fortunate to work in the Biomedical Imaging Technology Center at Georgia Tech / Emory University. In particular, I would like to thank Dr. Andy James, Dr. Zhihao Li, Dr. Lei Zhou, Dr. Longchuan Li, Dr. Xiangchuan Chen, Dr. Gopi Deshpande, Dr. Li Wei, Dr. Govind Bhagavatheeshwaran, Cameron Craddock, KiSueng Choi, Steven Harris, Daniel Perez, Priya Santhanam, Alex Poplawski, Jaemin Shin, Brenda Robledo, Katrina Gourdet and Robert Smith for their support.

Throughout recent years, I have also greatly benefited from the experience and advice of former Biomedical Imaging Technology Center colleagues. I am especially grateful to Dr. Stephen LaConte, Dr. Keith Heberlein, Dr. Scott Peltier, Dr. Qin Xu, Dr. Roger Nana, Dr. Zhi Yang, Dr. Nashiely Pineda, Dr. Omar Zurkiya, Dr. Dmitriy Niyazov and Dr. Xiaodong Zhang for their guidance and advice.

I would also like to thank Dr. Chantal Kerssens, Dr. Andy Butler and Dr. Chip Epstein of Emory University, Dr. Xiaoding Zhong of Siemens Medical Solutions and Dr. Jue Zhang of Peking University for their roles in supportive and intriguing collaborations.

I am most grateful to my family, especially my mother, father, sister Jennifer, brother-in-law Howard, niece Samantha and grandparents for their support throughout my time in graduate school.

This work was supported by the National Institutes of Health (RO1EB002009), the Georgia Research Alliance and the Department of Veterans Affairs Rehabilitation R&D Service C3073R.

TABLE OF CONTENTS

| | Page |
|---|------|
| ACKNOWLEDGEMENTS | iv |
| LIST OF TABLES | ix |
| LIST OF FIGURES | x |
| LIST OF ABBREVIATIONS | xii |
| LIST OF SYMBOLS | xiv |
| SUMMARY | xvi |
| CHAPTER 1: Introduction | 1 |
| 1.1 General Introduction | 1 |
| 1.2 Statement of Thesis | 2 |
| 1.2.1 Chapter 2: Arterial Spin Labeling to Reduce fMRI Measurement Variability in Individuals with Central Visual Impairment | 3 |
| 1.2.2 Chapter 3: Estimating Cerebral Blood Volume with Expanded Vascular Space Occupancy Slice Coverage | 4 |
| 1.2.3 Chapter 4: Simultaneous Acquisition of Gradient Echo / Spin Echo BOLD and Perfusion with a Separate Labeling Coil | 4 |
| 1.3 Background | 6 |
| 1.3.1 Magnetic Resonance Imaging | 6 |
| 1.3.2 Application of fMRI to Visual Studies | 7 |
| 1.3.3 Application of fMRI to Low Vision Studies | 14 |
| 1.4 General Summary | 19 |
| CHAPTER 2: Arterial Spin Labeling to Reduce fMRI Measurement Variability in Individuals with Central Visual Impairment | 20 |
| 2.1 Introduction | 21 |
| 2.2 Methods | 23 |
| 2.2.1 Visual Specifications | 23 |
| 2.2.2 Visual Stimuli | 24 |
| 2.2.3 MRI Acquisition | 25 |
| 2.2.4 BOLD and CBF Analysis | 26 |
| 2.2.5 CMRO ₂ Estimation | 28 |
| 2.2.6 Evaluation of Treatment Effects | 29 |
| 2.2.7 Assessment of BOLD and CBF Reproducibility | 30 |
| 2.3 Results | 31 |
| 2.3.1 fMRI Results: BOLD | 31 |
| 2.3.2 fMRI Results: CBF | 34 |

| | |
|---|-----|
| 2.3.3 fMRI Results: CMRO ₂ Estimation | 36 |
| 2.3.4 Reproducibility of CBF and BOLD Signal Changes | 38 |
| 2.4 Discussion and Conclusion | 39 |
| CHAPTER 3: Estimating Cerebral Blood Volume with Expanded Vascular Space | |
| Occupancy Slice Coverage | 42 |
| 3.1 General Introduction | 43 |
| 3.2 Materials and Methods | 46 |
| 3.2.1 Modified Biophysical Model | 47 |
| 3.2.2 MRI Experiments | 49 |
| 3.2.3 Visual Stimulation | 51 |
| 3.2.4 Data Processing | 51 |
| 3.2.5 Assessment of Fitting Accuracy | 53 |
| 3.2.6 Assessment of CBF – CBV Relationship | 54 |
| 3.2.7 Estimation of CMRO ₂ | 54 |
| 3.3 Results | 59 |
| 3.4 Discussion and Conclusions | 63 |
| CHAPTER 4: Simultaneous Acquisition of Gradient Echo / Spin Echo BOLD and Perfusion with a Separate Labeling Coil | |
| 4.1 Introduction | 69 |
| 4.2 Background and Previous Developments | 75 |
| 4.2.1 Labeling Coil Design | 75 |
| 4.3 Methods | 81 |
| 4.3.1 Image Acquisition | 81 |
| 4.3.1.1 Image Acquisition: Data Quality Validation of Stand-Alone SE Sequence | 82 |
| 4.3.1.2 Image Acquisition: Simultaneous Sequence | 82 |
| 4.3.2 Visual Stimuli | 84 |
| 4.3.3 Data Analysis | 84 |
| 4.3.3.1 Preprocessing and Analysis: Stand-Alone SE Evaluation | 84 |
| 4.3.3.2 Preprocessing and Analysis: Simultaneous Sequence Evaluation | 85 |
| 4.3.4 Region of Interest (ROI) Selection: Simultaneous Sequence Data | 86 |
| 4.3.5 Assessment of Reproducibility | 86 |
| 4.3.6 Assessment of Linear Coupling | 87 |
| 4.3.7 Proximity to Large Vessels | 87 |
| 4.4 Results | 88 |
| 4.4.1 Results: Stand-Alone SE Data Validation | 88 |
| 4.4.2 Results: Simultaneous Data Validation | 91 |
| 4.4.2.1 Reproducibility Assessment | 95 |
| 4.4.2.2 Linear Coupling Assessment | 95 |
| 4.4.2.3 Proximity to Large Vessels | 97 |
| 4.5 Discussion | 99 |
| 4.5.1 Two-Coil ASL and Stand-Alone SE Sequence Data Acquisition | 99 |
| 4.5.2 Simultaneous Sequence Data Acquisition | 102 |
| 4.6 Conclusion | 105 |

| | |
|--------------------------|-----|
| CHAPTER 5: Conclusions | 107 |
| 5.1 Problem Statement | 107 |
| 5.2 Overview of Findings | 107 |
| 5.3 Future Implications | 109 |
| REFERENCES | 111 |

LIST OF TABLES

| | Page |
|---|------|
| Table 2.1: Pre-implantation visual specifications for participating subjects | 23 |
| Table 2.2: Change in suprathreshold voxel counts between scanning sessions | 33 |
| Table 2.3: Change in percent signal change between scanning sessions | 33 |
| Table 2.4: Relative changes in BOLD, CBF and CMRO ₂ | 36 |
| Table 2.5: Coefficients of variation reflect better reproducibility for CBF than BOLD | 38 |
| | |
| Table 3.1: CBF, BOLD and model results for CBV_{REST} , CBV_{ACT} , $\% \Delta CBV$, $Y_{B,ACT}$ and $R_{1,BLOOD}$ | 62 |
| Table 3.2: Relative changes in CMRO ₂ using the multi-compartment model and associated M values from the single-compartment model | 63 |
| | |
| Table 4.1: Relative task-related changes and inter-subject coefficient of variation for task-related data acquired with the simultaneous sequence | 94 |
| Table 4.2: SNR and CBF_{GRAY} for stand-alone SE and simultaneous sequences | 94 |
| Table 4.3: Relative to the matched voxel localizer, CBF localizer improves linear coupling for CBF _{GE} and CBF _{SE} | 96 |
| Table 4.4: Proximity of center of gravity for CBF, GE BOLD and SE BOLD to closest large vessel | 97 |
| Table 4.5: Percent overlap of active voxels with large vessels | 99 |

LIST OF FIGURES

| | Page |
|--|------|
| Figure 2.1: CASL sequence consists of labeling time (τ) and post-labeling delay (w) prior to multislice acquisition utilizing EPI readout | 25 |
| Figure 2.2: Low vision patient exhibits variability in BOLD activation on two separate scanning sessions just days apart | 31 |
| Figure 2.3: CBF demonstrates better spatial specificity than BOLD | 34 |
| Figure 2.4: CBF and BOLD activation for low resolution checkerboard, high resolution checkerboard, small ring and large ring for 2 low vision subjects | 35 |
| Figure 2.5: Percent change for BOLD, CBF and $CMRO_2$ assuming $M=0.24$ and $CMRO_2$ estimation results over a range of M | 36 |
| Figure 2.6: Average coefficient of variation over both subjects for each stimuli and contrast | 39 |
| Figure 3.1: Multi-echo sequence acquires VASO image from first excitation and ASL and BOLD images from second excitation | 46 |
| Figure 3.2: Simulated $\Delta S/S$ for range of TI_1 and TI_1 coverage for slices 1-5 | 50 |
| Figure 3.3: An example of brain activation for the composite VASO, CBF and BOLD contrasts | 60 |
| Figure 3.4: Simulated $\Delta S/S$ for range of TI_1 and experimental points | 60 |
| Figure 3.5: Average time courses for BOLD and CBF | 62 |
| Figure 4.1: Two-coil ASL block diagram and photograph of the homebuilt DDS RF transmitter, RF power amplifier and PIN diode driver | 76 |
| Figure 4.2: Circuit diagram and photograph of labeling coil | 80 |
| Figure 4.3: Two-coil CASL stand-alone SE sequence diagram | 81 |
| Figure 4.4: Simultaneous sequence acquires CBF, GE BOLD and SE BOLD following a 3 second label and 700 ms post-label delay (w) | 83 |
| Figure 4.5: $\Delta S/S_{CONTROL}$ for resting state data acquired with stand-alone SE sequence | 89 |

| | |
|---|----|
| Figure 4.6: Activation in visual cortex from 8 Hz flashing checkerboard presented to bilateral visual field | 90 |
| Figure 4.7: Simultaneously acquired control image for CBF, GE BOLD and SE BOLD data | 90 |
| Figure 4.8: Activation for subject 4 ($p < 0.05$ corrected for FDR) for all contrasts | 92 |
| Figure 4.9: Activation for subject 4 ($p < 0.05$ corrected for FDR) for (A) CBF and matching voxel counts for (B) SE and (C) GE BOLD | 92 |
| Figure 4.10: Mean time course (across subjects) using CBF localizer | 93 |
| Figure 4.11: $\Delta S/S_{\text{CONTROL}}$ for CBF data acquired with simultaneous and stand-alone SE sequences | 95 |
| Figure 4.12: Linear coupling reflects stronger fits for CBF localizer when fitting CBF and BOLD contrasts but comparable fits for both localizers when fitting SE and GE BOLD contrasts | 96 |
| Figure 4.13: Proximity of each contrast's center of gravity to the closest large vessel | 98 |

LIST OF ABBREVIATIONS

| | |
|--------------|--|
| AMD | age-related macular degeneration |
| ASL | arterial spin labeling |
| ASR | artificial silicon retina |
| B_0 | static magnetic field strength |
| BOLD | blood oxygenation level dependent |
| CASL | continuous arterial spin labeling |
| CBF | cerebral blood flow |
| CBV | cerebral blood volume |
| CBV_{ACT} | cerebral blood volume during activation |
| CBV_{REST} | cerebral blood volume during rest |
| $CMRO_2$ | cerebral metabolic rate of oxygen |
| CV | coefficient of variation |
| ΔS | change in signal |
| DAC | digital-to-analog converter |
| DDS | direct digital synthesizer |
| DOI | diffusion optical imaging |
| EPI | echo planar imaging |
| F_{CSF} | fraction of cerebral spinal fluid |
| FDR | false discovery rate |
| fMRI | functional magnetic resonance imaging |
| FPGA | Field Programmable Gate Array |
| FWHM | full width half maximum |
| FTW | frequency tuning word |
| GE | gradient echo |
| GLM | general linear model |
| Hct | hematocrit |
| IC | integrated circuit |
| JMD | juvenile macular degeneration |
| LFP | local field potential |
| M | calibration parameter |
| MCU | microcontroller unit |
| MNI | Montreal Neurological Institute |
| MPRAGE | magnetization prepared rapid gradient echo |
| MR | magnetic resonance |
| MRI | magnetic resonance imaging |
| MSPS | mega samples per second |
| MT | magnetization transfer |
| OEF | oxygen extraction fraction |
| PASL | pulsed arterial spin labeling |
| PC | personal computer |
| PCB | printed circuit board |
| PET | positron emission tomography |
| PLL | phase-lock loop |
| PRL | preferred retinal locus |

| | |
|---------------|---|
| $R_{1,BLOOD}$ | longitudinal relaxation of blood |
| RF | radio frequency |
| ROC | receiver operator characteristic |
| ROI | region of interest |
| RP | retinitis pigmentosa |
| SE | spin echo |
| SNR | signal-to-noise ratio |
| SOC | system on chip |
| SPECT | single positron emission computed tomography |
| T1 | longitudinal relaxation time |
| T2 | transverse relaxation time |
| T2* | transverse relaxation time (including magnetic field inhomogeneity) |
| TE | echo time |
| TI | inversion time |
| TI1 | inversion time (multi-echo sequence) |
| TI2 | duration between first and second excitation pulses (multi-echo sequence) |
| TR | repetition time |
| TRL | trained retinal locus |
| TTL | transistor-transistor logic |
| ν | spiking rate per neuron |
| V1 | primary visual cortex |
| VASO | vascular space occupancy |
| $Y_{B,ACT}$ | blood oxygenation during activation |

LIST OF SYMBOLS

| | |
|--------------------------|---|
| A | labeling RF amplitude |
| α | Grubb's constant relating relative CBF and CBV changes |
| α_i | labeling efficiency |
| $Activation_{PRE_ASR1}$ | suprathreshold voxel counts in first ASR pre-implantation session |
| $Activation_{PRE_ASR2}$ | suprathreshold voxel counts in second ASR pre-implantation session |
| $Activation_{POST_ASR}$ | suprathreshold voxel counts in ASR post-implantation session |
| ATT | arterial transit time |
| β | constant reflecting the influence of deoxyhemoglobin concentration |
| B_0 | static magnetic field strength |
| C_{blood} | mL water / mL blood |
| C_{par} | mL water / mL parenchyma |
| CV_{INTRA} | intra-subject coefficient of variation |
| CV_{INTER} | inter-subject coefficient of variation |
| $\Delta CBF_{weighted}$ | CBF-weighted image intensity |
| CBV_{REST} | CBV at rest |
| $\Delta\chi$ | susceptibility difference between fully oxygenated and deoxygenated blood |
| df_1 | degrees of freedom (revised VASO model) |
| df_2 | degrees of freedom (original VASO model) |
| Δr | distance between centers of labeling coil and scanner field |
| Δx | change in water fraction of blood between rest and activation |
| ΔS | change in MRI signal |
| F | test statistic for multiple independent variables |
| f_0 | center reference frequency of the scanner |
| F_{CSF} | fraction of cerebral spinal fluid |
| $f_{labeling}$ | labeling frequency |
| FTW | frequency tuning word |
| G | labeling gradient strength |
| γ | gyromagnetic ratio |
| Hct | hematocrit |
| λ | water brain-blood partition coefficient |
| M | calibration parameter |
| $Mag(TI)$ | steady state magnetization as a function of inversion time |
| M_0 | equilibrium magnetization of the brain |
| M_a | arteriolar magnetization |
| M_t | tissue magnetization |
| M_v | venular magnetization |
| N | frequency resolution |
| N_{maps} | number of individual activation maps |
| OEF | oxygen extraction fraction |

| | |
|-------------------|--|
| Φ | inverse normal cumulative distribution function |
| P_i | p-value of map i |
| R_l | longitudinal relaxation rate |
| R_{2a}^* | arteriolar transverse relaxation rate |
| R_{2t}^* | tissue transverse relaxation rate |
| R_{2v}^* | venular transverse relaxation rate |
| $R_{2a}^{*,rest}$ | arteriolar transverse relaxation rate during rest |
| $R_{2a}^{*,act}$ | arteriolar transverse relaxation rate during activation |
| $R_{2v}^{*,rest}$ | venular transverse relaxation rate during rest |
| $R_{2v}^{*,act}$ | venular transverse relaxation rate during activation |
| $R_{2t}^{*,rest}$ | tissue transverse relaxation rate during rest |
| $R_{2t}^{*,act}$ | tissue transverse relaxation rate during activation |
| S | fMRI signal |
| σ_i | standard deviation of percent signal change across subjects |
| SS_1 | sum-of-squared error (revised VASO model) |
| SS_2 | sum-of-squared error (original VASO model) |
| $SYSCLK$ | system clock |
| τ | labeling duration |
| $T_{1,BLOOD}$ | longitudinal relaxation time of arterial blood |
| $T_{1,GRAY}$ | longitudinal relaxation time of gray matter |
| T_C | cumulative statistic |
| θ | initial phase offset of DDS |
| TI | inversion time |
| TI_1 | inversion time (multi-echo sequence) |
| TI_2 | duration between first and second excitation pulses (multi-echo sequence) |
| T_l | longitudinal relaxation of gray matter |
| v | spiking rate per neuron |
| $VASO$ | vascular space occupancy |
| w | post-label delay |
| x | water fraction of blood in voxel |
| x^{act} | water fraction of blood in voxel during activation |
| x_{avg} | mean percent signal change across subjects |
| x^{rest} | water fraction of blood in voxel during rest |
| Y_a^{act} | arterial blood oxygenation during activation |
| Y_a^{rest} | arterial blood oxygenation during rest |
| $Y_{B,ACT}$ | blood oxygenation during activation |
| Y_v^{act} | venous blood oxygenation during activation |
| Y_v^{rest} | venous blood oxygenation during rest |

SUMMARY

Functional magnetic resonance imaging (fMRI) based on blood oxygenation level dependent (BOLD) contrast has become a universal methodology in brain research. While the utilization of BOLD contrast to elucidate the human brain's functionality has gained prominence, the BOLD signal consists of a mix of physiological parameters and has relatively poor reproducibility. As fMRI becomes a prominent research tool for rehabilitation studies involving repeated measures, more quantitative and stable fMRI contrasts are needed.

Although this dissertation involves primarily healthy subjects, the methods presented relax critical assumptions that otherwise would confound utilization in patient populations. Furthermore, this work enhances relatively new fMRI measures to complement traditional approaches. These additional markers, cerebral blood flow (CBF) and cerebral blood volume (CBV) (and hence cerebral metabolic rate of oxygen (CMRO₂) modeling) are more specific imaging markers of neuronal activity than BOLD. Despite the rapid adoption of CBF and CBV in recent years, very few studies apply these measures in patient populations. Repeated measures of cortical functionality in the context of rehabilitation may be enhanced with such comprehensive estimates and associated longitudinal consistency.

The first aim of this dissertation assesses feasibility of complementing BOLD with quantitative fMRI measures in subjects with central visual impairment. While the utilities of these measures have been established in animals and healthy human subjects, they are yet to be applied to understanding pathophysiology and neural plasticity.

Second, image acquisition and analysis are developed to enhance quantitative fMRI by quantifying CBV while simultaneously acquiring CBF and BOLD images. This aim seeks to relax assumptions related to existing methods that are not suitable for patient populations. Finally, CBF acquisition using a low-cost local labeling coil, which improves image quality, is combined with simultaneous acquisition of two types of traditional BOLD contrast. This dissertation enhances CBF, CBV and CMRO₂ measures in healthy subjects. However, the motivation of this work relates to rehabilitation studies as these methodological improvements can lead to better characterization of pathophysiology and treatment effects.

CHAPTER 1

INTRODUCTION

1.1 General Introduction

In the past decade, functional magnetic resonance imaging (fMRI) based on blood oxygenation level dependent (BOLD) contrast has become the primary neuroimaging tool for rehabilitation studies. While the utilization of BOLD contrast to elucidate the human brain's functionality has gained prominence, the BOLD signal is not believed to fully correlate with actual neuronal activity. This dissertation complements BOLD fMRI with more comprehensive measures to reduce the gap between measured hemodynamics and actual neuronal activity. While the motivation for this work is to develop fMRI methods toward improved monitoring of patients with visual field impairment, most applications involve healthy subjects to demonstrate feasibility of innovative image acquisition and analysis. Despite the involvement of primarily healthy subjects, the developed methods relax critical assumptions that would confound utilization in patient populations. Furthermore, this work enhances additional measures to complement traditional fMRI experiments.

Additional quantitative measurements include cerebral blood flow (CBF) and cerebral blood volume (CBV) (and hence cerebral metabolic rate of oxygen (CMRO₂) modeling). Quantitative fMRI markers reflect physiological units as opposed to ambiguous units of BOLD and are considered to be more specific imaging markers of neuronal activity than BOLD. While CBF has been accessible through positron emission

tomography (PET) and both CBF and CBV measures have been achieved with the injection of contrast agents using MRI, recent developments have enabled noninvasive MRI acquisition of both measures without the use of injection. Simultaneous acquisition of CBF and BOLD enables CMRO₂ modeling; although CMRO₂ is not an independent measure, its estimation enables further insight to actual populations of neurons. Despite the rapid adoption of CBF and CBV in recent years, very few studies leverage these measures in patients. Repeated measures of cortical functionality in the context of rehabilitation can be enhanced with such comprehensive estimates and associated longitudinal consistency.

1.2 Statement of Thesis

This dissertation seeks to enhance the utilization of simultaneous BOLD, CBF and CBV measures (and hence CMRO₂) for future applications in elucidating pathophysiology and tracking repeated measures in healthy and rehabilitation subjects. First, feasibility of acquiring quantitative fMRI in rehabilitation subjects to complement BOLD is explored. While the utilities of these measures have been established in animals and healthy human subjects, they are yet to be applied to understanding pathophysiology and neural plasticity. Second, image acquisition and analysis are developed to enhance quantitative fMRI. This aim seeks to relax assumptions related to existing methods that are not suitable for patient populations. Finally, CBF acquisition using a low-cost local labeling coil, which improves image quality, is combined with simultaneous acquisition of two types of BOLD contrast. The accomplishment of these aims extend CBF, CBV and CMRO₂ measures in healthy subjects to potential rehabilitation participants and can lead to better characterization of pathophysiology and rehabilitation effects.

1.2.1 Chapter 2: Arterial Spin Labeling to Reduce fMRI Measurement Variability in Individuals with Central Visual Impairment

While fMRI using BOLD contrast is commonly used to assess cortical dynamics with repeated measures, quantitative methods are more reproducible and specific to neuronal dynamics. In this chapter, BOLD fMRI is applied in subjects implanted with a sub-retinal prosthesis used to treat subjects with central visual field impairment due to retinitis pigmentosa (RP). Although this is the standard approach for tracking treatment effects, variability associated with fellow eye stimulus between scanning session days and months apart suggests that actual treatment effects in the implanted eye are indistinguishable due to inherent BOLD variability. For the first time, the feasibility of arterial spin labeling (ASL) to measure CBF and estimate $CMRO_2$ to complement BOLD is explored in patients with central visual field impairment. Successful acquisition of these quantitative parameters and improved inter-scan reproducibility relative to BOLD demonstrate the promise of quantitative fMRI in this patient population. However, the inherent low sensitivity of CBF poses challenges for one subject with reduced activation in the visual cortex, underscoring the need for enhanced methodology. Improvements of quantitative fMRI are presented in Chapters 3 and 4 for eventual utilization in patient populations.

1.2.2 Chapter 3: Estimating Cerebral Blood Volume with Expanded Vascular Space Occupancy Slice Coverage

To complement CBF measurement with ASL, noninvasive CBV is commonly used to complement BOLD by quantifying the hemodynamic response. A model for quantifying CBV based on the noninvasive vascular space occupancy (VASO) technique and varying the extent of blood nulling yielding task-related signal changes with various amounts of BOLD and VASO weightings was previously described. However, this approach has been limited by reduced slice coverage and the confounding inflow of fresh blood. This chapter addresses these limitations and extends the previous model to multiple slices while accounting for the inflow effect. Furthermore, this method is applied to data from a multi-echo sequence simultaneously acquiring VASO, CBF and BOLD images. The incorporation of these simultaneous measurements will facilitate efficient image acquisition, providing a range of markers relevant to future rehabilitation studies. Furthermore, this approach does not rely on the assumption of resting CBV, an assumption that is particularly uncertain in patient populations. Finally, a new $CMRO_2$ estimation model using CBV, CBF and BOLD is described.

1.2.3 Chapter 4: Simultaneous Acquisition of Gradient Echo / Spin Echo BOLD and Perfusion with a Separate Labeling Coil

Chapter 4 complements Chapters 2 and 3 by improving CBF image quality through enhanced image acquisition. Recent advances improve low signal-to-noise ratios (SNR) of ASL by using a separate labeling coil to improve arterial labeling efficiency

and to minimize magnetization transfer (MT) effects. Previously, an inexpensive and programmable two-coil continuous arterial spin labeling (CASL) system was developed at Emory University's Biomedical Imaging Technology Center. While previous systems require the expensive magnetic resonance (MR) radio frequency (RF) instruments, this design utilizes a low-cost hardware to generate the labeling RF waveform without sacrificing RF performance. The first part of this chapter evaluates performance, ease of use and image quality for data acquired at rest and during visual stimuli.

Next, this method is enhanced by complementing two-coil ASL, which acquires superior CBF images, with simultaneous acquisition of spin echo (SE) and gradient echo (GE) BOLD contrasts. Relative to GE BOLD, SE BOLD and CBF have similar advantages including reduced bias to draining veins and better localization to intravascular space than extravascular regions. Simultaneous acquisition reduces inter-scan variability to improve evaluation of each contrast's relative specificity and reproducibility. Furthermore, it facilitates future rehabilitation studies that would benefit from complementary measures.

1.3 Background

1.3.1 Magnetic Resonance Imaging

The most significant and revolutionary advance in MRI in the past two decades occurred in the early 1990s when methods were developed for noninvasive mapping of brain function without the use of an exogenous contrast agent (1-3). The majority of fMRI experiments are based on the BOLD contrast, which is derived from the paramagnetism of deoxyhemoglobin: changes in the local concentration of deoxyhemoglobin within the brain lead to alterations in the magnetic resonance signal.

In addition to BOLD contrast with fMRI, PET and single photon emission computed tomography (SPECT) are commonly used in functional brain studies. PET and SPECT require injection of an exogenous tracer, which creates a health concern for studies involving repeated imaging sessions. On the other hand, fMRI utilizes a noninvasive endogenous tracer to measure hemodynamic correlates of neuronal activity (1). Unlike PET and SPECT, fMRI does not expose subjects to ionizing radiation and has higher spatial and temporal resolutions. Furthermore, fMRI can be used to map resting connectivity in human subjects to complement task-related activation maps (4). Both functional activation and resting connectivity can be measured using fast sequences such as echo planar imaging (EPI). The combination of fMRI's spatial and temporal resolutions and flexibility for safe repeated scanning sessions allow for more sophisticated experimental designs (5,6).

1.3.2 Application of fMRI to Visual Studies

BOLD fMRI contrast has also been the most prominent method for the study of the human visual system. However, despite its wide utilization, there are two important caveats related to this contrast. First, the BOLD signal is dependent on a combination of physiological parameters, including CBF, CBV and $CMRO_2$, and therefore produces relative, not absolute, results that vary longitudinally for reasons outside the realm of neuronal activity dynamics (7). Second, the magnitude of the signal change is largely dependent on brain vasculature because the BOLD signal originates from the venous concentration of deoxyhemoglobin (8). Therefore, the localization of “activation” is aligned more with draining veins than actual neuronal populations. Furthermore, the regional magnetic effect of deoxyhemoglobin exacerbates spatial specificity issues. Specifically, the attribute that enables BOLD contrast, paramagnetism, produces a bulk susceptibility difference between the vessels and surrounding tissue, so image voxels in extravascular space exhibit the BOLD contrast. While this improves BOLD sensitivity (a main reason for BOLD’s ease of utilization), spatial resolution of activation is not as specific as methods using other means of contrast such as CBF and CBV (8).

The empirical shortcomings of BOLD longitudinal consistency and spatial specificity have provided motivation for CBF measurement through the utilization of ASL. Initial MRI methods measuring CBF relied on contrast agents to label cerebral blood (9). However, in recent years noninvasive labeling has enabled measurement of absolute CBF values without the use of any exogenous agents. Specifically, ASL uses magnetically labeled arterial blood water as an endogenous tracer for measuring CBF

(10-19). In this method, arterial blood flowing toward the region of interest (ROI) is labeled by magnetic inversion. After a delay to allow for labeled blood to flow into the ROI, an image is acquired that depends on both the static tissue and the amount of tagged blood that has entered the slice. This “label image” is followed by a second image in which the inflowing blood is not inverted. Subtracting the label image from the control image, the resulting difference image is dependent only on blood flow and serves as a CBF-weighted image that can be used to calculate absolute CBF.

Recent extensions of CBF acquisition estimate $CMRO_2$ by assuming a uniform CBF-CBV relationship based on past empirical PET data (20). This relationship is assumed to be accurate across brain regions and species, but deviation in human physiology is possible and the applicability to pathophysiology is unknown. One study incorporated explicit CBV measurement by complementing fMRI with diffuse optical imaging (DOI) to better define the subject-specific relationship between CBF and CBV. However, DOI has several shortcomings: it requires the assumption of baseline hemoglobin concentrations from published literature for quantification, it has low spatial resolution, it may reflect responses from different volumes of tissue relative to MR observations, and it is not collected simultaneously with BOLD and CBF data acquisition (21). Still, despite drawbacks of CBV-related inaccuracies, the inclusion of CBV-weighted contrast can provide insight to the CBF-CBV relationship, particularly in patient populations.

CBV acquisition with MRI has gained prominence in recent years through efforts to acquire a more complete measure of hemodynamics. While many studies utilize

exogenous contrast agents to measure CBV, a recent technique has assessed CBV through changes in extravascular water signal without the use of contrast agents. This technique detects changes in vascular space occupancy (VASO) by acquiring images when the blood signal is selectively nulled (22). However, while VASO acquisition provides CBV-weighted signal changes between rest and activation states, it does not provide absolute CBV, which is required to model $CMRO_2$ without the assumed CBF-CBV relationship. Therefore, absolute CBV calculation based on the VASO signal generally requires the assumption of resting CBV.

Although noninvasive MRI methods generally do not yield absolute CBV, VASO signal can still augment BOLD and CBF measurements. Recently, a multi-echo sequence acquiring BOLD, CBV and VASO images from a single repetition time (TR), or MRI cycle, has enabled simultaneous acquisition of these parameters (23). The utilization of separate echo times (TE) for each of these three acquisitions optimizes each contrast, reducing the tradeoff experienced when BOLD and CBF images are generated from acquisition at a common TE. As with the traditional VASO sequence, CBV-weighted images are acquired at a very short TE when the blood signal is selectively nulled. Next, using a second excitation within the same TR, a label or control CBF image is acquired at a short TE. The third acquisition is BOLD-weighted using this second echo with acquisition at a longer TE, ensuring a $T2^*$ -weighted image with optimal BOLD contrast. On the other hand, for CBF/BOLD sequences using a single echo time, a TE must be selected that is too long for optimal CBF contrast, too short for optimal BOLD contrast, or compromised to yield suboptimal BOLD and CBF. Furthermore, the CBF/BOLD sequence makes no CBV-weighted measurement.

Although no studies to date have utilized this multi-echo sequence without the need to assume resting CBV, a recent study has expanded the singular VASO sequence (without CBF and BOLD acquisition) to quantify CBV by acquiring images at multiple inversion times (TI) to vary the extent of blood signal nulling (24). Biophysical modeling allows for decomposition of BOLD and CBV weighting to allow for empirically-derived quantification of CBV. In this study, Gu *et al.* validated this technique using visual stimuli on healthy human subjects. This recent development regarding noninvasive CBV quantification, along with established methods for BOLD and CBF imaging, provides a platform for several distinct CMRO₂ estimation techniques. Furthermore, it potentially relaxes assumptions of resting CBV or the CBF-CBV relationship that may not be valid in patient and elderly populations.

The ability to acquire BOLD and CBF noninvasively has enabled recent studies inducing hypercapnia (increased blood CO₂ levels) to calibrate CBF and BOLD measures for modeling CMRO₂, a supposed more accurate marker of neural activity than BOLD, CBF or CBV (25,26). In this technique, generally known as the simplified model, induced hypercapnia increases CBF while CMRO₂ remains constant, so the interaction of BOLD and CBF can be modeled to account for CMRO₂ during subsequent scans acquired at normocapnia (normal blood CO₂ levels). This normalization yields an empirically-derived calibration constant (M) specific to a given subject and brain region. Some studies have assumed this calibration constant based on published values to provide a general approximation of CMRO₂ (27,28). However, one recent study demonstrated that this calibration parameter should be empirically derived because it drives the calculation of CBF:CMRO₂ coupling dynamics (29). In this work, Chiarelli *et al.* used

simulated BOLD-CBF data that purposely exhibited poor neurovascular coupling. Despite this poor coupling, assuming values of M consistent with other studies led to comparable CBF:CMRO₂ ratios as those studies, demonstrating that M could have more of an effect on this ratio than the relationship between CBF and BOLD during hypercapnia.

For this reason, most studies employing MRI to model CMRO₂ calibrate empirically while acquiring CBF and BOLD data in one of three ways: (i) separately, resulting in decoupling of BOLD and CBF and increased scanning time (19); (ii) simultaneously with some tradeoff for BOLD and/or CBF acquisition (27,30); or (iii) in an interleaved fashion which optimizes CBF and BOLD results but sacrifices temporal resolution (18,31). Regardless of acquisition approach, studies using this simplified model must assume Δ CBV based on measured Δ CBF.

The uncertainty of this CBF-CBV relationship has provided motivation for a more comprehensive model which relaxes the simplified model's assumption of relative CBV based on CBF-related changes (32). Specifically, this model separates microvasculature into two compartments: arteriolar (30%) and venular (70%) and further divides BOLD signal into a third compartment for tissue. Lu *et al.* acquired CBF, BOLD and VASO images with separate sequences, leading to long experimental paradigms and the assumption that stimulus-induced changes in the visual cortex were the same during each sequence. Δ CBV is estimated from CBV-weighted changes, or Δ VASO, by assuming a resting state blood volume fraction of 4.7%. This introduces some uncertainty as resting CBV could vary within and between patient populations, and between brain regions.

Still, assuming resting CBV to estimate ΔCBV enables estimation of blood oxygenation during activation (based on the measured BOLD signal) and calculation of oxygen extraction fraction (OEF). This value is then used in conjunction with measured ΔCBF to yield CMRO_2 estimates independent of an assumed CBF-CBV relationship but dependent on assumed resting CBV.

A recent study compared the simplified and comprehensive models with positron emission tomography (PET) (33). Although PET has reduced spatial resolution relative to MRI, requires a local cyclotron, and involves injection of a radioactive tracer, which is not conducive to repetitive measures or patient populations, it is considered to be a gold standard for CMRO_2 measurement (34). This study improved upon the CMRO_2 estimation approach of Lu *et al.* (32) by using the multi-echo sequence of Yang *et al.* (23) instead of three separate acquisitions for CBF, VASO and BOLD. Although this study objectively evaluated both the simplified and comprehensive models, each model included key assumptions. Specifically, estimates from the simplified model assumed the calibration parameter extrapolated from other studies instead of inducing hypercapnia to determine subject-specific and brain region-specific calibration. The comprehensive model assumed resting CBV, which also may vary between subjects and brain regions. Despite these assumptions, this study provided a unique comparison of these methods and determined that at a range of stimulus frequencies (black and white checkerboard reversing contrast at 1-32 Hz) and stimulus durations CMRO_2 estimates from the comprehensive model were more consistent with PET results from two comparable studies.

Recent studies have shown that CMRO₂ estimation from either model provides a more comprehensive view of neuronal activity than utilization of BOLD alone. For instance, one study using parallel single unit recordings and CMRO₂ estimation (simplified model) using fMRI in the rat brain showed that CMRO₂ is more closely coupled with cortical efference, or neuronal spiking, while BOLD is dominated by afference, or local field potentials (LFPs) (25,26). Similar parallel studies in both rodents and primates have demonstrated that spiking rate per neuron (ν) is more highly correlated with stimulus-induced CMRO₂ than BOLD change (ΔS) (35,36). While it is possible that spiking rates are not consistent across species, the large variability of $\Delta S\%/\Delta \nu\%$ (within and between species) suggests that fMRI studies using BOLD contrast may be confounded by variability in BOLD's biophysical determinants (26). Another primate study also demonstrated that BOLD is more highly correlated with LFPs than neuronal spiking (37).

Although there is much debate regarding the extent to which this suggests BOLD reflects neuronal input, these findings imply that BOLD cannot necessarily be directly correlated with neuronal output (25). Δ CMRO₂ estimates, on the other hand, demonstrate a more linear correlation with Δ CBF and $\Delta \nu$ as demonstrated in anesthetized rats during forepaw stimulation (25,38,39). Furthermore, recent studies have revealed that CBF (and to a greater extent, CMRO₂) measures are more consistent over time within subjects and also between subjects (7,9,40). These results suggest that acquisition of a comprehensive array of fMRI measures including CBF, CBV and BOLD, as well as CMRO₂ estimates may be a more robust approach than BOLD alone for understanding pathophysiology and monitoring therapies.

Despite the benefits of CBF, CBV and $CMRO_2$ incorporation to pathophysiology studies, there has been no research applying these measures to patients with visual field impairment. In general, CBF and $CMRO_2$ have not been utilized for many disease pathophysiology or rehabilitation studies. Instead, BOLD contrast has been the marker of choice for such studies, largely due to its ease of use and widespread acceptance. While BOLD will continue to be an integral part of rehabilitation studies, utilization of these complementary measures will help to elucidate pathophysiology and to enable comprehensive interpretation of functional dynamics related to neuronal activity.

1.3.3 Application of fMRI to Low Vision Studies

Development of quantitative fMRI methods that are suitable to study patients with visual field impairment can help overcome BOLD limitations. One such disease, age-related macular degeneration (AMD) ranks as the major cause of visual impairment in the Western society in people over 50 years of age (41). Furthermore, approximately 12% of people aged 80 years or older in the United States have some form of AMD (42). AMD can be classified in two general forms: dry AMD, which is caused by geographic atrophy in the retinal pigment epithelium layer, and wet AMD, which results from choroidal neovascularization. This growth of new blood vessels in the choroids constitutes more serious macular degeneration than does dry AMD (43-45). AMD often results in central scotomata, or blindness related to the macula, in both eyes, corresponding to as much as 15-20 degrees in the central visual field (45).

Past studies have reported the development of a preferred retinal locus (PRL), a retinal location corresponding to a peripheral point in the visual field used as a revised fixation point to compensate for central vision loss (43,44,46,47). Patients with a central scotoma aim the eye such that the image of the visual target of interest is placed within the PRL. While the location of the PRL varies between patients, studies have reported that the PRL is often above the central scotoma located on the retina (the patient's eye aims such that the visual target of interest is below the central scotoma in the visual field) (43,44,46,47). Further complicating PRL generalizations, Whittaker *et al.* (48) suggested that patients might develop more than one PRL, particularly if the central scotoma exceeds 20 degrees of the visual field. While patients often adopt a PRL for fixation and other visual functions without explicit training, certain activities such as reading can impact PRL location. Although PRL development from attempting to read often localizes to the left of the retinal lesion (i.e. fixating to the left of the visual field scotoma), reading speed and accuracy can be significantly improved if a new trained retinal locus (TRL) is established above or below the retinal lesion (49). The variability of PRL development and optimum utilization for quality of life provides motivation to learn about the effect that PRL utilization can have on visual processing. Increased understanding of PRL development and utilization will provide a more stable foundation for rehabilitation practices. Furthermore, current behavioral measures do not provide insight about the point of breakdown when PRL adoption does not improve functionality. Therefore, it is possible that comprehensive measures of neuronal activity can eventually facilitate PRL tracking and rehabilitation.

However, in addition to questions concerning PRL development, controversy surrounds the retinotopic effect PRL development has on the visual cortex. In particular, the ophthalmology community has yet to reach consensus about whether the visual cortex reorganizes to fill in the silent zone of the primary visual cortex that was formerly mapped from the part of the retina affected by a central scotoma. If remapping does occur, as some studies indicate, regions of the cortex that normally were innervated by the damaged retina would be recruited in response to peripheral stimulus falling on healthy retinal areas, which could play an integral role in determining how patients adopt a PRL (50). Cortical remapping has been observed in the somatosensory system after limb amputation, as latent lateral connections are believed to become functional only when normal afferent signals are no longer present (51-53). However, recent studies exhibit mixed results concerning the extent of such remapping in the visual system.

Several electrophysiological studies supporting cortical reorganization following induced retinal lesions in animals have generated excitement in the field of ophthalmology. In several macaque studies, electrophysiological results demonstrate stimulus-driven activity within the deafferented zone, reflecting cortical reorganization of the primary visual cortex (V1) (54-58). On the other hand, one study found that cytochrome oxidase levels in the silent zone of the visual cortex remained depressed for months after monocular retinal lesions in adult macaques (59). Another study also inducing a monocular retinal lesion found no topographic reorganization near the silent zone in monkeys (60).

Recent fMRI studies demonstrate similar controversy as these electrophysiological results. For instance, a small study using BOLD fMRI on two human subjects suffering from juvenile macular degeneration (JMD) found that parts of the visual cortex (both striate and extrastriate) that normally respond only to central visual stimuli became strongly activated by peripheral stimuli as a result of central scotoma development (61). The first type of stimulus consisted of a one-back task in which subjects were presented with natural viewing scenes (faces, objects, etc.) and pressed a button when consecutive images were presented. The second experiment presented words (objects) in a passive (one-back) task for the first subject (second subject). Both types of stimuli exhibited activation in the foveal cortex by peripheral stimuli. In contrast to these results, Sunness *et al.* studied one AMD patient and found that cortical areas corresponding to a pericentral scotoma location remained silent (relative to a normal subject) during passive retinotopic mapping (50). In another, more expansive study, Smirnakis *et al.* utilized fMRI (BOLD contrast) to demonstrate a lack of cortical reorganization in four macaque monkeys scanned every 2-8 weeks for 18-30 weeks following peripheral retinal lesions 2-8 degrees in diameter (62).

However, this study triggered intense controversy, as Calford *et al.* recently responded with the assertion that BOLD fMRI provides a poor marker of cortical reorganization (63). Specifically, Calford *et al.* argue that because projection from the lateral geniculate nucleus to the visual cortex is believed to have limited reorganization (64), shifted receptive fields resulting from reorganization are manifested through cortical output, or neuronal spiking. Under this assumption, BOLD's likely reflection of synaptic input as opposed to spiking output renders it insufficient in gauging dynamic spiking

patterns resulting from potential reorganization (63). Furthermore, the proposed long-range horizontal connectivity within V1 resulting from reorganization would reside primarily within superficial layers, while BOLD is biased towards layer 4 due to its high vascularization (65-67). From this perspective, an ideal fMRI measure for evaluating reorganization would need to have closer coupling to neuronal output, or spiking, and better localization to actual neuronal populations than BOLD, which is highly susceptible to vascularization.

CBF, CBV and CMRO₂ have these advantages over BOLD but have yet to be applied to patients with visual field impairment. The combination of CMRO₂ coupling to neuronal spiking (25,26) and the supposed involvement of spiking in cortical reorganization (63) provide motivation for incorporating CMRO₂ modeling to gain additional insight to the extent of reorganization. Similarly, the refined spatial localization of CBF, CBV and CMRO₂ to actual populations of neurons as opposed to vascularization could enable fMRI to provide more definitive answers to these controversial questions surrounding reorganization. However, before realizing the potential of quantitative fMRI in this context, methodological improvements are needed to make these approaches suitable for patient populations.

1.4 General Summary

This chapter has provided an overview of the current state of fMRI utilization in studies with repeated measures. Furthermore, it has summarized the past usage of CBF and CBV as quantitative complements to the BOLD contrast. While traditional BOLD fMRI will remain an important part of future rehabilitation studies due to its ease of use and high sensitivity, shortcomings require increased development of quantitative fMRI. As summarized above, the following chapters address a number of challenges that accompany the integration of these measures, which are typically only used in healthy populations, into rehabilitation studies involving patient populations.

After establishing the feasibility of acquiring CBF and estimating $CMRO_2$ in patients with central visual impairment, the subsequent challenges improve image acquisition and modeling in healthy subjects. However, the motivation for these studies and the benefits that they provide directly relate to future utilization in rehabilitation studies. Importantly, minimizing these assumptions will enable improved experimental paradigms in other rehabilitation studies for a range of conditions. With this goal, this dissertation demonstrates a range of improvements to all research phases including acquisition, analysis and applications.

CHAPTER 2

ARTERIAL SPIN LABELING TO REDUCE FMRI MEASUREMENT VARIABILITY IN INDIVIDUALS WITH CENTRAL VISUAL IMPAIRMENT

Functional magnetic resonance imaging (fMRI) using blood oxygenation level dependent (BOLD) contrast is commonly used to assess cortical dynamics with repeated measures. This chapter applies BOLD in subjects implanted with a sub-retinal prosthesis used to treat subjects with central visual field impairment due to retinitis pigmentosa (RP). Variability associated with fellow eye stimulus between scanning session days and months apart suggests that actual treatment effects in the implanted eye are indistinguishable due to inherent BOLD variability. Arterial spin labeling (ASL) to measure cerebral blood flow (CBF) and estimation of cerebral metabolic rate of oxygen (CMRO₂) are proposed to complement BOLD and improve reproducibility between scans. This study reports the first application of these methods in subjects with central visual field loss and finds improved inter-scan reliability for CBF relative to BOLD.

2.1 Introduction

Retinitis Pigmentosa (RP) is a genetic disease causing first peripheral and then central visual field loss (68). However, despite degeneration of the outer retinal cells, the inner retina can remain intact (69,70). For this reason, recent developments in neurorehabilitation for individuals with visual field loss include retinal prostheses designed to electrically stimulate retinal/neural cells. One sub-retinal device, the Artificial Silicon Retina (ASR), has been previously evaluated in several contexts (71-77). More recently, the ASR microchip was implanted in a group of seven subjects and some visual improvements were observed (78). This chapter utilizes fMRI to assess cortical dynamics before and after implantation of this retinal prosthesis that is thought to provide a neurotrophic effect on the retinal cells.

Although several retinal prostheses have reported improvement to visual function, past accounts of efficacy have relied on measurements of visual capabilities without the utilization of fMRI to explore possible increased activation in the visual cortex. However, fMRI has been used in similar research initiatives for studies involving vision rehabilitation (79-82). Specifically, BOLD contrast can be used to study hemodynamics related to task performance by detecting changes in deoxyhemoglobin levels near the site of neuronal activity (1). BOLD contrast using fMRI has been the most prominent functional neuroimaging method for the last 15 years due to its high sensitivity and ease of use. However, the BOLD signal is dependent on a combination of physiological parameters, including CBF, cerebral blood volume (CBV) and CMRO₂ and therefore produces relative, not absolute results that vary longitudinally for reasons outside the

realm of neuronal activity dynamics (7). Furthermore, the magnitude of the signal change is largely dependent on brain vasculature because the BOLD signal originates from the venous concentration of deoxyhemoglobin so “activation” may be aligned more with draining veins than actual neuronal populations (8). With regard to spatial specificity, the attribute that enables BOLD contrast, paramagnetism, produces a bulk susceptibility difference between the vessels and surrounding tissue, so image voxels in extravascular space can exhibit the BOLD contrast. While this improves BOLD sensitivity (a main reason for BOLD’s ease of utilization), spatial resolution of activation is not as specific as methods using other means of contrast such as CBF (8). Despite these challenges, BOLD’s high sensitivity is conducive to studying patient populations due to potential reduced hemodynamics in response to stimuli.

The empirical shortcomings of BOLD longitudinal consistency and bias to draining veins have provided motivation for noninvasive measures of CBF and CBV, as well as estimation of $CMRO_2$. While initial MRI methods measuring CBF relied on contrast agents to label cerebral blood (9), ASL enables measurement of absolute CBF without the use of any exogenous agents. Specifically, ASL uses magnetically labeled arterial blood water as an endogenous tracer for measuring CBF (10-19).

This chapter utilizes BOLD contrast before and after ASR implantation to investigate effects in the visual cortex of a rehabilitation intervention in the retina. Furthermore, this chapter presents preliminary evidence that CBF measurement using ASL and $CMRO_2$ estimation, which have not been previously applied to individuals with

central visual impairment, have sufficient sensitivity for this population. Finally, reproducibility of CBF and BOLD is assessed.

2.2 Methods

The main objectives of this experiment were (1) to investigate cortical effects of the ASR implantation, (2) to explore potential CBF measurement and CMRO₂ estimation in the individuals with central visual impairment and (3) to compare reproducibility of CBF and BOLD contrasts. Five of the seven participants (4 female) with RP were evaluated before and after random monocular ASR implantation. Two of these subjects returned for CBF acquisition 9 months after implantation to explore the feasibility of utilizing CBF and CMRO₂ methods in future rehabilitation studies. For all subjects, written consent was acquired and all experiments were approved by Emory University's Internal Review Board.

2.2.1 Visual Specifications

Five individuals with RP (pre-operative specifications: age 34-62, visual acuity 20/90-540, central visual field 2.5-10 radial deg.) participated in this study (Table 2.1).

Table 2.1: Pre-implantation visual specifications for participating subjects

| Subject | Age | Gender | Fellow | | Implant | |
|---------|-----|--------|---------------|------------------------------|---------------|------------------------------|
| | | | Visual Acuity | Visual Field Extent (Radius) | Visual Acuity | Visual Field Extent (Radius) |
| 1 | 45 | F | 20/250 | 2.5 | 20/270 | 2.5 |
| 2 | 34 | F | 20/90 | 10 | 20/100 | 10 |
| 3 | 35 | M | 20/530 | 2.5 | 20/540 | 2.5 |
| 4 | 47 | F | 20/110 | 10 | 20/110 | 10 |
| 5 | 62 | F | 20/100 | 4 | 20/100 | 4 |

Participants were scanned using BOLD fMRI on two separate days in the same week before ASR implantation and in a single session 6 months after implantation. Although the ASR chip was implanted randomly in only one eye for each patient, both eyes were separately assessed in each BOLD scanning session. Furthermore, two subjects (2 and 4) also participated in separate scanning session 9 months after implantation in which simultaneous CBF and BOLD data were acquired.

2.2.2 Visual Stimuli

BOLD scanning sessions consisted of ten stimuli (rings at five eccentricities and checkerboards at five resolutions) reversing contrast at 8 Hz as patients fixated on a central target. Ring eccentricity was customized to cover regions both inside and outside the functioning visual fields based on specific subject visual impairment characteristics immediately preceding each fMRI session. Extent of the central visual field was determined with scanning laser ophthalmoscope macular perimetry. Similarly, checkerboard resolution was customized to each subject's visual acuity to ensure an appropriate range of resolutions both within and outside the resolution capabilities of the subject, occupying approximately 8 radial deg. of the central visual field. Each scanning session consisted of three scans with checkerboards and four scans with rings for each eye. For each scan presenting ring stimuli, three 16 second blocks of fixation were interleaved with two rounds of 5 eccentric rings (16 seconds per ring stimuli) for a total of four scans, each 3 minutes and 28 seconds in duration. Similarly, for each scan presenting checkerboard stimuli, fixation was interleaved with flashing checkerboards and repeated for a total of three scans, each 5 minutes and 36 seconds in duration. For

each stimulus, each scan consisted of a pseudo-random order of ring eccentricity or checkerboard resolution. For CBF scanning sessions which also consisted of three scans with flashing checkerboard and four scans with ring stimuli, four stimuli (rings at two eccentricities and checkerboards at two resolutions) were interleaved with fixation using 48 second blocks. All stimuli for the simultaneous CBF/BOLD scanning session were within the visual capabilities of each subject and longer blocks were used due to the lower temporal resolution of CBF relative to BOLD acquisition.

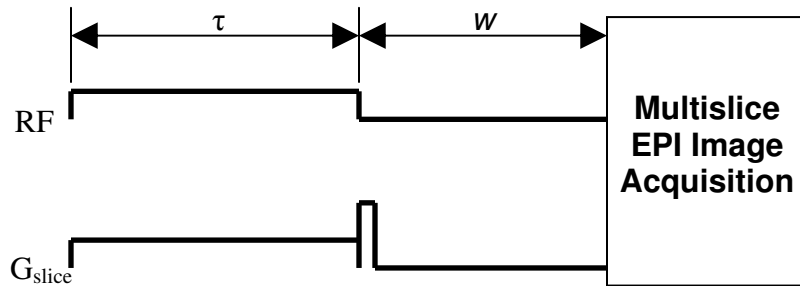


Fig. 2.1: CASL sequence consists of labeling time (τ) and post-labeling delay (w) prior to multislice acquisition utilizing EPI readout.

2.2.3 MRI Acquisition

Anatomical and functional data were acquired with a 3 Tesla whole body system (Siemens Medical Solutions, Malvern, PA). BOLD acquisition utilized a gradient echo EPI sequence (33 slices, 3 mm isotropic resolution, 2 sec repetition time (TR), 30 ms echo time (TE), 90 deg. flip angle). In the same session T1-weighted anatomical images were acquired using a magnetization prepared rapid gradient echo (MPRAGE) sequence (1 mm isotropic resolution). For CBF sessions, a continuous ASL (CASL) sequence collected 16 axial slices 6 mm thick with a 1.5 mm gap, 3 sec TR, 19 ms TE, 1.4 sec

labeling duration (τ) and 700 ms post-labeling delay (w) using a common CASL sequence detailed in Fig. 2.1 (83). In this method, arterial blood flowing toward the imaging region is labeled by adiabatic magnetic inversion. After a delay to allow for labeled blood to flow into the imaging region, an image is acquired that depends on both the static tissue and the amount of tagged blood that has entered the slice. This “label image” is followed by a second image in which the inflowing blood is not inverted. Subtracting the labeled image from the control image yields a CBF-weighted difference image dependent only on blood flow that can be used to calculate absolute CBF. Similarly, the addition of control and labeled images yields BOLD-weighted images, providing simultaneous acquisition of CBF and BOLD contrasts. Labeling is continuously applied by simultaneous radiofrequency pulse, which inverts the arterial spins, and slice selective gradient, which localizes the spatial specificity of the labeling. Because the same image acquisitions are used for both BOLD and CBF images, this sequence provides more favorable temporal resolution ($TR=3$ sec) than interleaved CBF and BOLD acquisitions. However, TE , the time between excitation and readout, is shorter than optimal BOLD (19 ms in this study relative to ~ 30 -35 ms for optimal BOLD). Despite this tradeoff, high BOLD sensitivity allows for this concession and this acquisition approach has been used to estimate $CMRO_2$ in animal (25,26) and healthy human studies (19,27).

2.2.4 BOLD and CBF Analysis

All functional data were analyzed using SPM2 (Wellcome Department, University College of London, London, UK) and BOLD data were preprocessed for slice

scan time correction, motion correction and normalization to standardized MNI space. For CBF data, pair-wise subtraction between motion corrected label and control image acquisitions provided CBF-weighted images which were quantified using the following equation (84):

$$CBF = \frac{\lambda R_{1,BLOOD} \Delta CBF_{weighted}}{2\alpha_l M_0 (e^{-wR_{1,BLOOD}} - e^{-(\tau+w)R_{1,BLOOD}})} \quad [2.1]$$

where CBF denotes quantified perfusion images, λ is blood/water partition coefficient, $\Delta CBF_{weighted}$ is the difference between control and label images, $R_{1,BLOOD}$ is the longitudinal relaxation rate of blood, M_0 is the equilibrium magnetization of brain and α_l is the tagging efficiency. Finally, CBF images were normalized to MNI space and spatially smoothed with a 6 mm kernel to improve the signal-to-noise ratio (SNR).

Similarly, addition of control and labeled images yields BOLD-weighted data. For all data, a multi-run general linear model was applied to generate activation maps for each ring eccentricity and checkerboard resolution. Extent of activation was defined by suprathreshold voxel counts using a statistical threshold of $p < 0.05$ corrected for false discovery rate (FDR) (85) for standard BOLD data and $p < 0.05$ (uncorrected) for CBF and data. The lower inherent SNR of CBF required this less stringent statistical threshold. Furthermore, all activation maps utilized a cluster threshold > 10 contiguous normalized 2 mm^3 voxels.

2.2.5 CMRO₂ Estimation

Simultaneous acquisition of CBF and BOLD-weighted images with the CASL sequence also enables CMRO₂ estimation. CBF data was acquired only in a single session and therefore not applied to tracking treatment effects in this study. However, its previously described longitudinal consistency makes its feasibility in this population a critical accomplishment toward improving future studies using repeated measures to study subjects with visual field loss. For each stimulus and subject, the region of interest (ROI) for CMRO₂ estimation was defined as voxels that were suprathreshold for both CBF and BOLD contrasts. As with most studies estimating CMRO₂, data acquired with this sequence assumes CBV based on measured CBF using Grubb's relationship

$$\frac{CBV}{CBV_0} = \left(\frac{CBF}{CBF_0} \right)^\alpha \quad [2.2]$$

where α , the constant relating CBV to CBF, is 0.38 (20). Some studies acquire BOLD and CBF data during induced hypercapnia to estimate a calibration parameter (M) (18,19) while others assume this value based on literature (27,28). The present study did not induce hypercapnia, instead calculating CMRO₂ utilizing a range of realistic values of M to explore the applicability of this estimation method to the low vision population. This model estimates CMRO₂ using

$$\frac{\Delta BOLD}{BOLD} = M \cdot \left(1 - \left(\frac{CMRO_2}{CMRO_{2 \ 1_0}} \right)^\beta \cdot \left(\frac{CBF}{CBF_0} \right)^{\alpha-\beta} \right) \quad [2.3]$$

where β is a constant reflecting the influence of deoxyhemoglobin concentration and assumed to be 1.5 (18,19). This approach yields an estimate of $CMRO_2$ for each value of M , providing insight about the feasibility of using this approach to estimate $CMRO_2$ in subjects with visual field impairment.

2.2.6 Evaluation of Treatment Effects

As described above, inherent BOLD variability in voxel counts can confound changes in brain hemodynamics related to improved visual capabilities. This variability is assessed by the percent change in suprathreshold voxel counts between two pre-implantation scans and averaged over five ring or checkerboard stimuli for each patient and eye:

$$Variability = \frac{100\%}{5} \sum_{stimuli} \frac{Activation_{PRE_ASR1} - Activation_{PRE_ASR2}}{Mean(Activation_{PRE_ASR1}, Activation_{PRE_ASR2})} \quad [2.4]$$

Similarly, change between pre- and post-implantation hemodynamics were assessed as follows:

$$Variability = \frac{100\%}{5} \sum_{stimuli} \frac{Activation_{POST_ASR} - Mean(Activation_{PRE_ASR1}, Activation_{PRE_ASR2})}{Mean(Activation_{PRE_ASR1}, Activation_{PRE_ASR2})} \quad [2.5]$$

Results for each comparison were compared for fellow and implanted eyes to determine the extent to which treatment effects (change between post- and pre-implantation) exceeded inherent variability (change between two pre-implantation sessions). Similarly, change in percent signal change was compared for fellow and implanted eyes.

2.2.7 Assessment of BOLD and CBF Reproducibility

Reproducibility of BOLD and CBF signal change was assessed for the two subjects participating in the separate scanning session that incorporated simultaneous CBF and BOLD measurement. Mean signal changes between visual stimuli and rest were calculated for each scan for suprathreshold voxels (cluster threshold > 5 voxels and $p < 0.05$ and 0.01 for CBF and BOLD, respectively). Significance thresholds were different from multi-run analysis because activation maps, which were calculated for separate scans within a scanning session, had fewer degrees of freedom and therefore less statistical power. Furthermore, a less stringent statistical threshold was used for CBF than BOLD due to differences in sensitivity and SNR between the two contrasts. Coefficient of variation (CV) was calculated for each subject, contrast and stimulus type with the following equation (7):

$$CV_{INTRA} = (100\%) \cdot \frac{\sigma_i}{x_{avg}} \quad [2.6]$$

Where x_{avg} and σ_i are the average and standard deviation of percent signal change across scans for a given subject, session, stimulus and contrast. CV of BOLD and CBF were

compared for each subject and stimulus to assess reproducibility within a scanning session.

2.3 Results

2.3.1 fMRI Results: BOLD

As previously described, recent studies consistently indicate that CBF and CMRO₂ measures provide more longitudinal consistency than BOLD between patients and over time (7). For the purposes of tracking and evaluating dynamic neuronal activity resulting from rehabilitation or disease progression, BOLD can be prone to variability confounds unrelated to actual pathophysiology (specifically visual stimuli in this study). For example, for subject 2 the two scanning sessions just days apart demonstrate high variability in suprathreshold voxel counts for a flashing checkerboard stimulus (Fig. 2.2 and Table 2.2). This variability was found despite this subject's fairly good acuity

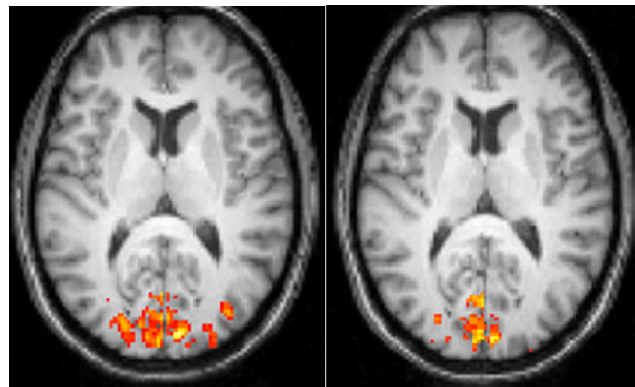


Fig. 2.2: Low vision patient exhibits variability in BOLD activation on two separate scanning sessions just days apart.

(20/100) and fairly intact central visual field (20 degree diameter). To evaluate reproducibility, suprathreshold voxel counts between two scanning sessions prior to implantation were compared for each stimulus. The median change in number of suprathreshold voxels (results for each eye's 5 stimuli average per patient) between scanning sessions were -65% (-38%) for rings (flashing checkerboard) stimuli for fellow eye and were -28% (-61%) for rings (flashing checkerboard) stimuli for the implanted eye (Table 2.2). Beyond the scope of this intersession variability, change between pre- and post-implantation suprathreshold voxel counts exhibited changes in hemodynamics for both eyes (implanted and fellow) and each stimulus type. Specifically, median change in voxel counts were 109% (301%) for rings (flashing checkerboard) stimuli for fellow eye and were -12% (141%) for rings (flashing checkerboard) stimuli for the implanted eye (Table 2.2). Similarly, inter-session variability in percent signal change suggests that changes between pre- and post-implantation might reflect inherent variability as opposed to treatment effects (Table 2.3). There are two possible causes for greater changes between pre- and post-treatment sessions relative to those between two pre-treatment sessions. First, treatment and/or disease progression could impact voxel counts and percent signal change after implantation. However, there is no trend in the results that suggests that treatment (which would be seen as consistent positive values in the implanted eye) or disease progression (which would be seen as consistent negative values in the fellow eye) caused the voxel count or percent signal change results. Second, inter-session variability unrelated to treatment effects or disease progression could be more significant when the sessions are separated by more time. This uncertainty

Table 2.2: Change in suprathreshold voxel counts between scanning sessions

| Subject | Stimulus | Change in Voxel Counts Between Pre-implantation Sessions | | Change in Voxel Counts Between Pre- and Post-implantation | |
|----------------|--------------|--|-----------------|---|------------------|
| | | Fellow | Implant | Fellow | Implant |
| 1 | Ring | -200% | 29% | 139% | -67% |
| | Checkerboard | -200% | 30% | 442% | -23% |
| 2 | Ring | -65% | -40% | 30% | -61% |
| | Checkerboard | -31% | -130% | 370% | -36% |
| 3 | Ring | 23% | -200% | 3846% | 2200% |
| | Checkerboard | -127% | -17% | -99% | 725% |
| 4 | Ring | -163% | 17% | 109% | 378% |
| | Checkerboard | -38% | -100% | 301% | 169% |
| 5 | Ring | 19% | -28% | -86% | -12% |
| | Checkerboard | 16% | -61% | 41% | 141% |
| Median (Range) | Ring | -65 (-200 - 23) | -28 (-200 - 29) | 109 (-86 - 3846) | -12 (-67 - 2200) |
| | Checkerboard | -38 (-200 - 16) | -61 (-130 - 30) | 301 (-99 - 442) | 141 (-36 - 725) |

Table 2.3: Change in percent signal change between scanning sessions

| Subject | Stimulus | Change in Percent Signal Change Between Pre-implantation Sessions | | Change in Percent Signal Change Between Pre- and Post-implantation | |
|----------------|--------------|---|-----------------------|--|----------------------|
| | | Fellow | Implant | Fellow | Implant |
| 1 | Ring | -0.58% | -0.60% | 0.23% | -0.08% |
| | Checkerboard | -0.55% | -1.87% | 0.69% | -0.79% |
| 2 | Ring | 0.05% | -0.10% | 0.01% | 0.43% |
| | Checkerboard | 0.02% | -0.14% | 0.09% | -0.16% |
| 3 | Ring | -0.23% | -0.73% | 0.22% | 0.15% |
| | Checkerboard | -0.52% | -0.98% | 0.21% | -0.54% |
| 4 | Ring | 1.47% | -2.25% | -0.02% | -1.49% |
| | Checkerboard | 0.69% | -0.32% | -0.01% | -0.19% |
| 5 | Ring | -0.02% | -0.04% | 0.20% | 0.04% |
| | Checkerboard | 0.03% | 0.01% | 0.15% | 0.12% |
| Median (Range) | Ring | -0.02 (-0.58 - 1.47) | -0.60 (-2.25 - -0.04) | 0.20 (-0.02 - 0.23) | 0.04 (-1.49 - 0.43) |
| | Checkerboard | 0.02 (-0.55 - 0.69) | -0.32 (-1.87 - 0.01) | 0.15 (-0.01 - 0.69) | -0.19 (-0.79 - 0.12) |

underscores the need to complement BOLD with more consistent measures, such as CBF, to control for variability in BOLD repeated measurements.

2.3.2 fMRI Results: CBF

An extension of this study examined two of the subjects (2 and 4) incorporating simultaneous BOLD and CBF acquisition with the CASL sequence 9 months after ASR implantation. Stimuli were presented to the fellow eye which was the left eye for these two subjects. The ability to detect activation in the occipital lobe utilizing CBF with this sequence assures the ability to estimate $CMRO_2$ in future studies also employing hypercapnic calibration or an alternate model as described in Chapter 4. Fig. 2.3 exhibits typical results, as statistical analysis ($p < 0.05$) demonstrates bilateral CBF activation in the occipital lobe. Slightly more activation is evident in the right hemisphere, which is

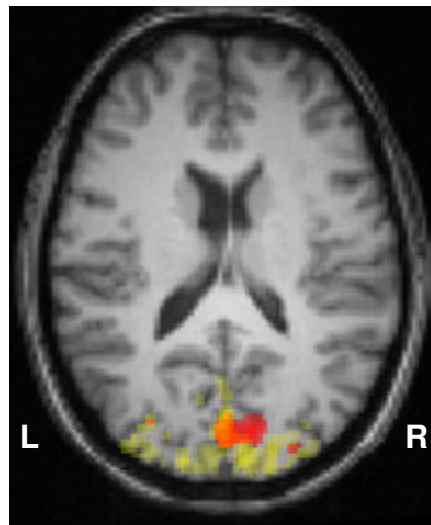


Fig. 2.3: CBF (red) demonstrates better spatial specificity than BOLD (yellow) for subject AT03 with small ring visual stimulus.

consistent with the left eye's disproportionate involvement with the left visual field. This activation pattern demonstrates sufficient sensitivity and specificity in CBF acquisition for the patient population. Furthermore, consistent with literature, BOLD activation generally appears to be more biased toward draining veins than CBF for both subjects (Fig. 2.4). While CBF data were not acquired before implantation for treatment evaluation, the demonstrated feasibility of using this technique in the low vision population for the first time supports the utilization of this technique in future studies.

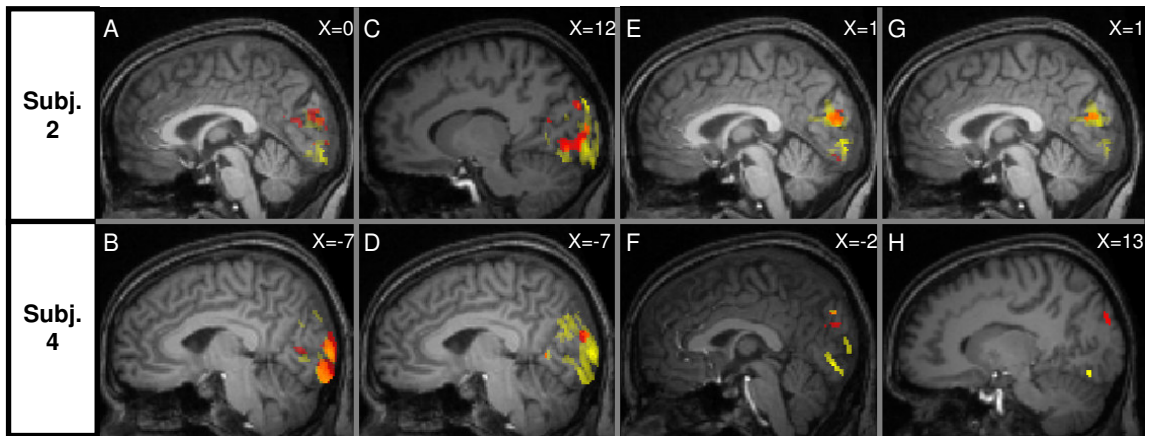


Fig. 2.4: CBF (red) and BOLD (yellow) activation for low resolution checkerboard (A,B), high resolution checkerboard (C,D), small ring (E,F) and large ring (G,H) for 2 low vision subjects.

2.3.3 fMRI Results: CMRO₂ Estimation

As described above, CBF and BOLD data are simultaneously acquired and calibration parameter M is assumed based on values from similar studies. To account for the uncertainty of an assumed value of M, hemodynamics are also modeled over a range of reasonable calibration values to ensure that the CASL sequence applied to individuals with central visual impairment can yield reasonable CMRO₂ estimates.

Table 2.4: Relative signal changes for BOLD, CBF and CMRO₂

Subject 2

| Contrast | Small Ring | Large Ring | Low Res. Check. | High Res. Check. |
|---------------------|------------|------------|-----------------|------------------|
| %ΔBOLD | 0.1 | 0.3 | 0.2 | 0.1 |
| %ΔCBF | 14.1 | 32.8 | 22.5 | 14.6 |
| %ΔCMRO ₂ | 10.0 | 22.6 | 15.7 | 10.4 |

Subject 4

| Contrast | Small Ring | Large Ring | Low Res. Check. | High Res. Check. |
|---------------------|------------|------------|-----------------|------------------|
| %ΔBOLD | 0.1 | -- | 0.3 | 0.4 |
| %ΔCBF | 82.1 | -- | 75.5 | 183.7 |
| %ΔCMRO ₂ | 56.1 | -- | 50.9 | 115.6 |

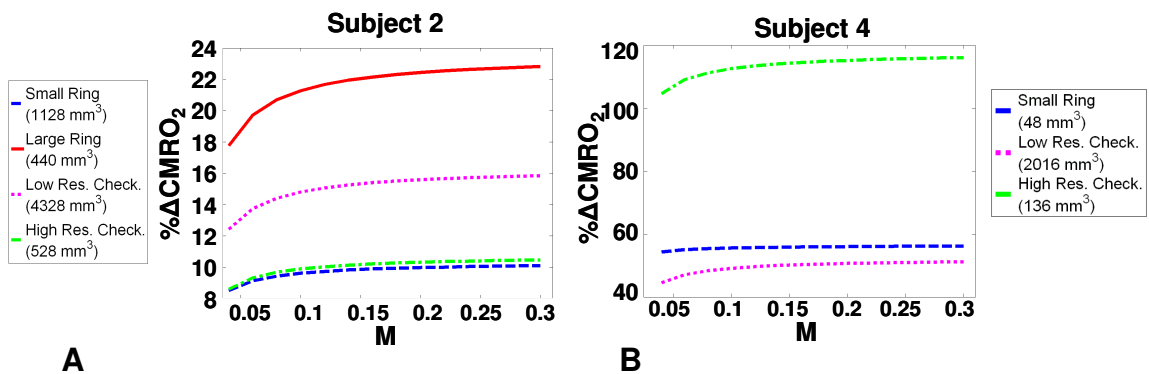


Fig. 2.5: CMRO₂ estimation results over a range of M.

Assuming an M value of 0.24 based on previous literature (18,33), results generally fell within a predefined reasonable range of $\% \Delta \text{CMRO}_2$ (between 6 and 48% based on published values for similar stimuli (86)). For instance, $\% \Delta \text{CMRO}_2$ estimates for subject 2, who was sensitive to all four types of stimuli, were between 10 and 23% for all stimuli (Table 2.4). On the other hand, estimates were higher than expected for subject 4; although visual acuity and central visual fields are similar between subjects 2 and 4, subject 4 exhibited a smaller activation region, likely resulting in less accurate estimated relative changes (Table 2.4). Similarly, the relative proportions of the three contrasts ($\% \Delta \text{BOLD}$, $\% \Delta \text{CBF}$ and $\% \Delta \text{CMRO}_2$) are consistent with expectations as long as sufficient activation is detected (all stimuli for subject 2, small ring and low resolution checkerboard for subject 4). These results suggest that the current techniques can be used to estimate reliable CMRO_2 values as long as a sufficiently large ROI is deemed “active” for both CBF and BOLD contrasts. However, to improve SNR and sensitivity, especially to small active ROIs, CBF acquisition methods must be improved.

To further examine the effects of calibration, $\% \Delta \text{CMRO}_2$ was estimated using a range of values of M (selection of M is commonly determined empirically). As shown in Fig. 2.5, $\% \Delta \text{CMRO}_2$ values are quite variable at low values of M, while estimates are more stable at higher values of M which are often reported for fMRI studies of the visual cortex (18,19). All estimates for both patients are within the reasonable range with the possible exception of the high resolution flashing checkerboard for subject 4, presumably due to the low number of active voxels suggesting that the patient did not have a sufficiently detectable hemodynamic response to this particular stimulus. Results for the patient sensitive to all stimuli are shown to be reasonable at all values of M.

2.3.4 Reproducibility of CBF and BOLD Signal Changes

As shown in Table 2.5, over 2 subjects and 4 stimuli, CV was reduced for CBF in all but two instances (large ring stimulus for subject 2 and low resolution checkerboard for subject 4). Across subjects and stimuli, the mean CV was $12 \pm 10\%$ and $26 \pm 5\%$ for CBF and BOLD, respectively, demonstrating better reproducibility for CBF relative to BOLD percent signal change. Furthermore, average CV across subjects for each stimulus showed reduced CV for CBF relative to BOLD for all four stimuli (Fig. 2.6).

Table 2.5: CV reflects better reproducibility for CBF than BOLD

| Subject | Stimulus | CBF | | BOLD | |
|---------|------------------------|---|-------------------------------|--|------------------------------|
| | | Change (%) | CV (%) | Change (%) | CV (%) |
| 2 | Small Ring | 68.02 ± 13.56 | 20 | 0.64 ± 0.13 | 21 |
| | Large Ring | 58.55 ± 12.25 | 21 | 0.61 ± 0.10 | 16 |
| | Low Res. Checkerboard | 58.45 ± 4.31 | 7 | 0.76 ± 0.19 | 26 |
| | High Res. Checkerboard | 51.80 ± 1.93 | 4 | 0.67 ± 0.16 | 24 |
| 4 | Small Ring | 82.58 ± 3.92 | 5 | 0.64 ± 0.23 | 30 |
| | Large Ring | 81.24 ± 6.31 | 8 | 0.71 ± 0.20 | 29 |
| | Low Res. Checkerboard | 56.91 ± 17.19 | 30 | 0.71 ± 0.21 | 29 |
| | High Res. Checkerboard | 63.88 ± 1.57 | 2 | 0.74 ± 0.23 | 30 |
| | | CBF CV (Mean \pm S.D.): | 12 ± 10 | BOLD CV (Mean \pm S.D.): | 26 ± 5 |

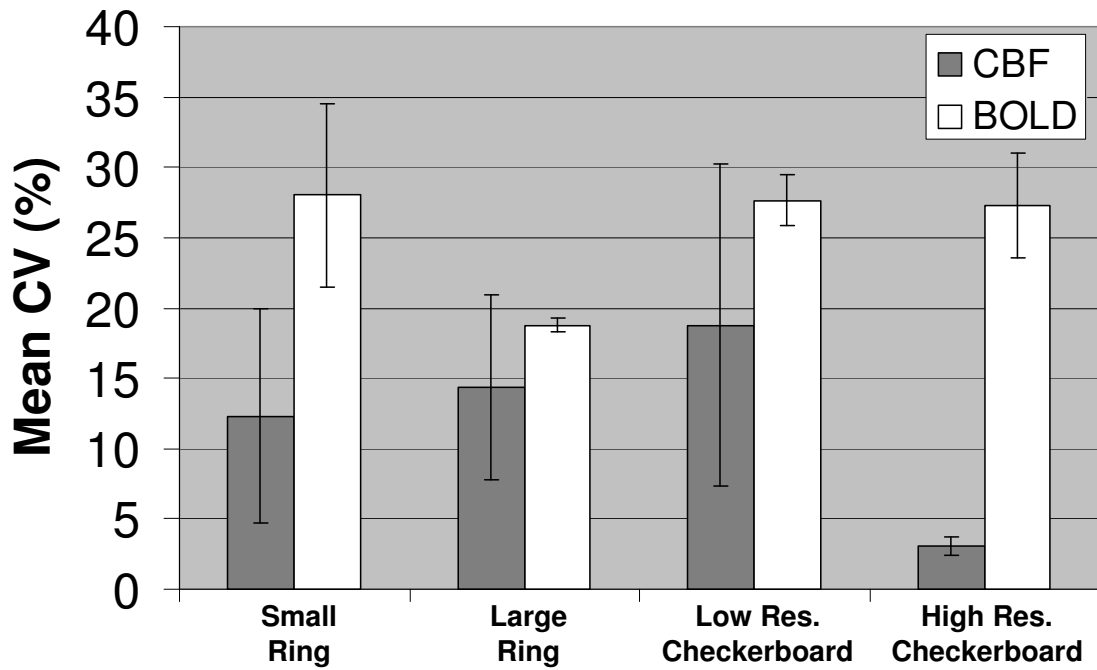


Fig. 2.6: Average CV over both subjects for each stimuli and contrast.

2.4 Discussion and Conclusion

This chapter evaluates the variability in repeated measurements utilizing BOLD fMRI contrast in individuals with the ASR retinal prosthesis before and 6 months after implantation. While this approach assesses cortical hemodynamics in the context of disease progression and treatment effects, inherent BOLD variability is evident between pre-implantation scanning sessions. Furthermore, changes in voxel counts and percent signal change are commonly greater for the fellow eye than the implanted eye indicating that the change is probably due to inherent variability rather than treatment effects.

Therefore, the present findings demonstrate a significant potential flaw in using BOLD for functional neuroimaging studies with repeated measures.

To address this challenge, this chapter explores the first utilization of noninvasive CBF measurement and $CMRO_2$ estimation in a population with central visual impairment. Consistent results in two subjects demonstrate the feasibility of these approaches in this patient population. Furthermore, within-session reproducibility of percent signal change is consistent with other studies of healthy subjects (7,87). In conjunction with literature demonstrating less inter-session variability in CBF relative to BOLD, these results support utilization of these techniques in future studies involving repeated measures. Furthermore, published findings of closer linkage between CBF: $CMRO_2$ and neuronal spiking in animal models (25,39) suggest that studies of neurorehabilitation and disease tracking could benefit from quantitative fMRI.

Although the BOLD images acquired with traditional ASL are not optimized due to short TE, several sequences acquire CBF images and optimized BOLD. For instance, dual echo sequences acquire images at a short echo time for CBF-weighting and longer echo time for BOLD-weighting (88). One multi-echo sequence even acquires CBV-weighted images simultaneously with optimized CBF and BOLD images (23), adding yet another measurement to assess hemodynamics. As MRI pulse sequences develop and become more readily available, inclusion of CBF in rehabilitation protocols will provide more comprehensive analysis of hemodynamics and more objective measures for longitudinal studies with repeated measures. Development of multi-echo image

acquisition and analysis to optimize multiple fMRI contrasts are explored in Chapters 3 and 4.

CHAPTER 3

ESTIMATING CEREBRAL BLOOD VOLUME WITH EXPANDED VASCULAR SPACE OCCUPANCY SLICE COVERAGE¹

A model for quantifying cerebral blood volume (CBV) based on the vascular space occupancy (VASO) technique and varying the extent of blood nulling yielding task-related signal changes with various amounts of blood oxygenation level-dependent (BOLD) and VASO weightings was previously described. Challenges associated with VASO include limited slice coverage and the confounding inflow of fresh blood. In this work, an approach that extends the previous model to multiple slices and accounts for the inflow effect is described and applied to data from a multi-echo sequence simultaneously acquiring VASO, cerebral blood flow (CBF) and BOLD images. This method led to CBV values (7.9 ± 0.3 and 5.6 ± 0.3 mL blood/100 mL brain during activation and rest, respectively) consistent with previous studies using similar visual stimuli. Furthermore, an increase in effective blood relaxation (0.65 ± 0.01) compared to the published value (0.62) was detected, likely reflecting inflow of fresh blood. Finally, CMRO₂ estimates using a multiple compartment model without assumption of CBV_{REST} led to estimates (18.7 ± 17.0 %) that were within published ranges.

¹ The work in this chapter has been published as “Glielmi CB, Schuchard R, Hu X. Estimating Cerebral Blood Volume with Expanded Vascular Space Occupancy Slice Coverage [Electronic publication ahead of print].” Reprinted with permission of Wiley-Liss, Inc. a subsidiary of John Wiley & Sons, Inc.

3.1 General Introduction

BOLD contrast-based fMRI has been the most widely used functional neuroimaging method for the last 15 years. Despite its wide utilization, there are two important limitations related to the BOLD contrast. First, the contrast is dependent on a combination of physiological parameters, including CBF, CBV and $CMRO_2$ and therefore produces relative, not absolute, measures that vary longitudinally for reasons outside the realm of neuronal activity dynamics (7). Second, the magnitude of the signal change is largely dependent on brain vasculature because the BOLD signal originates from the venous concentration of deoxyhemoglobin (8). Therefore, the localization of “activation” is aligned more with draining veins than neurons. Furthermore, the regional magnetic effect of deoxyhemoglobin exaggerates spatial extent of the measured contrast because it produces a bulk susceptibility difference between the vessels and surrounding tissue so image voxels in extravascular space also exhibit the BOLD contrast. While this susceptibility enhances BOLD sensitivity (a main reason for BOLD’s ease of utilization), spatial localization is not as specific as methods based on other types of contrast such as CBF and CBV (8).

The poor longitudinal consistency and spatial specificity of the BOLD contrast have motivated the development of noninvasive measures of CBF and CBV. While initial MRI methods for CBF imaging relied on contrast agents (9), arterial spin labeling (ASL) enables absolute CBF measurement without any exogenous agents by using magnetically labeled arterial blood water as an endogenous tracer (10-15,17). Similarly, a recent technique was introduced to image CBV by measuring the extravascular water

signal without the use of contrast agents. This technique detects changes in vascular space occupancy (VASO) by acquiring images when the blood signal is selectively nulled (22). While the original VASO technique provides CBV-weighted signal changes between rest and activation states, it relies on the assumption of absolute CBV for quantification. More recently, one group developed a biophysical model allowing for decomposition of BOLD and CBV weighting enabling CBV quantification by varying the extent of blood nulling. (24) However, this approach does not account for the inflow of fresh blood spins that are not nulled, confounding the steady-state magnetization and in turn, the VASO contrast (89). Furthermore, this model has only been applied to single slice acquisition.

The present model extends this approach to multiple slices and accounts for inflow effects. Furthermore, the application of this model to data from a multi-echo sequence simultaneously acquiring VASO, CBF and BOLD enables CMRO₂ estimation. Many studies estimating CMRO₂ use a single-compartment model, calibrating the BOLD-CBF relationship with induced hypercapnia (19,86,90,91) and deriving Δ CBV from Δ CBF based Grubb's relationship using PET (20). However, this assumption may not be accurate across brain regions and species, especially in pathological conditions. To avoid the potential errors arising from using Grubb's relationship, Lu *et al.* introduced a multi-compartment method, separating the BOLD signal into intravascular and extravascular components, that included VASO measurement (32). Specifically, they acquired CBF, BOLD and VASO images with separate sequences, assuming stimulus-induced changes in the visual cortex were constant across scans. Relative Δ CBV is estimated from CBV-weighted changes, or Δ VASO, by assuming a resting state blood

volume fraction. This introduces some uncertainty as CBV_{REST} could vary between brain regions and subjects and $CMRO_2$ estimation could be confounded by the use of separate scans for each contrast. A recent study utilizes this model in combination with simultaneous acquisition, also assuming CBV_{REST} to derive ΔCBV from traditional VASO measurements (92).

While these models have provided viable methods for estimating $CMRO_2$ in healthy subjects, the assumption of a CBV-CBF relationship or absolute CBV_{REST} makes their application to patient and/or elderly populations difficult. One study incorporated explicit CBV measurement by complementing fMRI with diffuse optical imaging (DOI) to better define the subject-specific relationship between CBF and CBV. However, DOI requires the assumption of baseline hemoglobin concentrations from published literature for quantification, has low spatial resolution and may reflect responses from different volumes of tissue relative to MR observations (21). It is therefore desirable to have an entirely MR-based approach for estimating $CMRO_2$ without assuming CBF-related CBV dynamics or absolute CBV_{REST} . For this reason, the current method's ability to noninvasively quantify CBV during simultaneous BOLD and CBF acquisition can enhance $CMRO_2$ estimation, particularly in patient populations where the CBV-CBF relationship is unknown.

The current work seeks three main objectives in this context by extending a previous modeling approach (24). First, quantification of CBV_{REST} and CBV_{ACT} is extended beyond a single slice and in conjunction with simultaneous VASO, CBF and BOLD acquisition (23). Second, this approach accounts for the inflow of fresh blood by

modeling the effective longitudinal relaxation rate of blood ($R_{1,BLOOD}$), addressing the main confound of VASO-based CBV quantification. Finally, $CMRO_2$ is estimated using a multi-compartment model (32) without assuming CBF-CBV coupling or CBV_{REST} .

3.2 Materials and Methods

A total of four normally sighted males (age 23-36) participated in this study. Written consent was acquired for all subjects and all experiments were approved by Emory University's Internal Review Board.

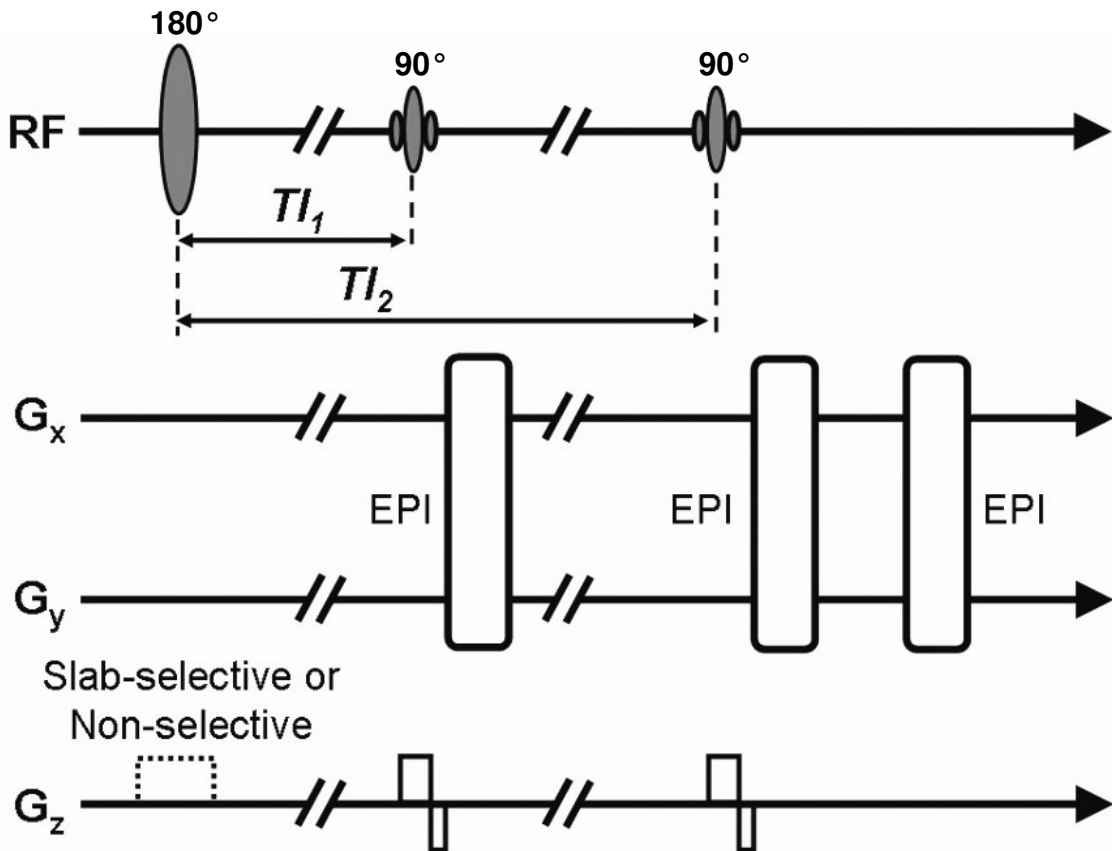


Fig. 3.1: Multi-echo sequence acquires VASO image from first excitation and ASL and BOLD images from second excitation. (Sequence from Yang et al. [23])

3.2.1 Modified Biophysical Model

The previous CBV quantification model acquires VASO images at multiple inversion times (TI), the time between inversion and transverse excitation, to provide varied CBV and BOLD weightings (24). In their study, Gu *et al.* used the singular VASO sequence (22) and applied a biophysical model to data from 14 different TIs to quantify CBV_{REST} and CBV_{ACT} . Once the relative signal changes, $\Delta S/S = (S_{ACTIVATION} - S_{REST})/S_{REST}$, are calculated for each TI, Gu *et al.* employed two steps of data fitting to the model to obtain four unknown parameters: fraction of cerebral-spinal fluid (F_{CSF}), CBV_{REST} , CBV_{ACT} and average blood oxygenation during activation ($Y_{B,ACT}$). For the first step, an admissible range of F_{CSF} was determined by focusing on the two TI values to either side of the blood nulling point. In this step, CBV_{REST} , CBV_{ACT} and $Y_{B,ACT}$ were assumed to locate an admissible range of F_{CSF} . The second step is a three-parameter non-linear fitting using a Levenberg–Marquardt algorithm applied to the remaining TI values to obtain CBV_{REST} , CBV_{ACT} and $Y_{B,ACT}$ for each of these F_{CSF} values selecting the parameters resulting in minimal residual errors (24).

The present work builds upon this model by quantifying CBV during simultaneous acquisition of VASO, CBF and BOLD, leveraging the varying TIs required for the model to expand to multiple slice coverage and modeling the inflow of fresh blood spins. The main difference between the standard VASO and multi-echo sequences in the context of quantifying CBV involves the difference in longitudinal steady state magnetization (Mag). With the singular VASO sequence, the signal dependence on longitudinal relaxation rate (R_l) can be calculated as follows:

$$Mag(TI) = 1 - 2 \cdot e^{(-TI \cdot R_1)} + e^{-R_1(TR)} \quad [3.1]$$

where TR is the repetition time and TI is the inversion time (23). With two excitations in the sequence used in this study (Fig. 3.1), one must consider the second inversion time (TI₂), or the time between inversion and the second excitation, when calculating this signal dependence:

$$Mag(TI_1) = 1 - 2 \cdot e^{(-TI_1 \cdot R_1)} + e^{-R_1(TR+TI_2-TI_1)} \quad [3.2]$$

However, steady state magnetization for either the singular VASO or multi-echo sequence is confounded by the inflow of fresh blood. To account for this, $R_{1,BLOOD}$ is assumed to be a variable that is determined by experimental data (as well as CBV_{REST} , CBV_{ACT} , F_{CSF} and $Y_{B,ACT}$). Using an ROI of suprathreshold VASO voxels, an exhaustive search of these parameters minimized the sum of squares of the difference between empirical and simulated ranges of $\Delta S/S$. As with the previous model, the two data points on either side of the zero-crossing were omitted because they are mainly sensitive to CSF as opposed to CBV.

The biophysical model was separately applied to each slice and averaged over the ROIs in all the slices to yield estimates for each subject's active 3-dimensional ROI. By fitting the data for CBV_{REST} , CBV_{ACT} , F_{CSF} , $Y_{B,ACT}$ and $R_{1,BLOOD}$, CBV quantification can be more accurately estimated for several slices and utilized for $CMRO_2$ modeling.

3.2.2 MRI Experiments

All data were acquired on a Siemens 3 Tesla Tim Trio scanner (Siemens Medical Solutions, Erlangen, Germany) with a multi-echo sequence utilizing an inversion recovery sequence with two excitations (2 sec TR, 11/11/33 ms TE for VASO/CBF/BOLD, 250 mm FOV, 75% k-space coverage, 3.9 X 3.9 mm in-plane resolution for five ascending 5 mm thick slices) for a total scanning time of approximately 21 minutes. (23). As shown in Fig. 3.1, spins are inverted by a 180° pulse before excitation and VASO acquisition. A second excitation pulse prepares for two additional gradient echo images, CBF (short TE) and BOLD (long TE). The interleaved slab-selective/non-selective gradient is used for label/control CBF images, respectively. For VASO imaging, a relatively thick slab (>100 mm) for the selective gradient is required to minimize the inflow of uninverted spins. On the other hand, excessive slab thickness could reduce perfusion signal due to the reduced amount of labeled spins. CBF and VASO contrasts are balanced based on empirical comparisons of acquisitions at slab inversion thickness of 500, 150, 125, 100 and 50 mm (23) which demonstrated that a slab thickness of 125 mm provided the best balance of CBF and VASO contrasts.

For traditional VASO acquisition, the delay between the inversion pulse and the first excitation pulse (TI_1) is selected at the blood nulling point to yield a minimized signal from voxels containing blood (22). As indicated above, the present study instead collects 14 scans with different TI_1 values to vary the level of blood nulling (24). This strategy, which allows for an increase in slice coverage relative to traditional VASO experiments, yields a different set of TI_1 values for each slice, but each sufficiently covers the range of blood nulling required to apply the biophysical model (Fig. 3.2). The time between the 180° inversion and the second excitation pulse (TI_2) is also slightly different for each slice, but the model accounts for this difference.

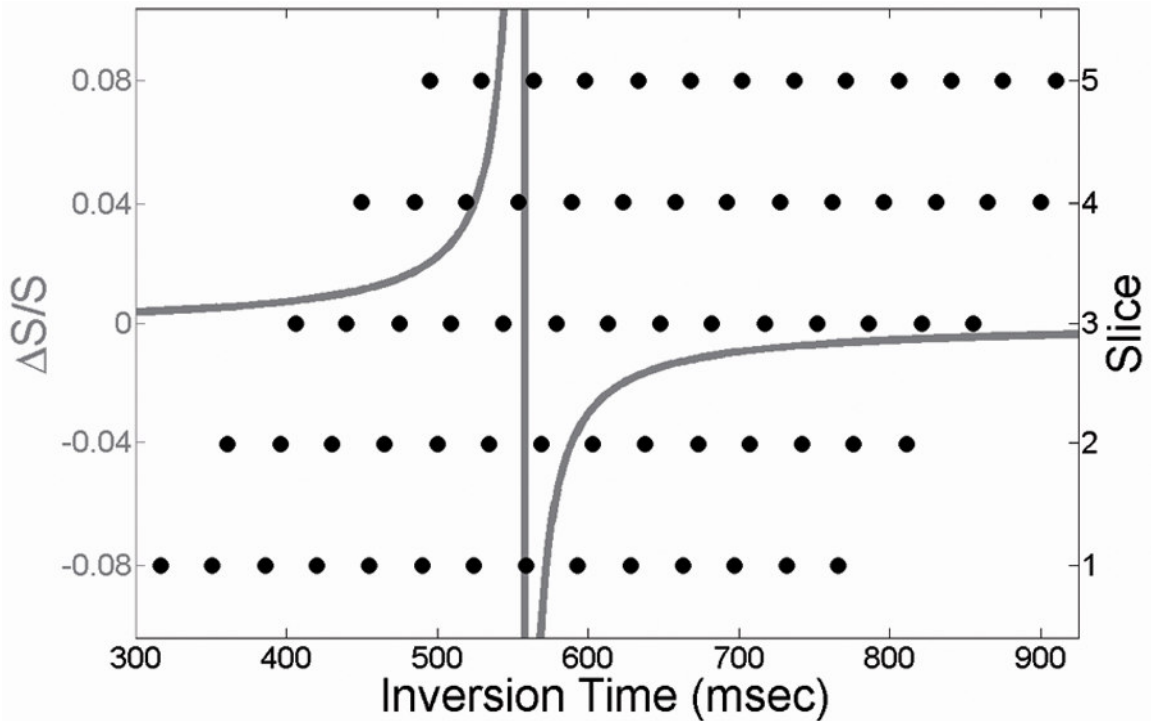


Fig. 3.2: Simulated $\Delta S/S$ for range of TI_1 (gray) and TI_1 coverage for slices 1-5 (black).

3.2.3 Visual Stimulation

Visual stimuli were delivered using a back-projection system (40 degree viewing angle), where a projection screen is installed behind the subject's head while a mirror mounted on a head coil reflects the screen to the subject. A projector equipped with a long throw replacement lens displayed computer input on an in-bore screen. Visual paradigms were programmed in Presentation™ (www.neuro-bs.com), while a serial response box (Current Designs™, www.curdes.com) was used for synchronization with the MR scanner. For each TI₁, stimulus consisted of 24 seconds of fixation on a cross followed by 48 seconds of a flashing checkerboard (8 radial degrees of the visual field) with reversing contrast at 8 Hz and ended with another 20 seconds of fixation.

3.2.4 Data Processing

VASO, CBF and BOLD data were preprocessed and statistically analyzed using SPM2 (Wellcome Department, University College of London, UK). All raw data were corrected for motion before adding (VASO and BOLD) or subtracting (CBF) control and label images. Subtracted images were quantified using the following equation (93):

$$CBF = \frac{\lambda \Delta CBF_{weighted}}{2\alpha_1 M_0 \tau e^{-(TI_2/T_{1,BLOOD})}} \quad [3.3]$$

where $T_{1,BLOOD}$ is the longitudinal relaxation time of blood and τ (700 ms) and TI_2 (1000 ms) are the labeling duration and image acquisition time, respectively. Prior to statistical analysis, CBF and VASO data were spatially smoothed with a 6 mm kernel to improve signal-to-noise ratio (SNR). Data from all 14 scans were used for BOLD analysis but data from only the first 5 scans were used for CBF analysis. This is because when the time between VASO/ASL selective inversion and VASO excitation approaches 700 ms, uninverted blood, critical for ASL contrast, could reach the imaging region and be affected by the VASO excitation pulse. VASO data from each scan (corresponding to each TI_1) were separately analyzed, generating fourteen t-maps with varied BOLD/VASO weighting (positive/negative correlation to task). These individual maps were combined using multiple dataset analysis (24,94) by utilizing the inverse normal cumulative distribution function (Φ) and p-values (P_i) corresponding to test statistics for each voxel from each scan. Specifically, supra-threshold maps from each TI_1 were generated using absolute value (due to TI_1 -dependent BOLD/VASO weighting) of the t-statistic corresponding to $p < 0.05$ before applying

$$T_C = \sum_{i=1}^{N_{maps}} \frac{\phi^{-1}(1-P_i)}{\sqrt{N}} \quad [3.4]$$

where T_C is the cumulative statistic and N_{maps} is the number of individual activation maps included in the calculation. Voxels with a T_C larger than 5 and contiguous cluster size of at least 8 voxels were considered active for the VASO contrast at multiple TI_1 values.

All maps were masked with SNR threshold of 5 derived from VASO data collected at the blood nulling point to exclude large vessel effects (95).

3.2.5 Assessment of Fitting Accuracy

Fitting results and quality were assessed by comparing the results of the original model (24) which assumes $R_{1,BLOOD}$ to be 0.62 and the revised model which assumes $R_{1,BLOOD}$ to a fitting parameter. The inclusion of this additional parameter reduces degrees of freedom. Models were tested for statistical difference by comparing the residual variance of their fits using the “extra sum-of-squares” principle (96):

$$F = \frac{SS_1 - SS_2}{(df_1 - df_2)(SS_2 / df_2)} \quad [3.5]$$

where SS_1 and SS_2 are the sum of squares with degrees of freedom df_1 and df_2 for the current and original models, respectively. The F-ratio is used to assess the decrease in sum-of-squared error relative to decrease in degrees of freedom for the more complex model.

3.2.6 Assessment of CBF – CBV Relationship

As described above, many experiments estimate $CMRO_2$ by deriving stimulus-related CBV and CBF changes with the following equation (20):

$$\frac{CBV}{CBV_0} = \left(\frac{CBF}{CBF_0} \right)^\alpha \quad [3.6]$$

where α is assumed to be 0.38. This relationship can be empirically evaluated by calculating α with relative CBV changes derived from the model and simultaneously acquired relative CBF changes.

3.2.7 Estimation of $CMRO_2$

The multi-compartment model does not rely on calibration or parameter assumption by utilizing CBV to calculate OEF en route to $CMRO_2$ estimation (32). First, this model separates microvasculature into two compartments, arteriolar (a, 30%) and venular (v, 70%). The BOLD signal is therefore described with the equation

$$S \sim 0.3 \cdot x \cdot M_a e^{-R_{2a}^* TE} + 0.7 \cdot x \cdot M_v e^{-R_{2v}^* TE} + (1-x) \cdot M_t e^{-R_{2t}^* TE} \quad [3.7]$$

arteriolar (a)
venular (v)
tissue (t)

where S denotes BOLD signal, x is the water fraction of the blood in the voxel, and M_i and R_{2i}^* ($i=a, v, t$) describe magnetization and transverse relaxation, respectively. Upon neuronal activation, the BOLD signal change can be characterized as follows:

$$\frac{\Delta S}{S} = \frac{0.3 \cdot (\Delta x) \cdot M_a e^{-R_{2a}^* TE} + 0.7 \cdot M_v (x^{act} \cdot e^{-R_{2v}^* TE} - x^{rest} \cdot e^{-R_{2v}^* TE}) + M_t e^{-R_{2t}^* TE} [e^{-\Delta R_{2t}^* TE} (1-x^{act}) - (1-x^{rest})]}{0.3 \cdot x^{rest} \cdot M_a e^{-R_{2a}^* TE} + 0.7 \cdot x^{rest} \cdot M_v e^{-R_{2v}^* TE} + (1-x^{rest}) \cdot M_t e^{-R_{2t}^* TE}} \quad [3.8]$$

In this equation, Δx , the stimulus-induced change in water fraction of blood, is typically obtained from the VASO signal and assumed CBV_{REST} (32,92) as follows:

$$\Delta x = x^{act} - x^{rest} = \left(\frac{C_{par} - CBV_{REST} C_{blood}}{C_{par}} \right) \cdot \frac{\Delta VASO}{VASO} \quad [3.9]$$

where $C_{par}=0.89$ and $C_{blood}=0.87$, the water contents in mL water/ mL substance for parenchyma and blood, respectively, and relating CBV and VASO changes with the following equation (32,92):

$$\frac{\Delta CBV}{CBV} = - \left(\frac{C_{par}}{C_{blood} CBV_{REST}} - 1 \right) \cdot \frac{\Delta VASO}{VASO} \quad [3.10]$$

In the present study, Δx was determined without VASO or assumption of CBV_{REST} using absolute CBV derived from experimental data. These parameters were also used to determine ΔR_{2t}^* as follows:

$$\Delta R_{2t}^* = R_{2t}^{*act} - R_{2t}^{*rest} = 0.7 \cdot \gamma \cdot B_0 \cdot \frac{4}{3} \pi \cdot \Delta \chi \cdot Hct \cdot (CBV_{ACT} \cdot (1 - Y_v^{act}) - CBV_{REST} \cdot (1 - Y_v^{rest})) \quad [3.11]$$

where Hct is the hematocrit fraction of blood in microvasculature (0.36), $\Delta \chi$ is the susceptibility difference between fully oxygenated and deoxygenated blood (0.2 ppm)(24), and B_0 is the strength of the magnetic field (3 Tesla).

Because R_{2a}^* does not change during activation ($Y_a^{rest} = Y_a^{act}$), the only remaining unknown in Eq. 3.8 is R_{2v}^{*act} (assuming $Y_a = 1$ and $Y_v^{rest} = .61$) which can be determined by using the measured BOLD signal change, $\Delta S/S$. This enabled calculation of Y_v^{act} using Eq. 3.11, followed by OEF calculation at both rest and activation using

$$(1 - Y_v) = 1 - Y_a + OEF \cdot Y_a \quad [3.12]$$

and calculating the change in OEF during activation as follows:

$$\Delta OEF = \left(\frac{Y_a - Y_v^{act}}{Y_a} - \frac{Y_a - Y_v^{rest}}{Y_a} \right) \quad [3.13]$$

Task-related change in OEF was normalized to baseline with

$$\frac{\Delta OEF}{OEF} = \left(\frac{Y_V^{rest} - Y_V^{act}}{Y_a - Y_V^{rest}} \right) \quad [3.14]$$

and used in conjunction with normalized ΔCBF to estimate $\Delta CMRO_2$ as follows (32):

$$\left(1 + \frac{\Delta OEF}{OEF} \right) \cdot \left(1 + \frac{\Delta CBF}{CBF} \right) = \left(1 + \frac{\Delta CMRO_2}{CMRO_2} \right) \quad [3.15]$$

Similarly, the single-compartment model (19) was adapted to include CBV measurement as follows:

$$M = \frac{\frac{\Delta BOLD}{BOLD_0}}{1 - \left(\frac{CBV}{CBV_0} \right) \left(\frac{CMRO_2}{CMRO_{2|0}} \right)^\beta \left(\frac{CBF}{CBF_0} \right)^{-\beta}} \quad [3.16]$$

where β is a constant reflecting the influence of deoxyhemoglobin concentration (1.5) and M is typically estimated by inducing hypercapnia (18,19) or hyperoxia (97). While this study did not induce hypercapnia, estimated ΔCMRO_2 from the multi-compartment model is used to solve for M in the single-compartment model.

3.3 Results

For all subjects, robust activation maps were derived from VASO, CBF and BOLD contrasts. As shown in Fig. 3.3, activation for each contrast demonstrated bilateral activation in the occipital lobe, consistent with the flashing checkerboard presented to both visual fields. As expected, BOLD activation was more extensive than CBF and VASO, which are known to have better spatial specificity (22,98). Although this study focuses on quantifying and expanding coverage of the VASO contrast, the ability to maintain CBF and BOLD contrast detection using this method is critical for estimating CMRO_2 (19,91).

Modeling yielded close alignment of experimental and simulated $\Delta S/S$, as demonstrated in Fig. 3.4. In addition to finding fits with low residuals, all estimated parameters were fairly consistent between subjects and within expected ranges (24). For instance, $R_{1,\text{BLOOD}}$ was higher (0.65 ± 0.01) than the intrinsic blood R_1 (0.62) (99) for all

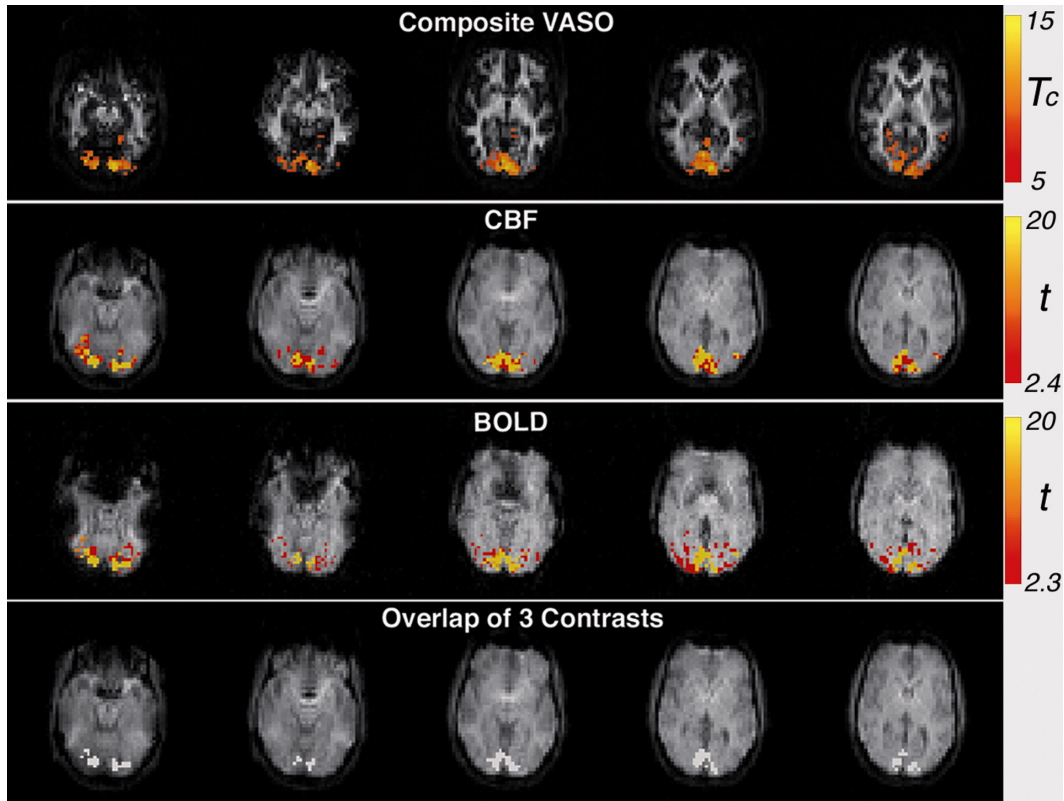


Fig. 3.3: An example of brain activation for the composite VASO, CBF and BOLD contrasts (contiguous voxels > 8 , $T_c > 5$ for VASO, $p < 0.01$ for BOLD and CBF), as well as overlap of all three contrasts (subject 3).

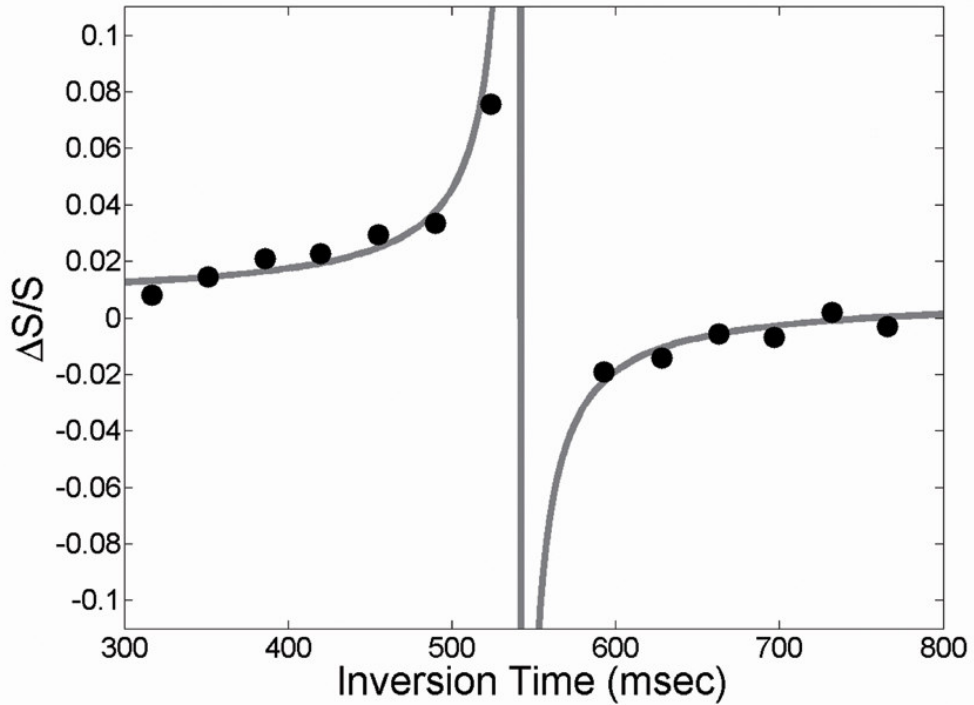


Fig. 3.4: Simulated $\Delta S/S$ for range of TI_1 (gray) and experimental points (black).

subjects, suggesting that the inflow of uninverted blood spins increase the effective relaxation rate (Table 3.1). Estimating CBV with $R_{1,BLOOD}$ set to 0.62 yielded different results. Specifically, CBV_{REST} derived with fixed $R_{1,BLOOD}$ differed from the corresponding values derived by the revised model by -4 to 7%, CBV_{ACT} by -12 to 4% and $\% \Delta CBV$ by -4 to 18%. Relative to the original model, fitting with the revised model was significantly improved for the bottom slice, which is closest to blood inflow, across subjects (F-ratio = 3.9, p-value = 0.05). Across slices, fit for the revised model was significantly improved for subject 1 (F-ratio = 6.3, p-value = 0.02). While differences in other fits were not significant, the revised model consistently reduced sum-of-squared error.

Using this model, absolute CBV values were 7.9 ± 0.3 and 5.6 ± 0.3 mL blood/100 g tissue for CBV_{ACT} and CBV_{REST} , respectively, and $\% \Delta CBV$ was $42.2 \pm 5.4\%$ (Table 3.1). Quantified CBF at rest and during activation were 54.1 ± 18.4 and 110.0 ± 37.9 mL blood/100 g tissue/min, respectively, and relative changes in CBF and BOLD were $103.9 \pm 13.8 \%$ and $1.7 \pm 0.6 \%$, respectively. CBV changes derived from the revised method ($42.4 \pm 5.4\%$) are higher than those derived from CBF changes using Grubb's relationship ($31.0 \pm 3.4\%$) assuming an α of 0.38. This difference can be further probed by calculating α from the modeled CBV estimated measured CBF changes ($\alpha = 0.50 \pm 0.06$).

Table 3.1: CBF, BOLD and model results for CBV_{REST} , CBV_{ACT} , $\% \Delta CBV$, $Y_{B,ACT}$ and $R_{I,BLOOD}$

| Subject | CBF_{REST} (mL blood / 100 mL brain / min) | CBF_{ACT} (mL blood / 100 mL brain / min) | ΔCBF | $\Delta BOLD$ | ΔCBV derived from ΔCBF | α (Based on ΔCBF and model ΔCBV) | CBV_{REST} (mL blood / 100 mL brain) | CBV_{ACT} (mL blood / 100 mL brain) | ΔCBV derived from model | $Y_{B,ACT}$ | $R_{I,BLOOD}$ |
|--------------------|--|---|----------------------|-------------------|---|--|---|--|--|----------------------|--------------------|
| 1 | 63.1 | 119.4 | 89.2% | 1.5% | 27.4% | 0.58 | 5.6 | 8.0 | 44.4% | 0.772 | 0.64 |
| 2 | 36.2 | 79.3 | 119.1% | 1.2% | 34.7% | 0.50 | 5.2 | 7.8 | 48.5% | 0.748 | 0.66 |
| 3 | 75.5 | 159.7 | 111.5% | 2.4% | 32.9% | 0.45 | 6.0 | 8.4 | 39.7% | 0.745 | 0.63 |
| 4 | 41.8 | 81.7 | 95.7% | 1.9% | 29.1% | 0.46 | 5.6 | 7.6 | 36.1% | 0.745 | 0.64 |
| Mean \pm S.D. | 54.1 \pm 18.4 | 110.0 \pm 37.9 | 103.9 \pm 13.8% | 1.7 \pm 0.6% | 31.0 \pm 3.4% | 0.50 \pm 0.06 | 5.6 \pm 0.3 | 7.9 \pm 0.3 | 42.2 \pm 5.4% | 0.753 \pm 0.013 | 0.65 \pm 0.01 |

While the presented model yields a single CBV estimate for group of scans, CBF and BOLD changes are calculated at each time point (Fig. 3.5). A distinct post-stimulus undershoot is evident in BOLD but not CBF, consistent with a previous study of fMRI signal dynamics with visual stimuli (32).

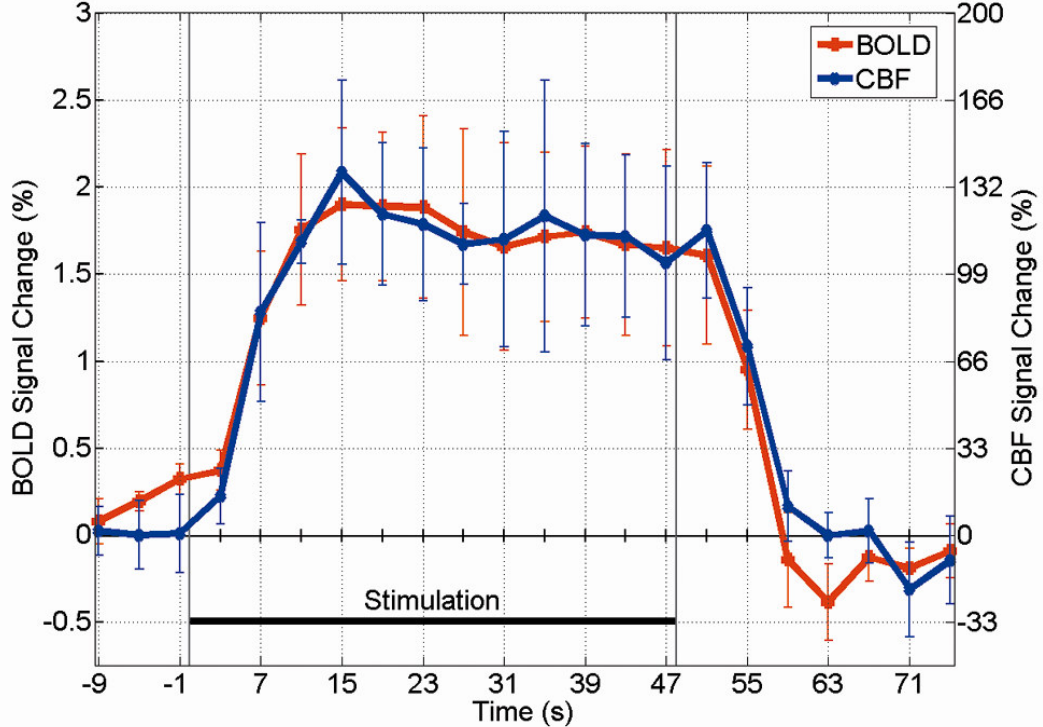


Fig. 3.5: Average time courses for BOLD and CBF ($n=4$).

The multi-compartment model led to $CMRO_2$ values shown in Table 3.2. The average change in $CMRO_2$ (18.7%) is consistent with literature values and variability is consistent with some prior studies (86). Interestingly, estimation of M using these $CMRO_2$ values in the single-compartment model yielded consistent values ($M = 0.05 \pm 0.006$).

Table 3.2: Relative changes in $CMRO_2$ using the multi-compartment model and associated M values from the single-compartment model.

| Subject | $\Delta CMRO_2$ | M |
|---------------------------------------|-----------------------------------|----------------------|
| 1 | 16.9% | 0.051 |
| 2 | 43.3% | 0.057 |
| 3 | 6.8% | 0.047 |
| 4 | 7.9% | 0.043 |
| Mean \pm S.D. | 18.7 \pm 17.0 | 0.050 \pm 0.006 |

3.4 Discussion and Conclusions

This work expands a previous model estimating CBV from VASO by acquiring multiple slices, incorporating simultaneous acquisition of VASO, CBF and BOLD, and accounting for inflow of blood by estimating effective $R_{1,BLOOD}$. The determination of longitudinal blood relaxation based on experimental data can improve accuracy of CBV quantification for the singular VASO sequence and is even more critical for the multi-

echo sequence because a thinner inversion slab, important for CBF detection, is associated increased inflow of fresh blood spins.

In addition to the confounding effect of fresh blood inflow, this method addresses several challenges of the VASO technique including reliance on precise blood signal nulling, assumption of CBV_{REST} to estimate ΔCBV from $\Delta VASO$ and limited slice coverage. First, varying TI accounts for inexact blood nulling; in contrast to traditional VASO, the current method intentionally varies the extent of blood nulling so subject-specific TI is not required. Furthermore, the desire to vary TI enables multiple slices to be acquired. Second, by modeling CBV empirically, this method does not assume CBV_{REST} for the quantification of relative VASO changes. This avoids error related to inter-subject or inter-regional differences and also does not require the use of Grubb's relation.

One recent study utilized global saturation immediately after single slice acquisition to avoid the confounding effect of fresh blood inflow (100). This approach accounts for blood inflow, as the current approach does, but unlike the current method, still relies on assumed CBV_{REST} to estimate ΔCBV from VASO-related changes. Another study also relies on this assumption to quantify ΔCBV and estimate $CMRO_2$ (32). However, this study is also limited by single slice coverage and does not simultaneously acquire CBF and BOLD as the current study does. The study upon which the present method was based varies TI to avoid assumptions of CBV_{REST} , CBF-related changes in CBV and exact blood nulling TI (24). The revised approach builds upon this method by expanding to multiple slices, incorporating simultaneous BOLD and CBF

acquisition and accounting for the inflow of fresh blood spins. Finally, another method quantified CBV using VASO by acquiring images before and after contrast agent injection (101). This presented method is different from this approach because it is noninvasive, allowing for safe repeated measures.

To evaluate the proposed method's ability to quantify CBV without assuming a direct relationship with CBF or absolute CBV_{REST} model results can be compared to previous findings. CBV estimates (~ 7.9 and ~ 5.6 mL blood/100 g tissue for CBV_{ACT} and CBV_{REST} , respectively) and $\% \Delta CBV$ ($\sim 42.2\%$) are slightly higher than the previous study (24) which assumed $R_{I,BLOOD}$ for the model (~ 6.6 and ~ 5 mL blood/100 g tissue for CBV_{ACT} and CBV_{REST} , respectively, and $\sim 32.4\% \Delta CBV$). However, CBV_{REST} estimates are very similar to previously measured values from PET (102) and fMRI (103) studies which both reported baseline CBV of approximately 5.5 mL blood / 100 mL tissue. When typical $\% \Delta VASO$ ($\sim 2.15\%$ in (22)) is used with this value of CBV_{REST} , estimated CBV_{ACT} is in the range of those determined with the present method. Similarly, estimated $Y_{B,ACT}$ (~ 0.753) is within one standard deviation of the original model (0.787 ± 0.059 in (24)). Furthermore, the inclusion of $R_{I,BLOOD}$ improves fitting accuracy to a greater extent than it reduces degrees of freedom, revealing differences in CBV quantification and $\% \Delta CBV$. Fitting the data with the revised model significantly improved fitting for the bottom slice (across subjects) and subject 1 (across slices) demonstrating that some slices and subjects benefit more from this model. Furthermore, because the fitting was not degraded in any subjects or slices, future studies can use this model to improve overall fit quality. Mean sum-of-squared error was lower for the first 3 slices (0.0005) than slices 4 and 5 (0.0009) due to TI ranges that were more balanced

around the blood nulling point. Future studies can acquire 14 slices using a similar protocol (14 separate scans) each with a different slice order (scan 1: slice 1 first; scan 2: slice 2 first; etc.) to provide a balanced and consistent TI coverage with further expansion of slice coverage and empirical determination $R_{1,BLOOD}$.

While higher $R_{1,BLOOD}$ can be attributed to the inflow of fresh blood resulting in an increase in *effective* $R_{1,BLOOD}$ there are reasons inherent $R_{1,BLOOD}$ could also be different. Typically, longitudinal blood relaxation is based on bovine blood matched for common human Hct levels which are typically 0.38 to 0.46 in humans (99,104). However, actual $R_{1,BLOOD}$ is dependent on the exact Hct level which could vary between subjects. Modeling $R_{1,BLOOD}$ is particularly useful when Hct levels are unknown in certain populations, as studies have found altered Hct in patients with cardiac disease (105) and hypertension (106). Furthermore, that study found temperature to affect relaxation times ~ 20 ms/ $^{\circ}$ C so scanner temperature can play a role in relaxation rates. Also, radiation damping can increase $R_{1,BLOOD}$ which can be more problematic as fMRI experiments are conducted at higher fields. While dephasing could reduce the effect of damping (99), there still will be damping during the delay of the RF pulse and the spoiling gradient (107). For these reasons, it is difficult to compare $R_{1,BLOOD}$ to published values; uncertainty of longitudinal blood relaxation suggests that empirical derivation of $R_{1,BLOOD}$ is appropriate.

Quantified CBF at rest (~ 54.1 mL blood/100 g tissue/min) was slightly lower than gray matter CBF in a similar experiment (~ 66.4 and ~ 67.2 mL blood/100 g tissue/min using multi-echo and traditional ASL in (23)) but similar to another fMRI study using a

separate labeling coil (48 – 62 mL blood/100 g tissue/min in (108)) which has better SNR due to the absence of magnetization transfer (MT). ROIs in this chapter contained some white matter voxels which have lower CBF (25.2 and 24.6 mL blood/100 g tissue/min using multi-echo and traditional ASL, respectively, in (23)), resulting in lower CBF_{REST} . Relative change in CBF (~104 %) was higher than the previous study (~50-80 % for both multi-echo and traditional ASL in (23)). In addition to lower baseline CBF, higher $\% \Delta CBF$ in this chapter could be attributed to a thinner inversion slab (125 mm) relative to the previous study (150 mm in (23)).

Assessing the CBF-CBV relationship, α was found to be 0.50 ± 0.06 , while it is typically assumed *a priori* in other studies (0.38 in (20) or 0.50 in (109)). The consistency between the derived α with those measured or assumed in other studies validates the approach in situations where the assumed value may be inaccurate, such as in elderly or patient populations. $CMRO_2$ estimates (18.7 ± 17.0 %) were within the range and inter-subject variability of previous studies (6 to 48% in (86)). The ability to experimentally determine ΔCBV without assuming a CBF-CBV relationship could reduce uncertainty in $CMRO_2$ estimation. In addition, this model does not require assuming the value of CBV_{REST} . A more comprehensive comparison between $CMRO_2$ estimation methods with more subjects will be required to appropriately validate this approach.

The present method enables quantitative VASO imaging with simultaneous CBF and BOLD image acquisition. This approach is less reliant on assumptions related to CBV quantification and accounts for the fresh inflow of uninverted blood. Future

applications can involve more subjects to quantify CBV in conjunction with CBF and BOLD measurement to better understand CMRO₂ estimation accuracy.

CHAPTER 4

SIMULTANEOUS ACQUISITION OF GRADIENT ECHO / SPIN ECHO BOLD AND PERFUSION WITH A SEPARATE LABELING COIL²

As described in previous chapters, arterial spin labeling (ASL) to measure cerebral blood flow (CBF) complements blood oxygenation level dependent (BOLD) contrast with a measure that is more quantitative and has better specificity to neuronal activation. Recent advances improve low signal-to-noise ratios (SNR) of ASL by using a separate labeling coil to improve arterial labeling efficiency and to minimize magnetization transfer (MT) effects. First, an inexpensive and programmable RF transmitter for two-coil continuous arterial spin labeling (CASL) system is presented in this chapter. Unlike previous implementations of two-coil CASL which require expensive magnetic resonance (MR) radio frequency (RF) instruments, the presented design utilizes a low-cost system on chip (SOC) direct digital synthesizer (DDS) and a mini-size communication RF power amplifier to generate the labeling RF waveform without sacrificing RF performance. Compared with a single RF channel two-coil CASL

² Partial work in this chapter has been published as “Xu Q, Glielmi C, Zhou L, Choi K, Hu X. An inexpensive and programmable RF transmitter setup for two-coil CASL. Concepts in Magnetic Resonance Part B (Magnetic Resonance Engineering) 2008;33B(4):228-235.” Reprinted with permission of Cadmus Communications.

approach, this design requires minimal scanner hardware modifications. Moreover, this design offers a programmable interface for easy sequence setup and debugging. Performance and ease of use are validated experimentally.

Second, image acquisition with this labeling coil is enhanced to simultaneously acquire two BOLD contrasts. While the CBF contrast is better aligned with neuronal events and more reproducible than BOLD, simultaneous ASL and spin echo (SE) BOLD have not been compared. Relative to gradient echo (GE) BOLD, SE BOLD is less biased to draining veins and is more localized to intravascular space than extravascular regions. This chapter mainly focuses on a new pulse sequence that simultaneously acquires ASL with a separate labeling coil, GE BOLD and SE BOLD. Simultaneous acquisition reduces inter-scan variability to improve evaluation of each contrast's relative specificity and reproducibility. Furthermore, it facilitates studies that would benefit from complementary measures.

4.1 Introduction

Pulsed (PASL) and continuous arterial spin labeling (CASL) are established MRI perfusion imaging tools, allowing for noninvasive assessment of brain function and pathology (110). Compared with single coil CASL (111), in which a single coil is used for labeling and excitation, CASL with a separate labeling coil (two-coil) has the advantages of higher SNR, oblique slice orientation, reduced RF power deposition, and absence of MT effects (112-114).

Most implementations of two-coil CASL (112-114) require two independent sets of proton RF channel and amplifier, a hardware requirement that is not currently available on most clinical MRI scanners. Consequently, implementation of two-coil CASL often requires the availability of costly commercial RF instruments such as MR RF power amplifiers. This substantial RF hardware cost has impeded expansion of two-coil CASL in research and clinically-oriented applications.

One inexpensive alternative implementation of two-coil CASL is to utilize the RF channel and amplifier on the scanner by inserting a high-power RF switch between the scanner RF power amplifier and the coil system (115). This approach splits the RF power into a low-power labeling period (for carotid blood inversion) and a high power excitation period (for image acquisition) in the time domain. Although this implementation significantly reduces cost, it is limited by the maximum RF-on time permitted on clinical scanners causing suboptimal labeling efficiency. More importantly, it requires scanner RF chain hardware modifications, which vary by scanner and are quite complicated.

The first part of this chapter describes an alternative inexpensive solution for two-coil CASL with minimal scanner hardware modifications, using a system-on-chip (SOC) direct digital synthesizer (DDS) (116) and mini-size communication RF power amplifier. The programmable DDS technique facilitates setup and debugging of the CASL sequence. This design is also simple and fully integrated, requiring minimal cost. Additionally, utilization of a communication RF power amplifier instead of an expensive MR RF power amplifier further reduces cost. While design conception and hardware

development was performed outside the scope of this dissertation, application of this approach for functional neuroimaging and assessment of data quality consist of the first innovative aspect of this chapter.

After confirming ease of utilization and image quality of data acquired with two-coil CASL using a stand-alone SE sequence that only acquires one contrast, the second part of this chapter seeks to enhance image acquisition by complementing CBF with GE and SE BOLD contrasts. Each BOLD contrast can be used to study hemodynamics related to task performance by detecting changes in deoxyhemoglobin levels near the site of neuronal activity (1). BOLD contrast using fMRI has been the most prominent functional neuroimaging method for the last 15 years due to its high sensitivity and ease of use. However, the BOLD signal is dependent on a combination of physiological parameters, including CBF, cerebral blood volume (CBV) and cerebral metabolic rate of oxygen ($CMRO_2$) and therefore produces relative, not absolute results that vary longitudinally for reasons outside the realm of neuronal activity dynamics (7). Furthermore, the magnitude of the signal change is largely dependent on brain vasculature because GE BOLD signal originates from the venous concentration of deoxyhemoglobin so “activation” may be aligned more with draining veins than actual neuronal populations (8). The attribute that enables BOLD contrast, paramagnetism, produces a bulk susceptibility difference between the vessels and surrounding tissue resulting in extravascular contribution. While this improves GE BOLD sensitivity, spatial resolution of activation is not as specific as methods using other means of contrast such as CBF (8) or SE BOLD (117). Alternative acquisition methods that are less biased

to draining veins, such as ASL (10-15,17), SE BOLD at higher fields (117) and at 3 Tesla (118,119) can be primary or complementary measures for functional studies.

SE BOLD acquisition refocuses static dephasing that occurs around large vessels so its contrast results from dynamic dephasing associated with smaller vasculature (120-122). At higher fields, improved spatial specificity of SE BOLD relative to GE BOLD is even more pronounced due to shorter T2 of venous blood as static magnetic field increases (117,123,124). Even at 3 Tesla, SE BOLD has also been shown to be more specific to neuronal dynamics, as previous studies have acquired high resolution SE BOLD (119) for experiments requiring a high degree of spatial localization (118).

Non-invasive measurement of CBF with ASL is more quantitative and has better specificity to neuronal activation relative to BOLD (111). Specifically, ASL uses magnetically labeled arterial blood water as an endogenous tracer for measuring CBF (10-19). Recent advances improve low SNR of ASL by using a separate labeling coil to improve arterial labeling efficiency and to minimize MT effects (108,125).

While CBF is better aligned with neuronal events (25) and more reproducible (7) than BOLD, simultaneous ASL and SE BOLD have not been compared. However, one study utilized a single imaging sequence to separately acquire SE BOLD and CBF at 4 and 7T (117). This study demonstrated millimeter and submillimeter spatial specificity of each contrast, improved detection with higher magnetic field and reproducibility under repeated measures. The ability to simultaneously acquire these contrasts would provide a better basis for comparison between the contrasts.

Acquisition of multiple readouts can optimize acquisition parameters for different contrasts while acquisition with a single readout for CBF and BOLD contrasts consists of tradeoff for each contrast's optimal echo time (TE). Furthermore, simultaneous acquisition reduces inter-scan variability to improve evaluation of each contrast's relative specificity and improves scanning efficiency for studies that would benefit from complementary measures. One approach utilizes two readouts with ASL, minimizing TE for CBF (reducing BOLD contamination) and optimizing TE for GE BOLD (matching to gray matter T2*). Double readout ASL acquisition has been used for both EPI (88) and spiral (126) readouts. ASL with two readouts was enhanced in a recent study measuring the CBV-weighted vascular space occupancy (VASO) contrast (22) in conjunction with a second excitation followed by ASL and GE BOLD readouts (23). However there have been no studies implementing simultaneous ASL and SE BOLD acquisition, two measures that will be increasingly applied as fMRI studies progress to higher magnetic fields.

After validating the feasibility and quality of an inexpensive two-coil CASL system, this chapter presents a new pulse sequence that simultaneously acquires ASL with a separate labeling coil, GE BOLD and SE BOLD. This approach optimizes imaging parameters for each contrast, demonstrating reliable acquisition of each contrast during a visual stimulation paradigm. In addition to demonstrating robust activation for each contrast, SNR and CBF quantification is compared to the more traditional stand-alone SE ASL. Finally, potential applications of this acquisition approach are explored. Specifically, inter-subject variation, linear coupling of stimulus-related signal changes between contrasts and proximity to large vessels are assessed for each contrast.

4.2 Background and Previous Developments

The separate labeling coil used in this chapter provides an inexpensive and easily programmable means for two-coil CASL. Design and construction was performed by Dr. Qin Xu of the Biomedical Imaging Technology Center at Emory University. Background of hardware design (125) is described before this chapter presents new developments focusing on evaluating data quality and enhancing image acquisition to include multiple contrasts.

4.2.1 Labeling Coil Design

Figure 4.1 shows the schematics and the photograph of the setup for gating a continuous wave RF output during the labeling period and to detune the coil after labeling. The setup requires only two inputs from the scanner. First, a 10-MHz reference signal ensures that the labeling RF is coherent with the scanner center frequency. Second, the scanner transistor–transistor logic (TTL) triggering signal is used to control the labeling timing. In this chapter, TTL is referred to as “triggering signal” and the RF triggered by this TTL as “labeling signal.”

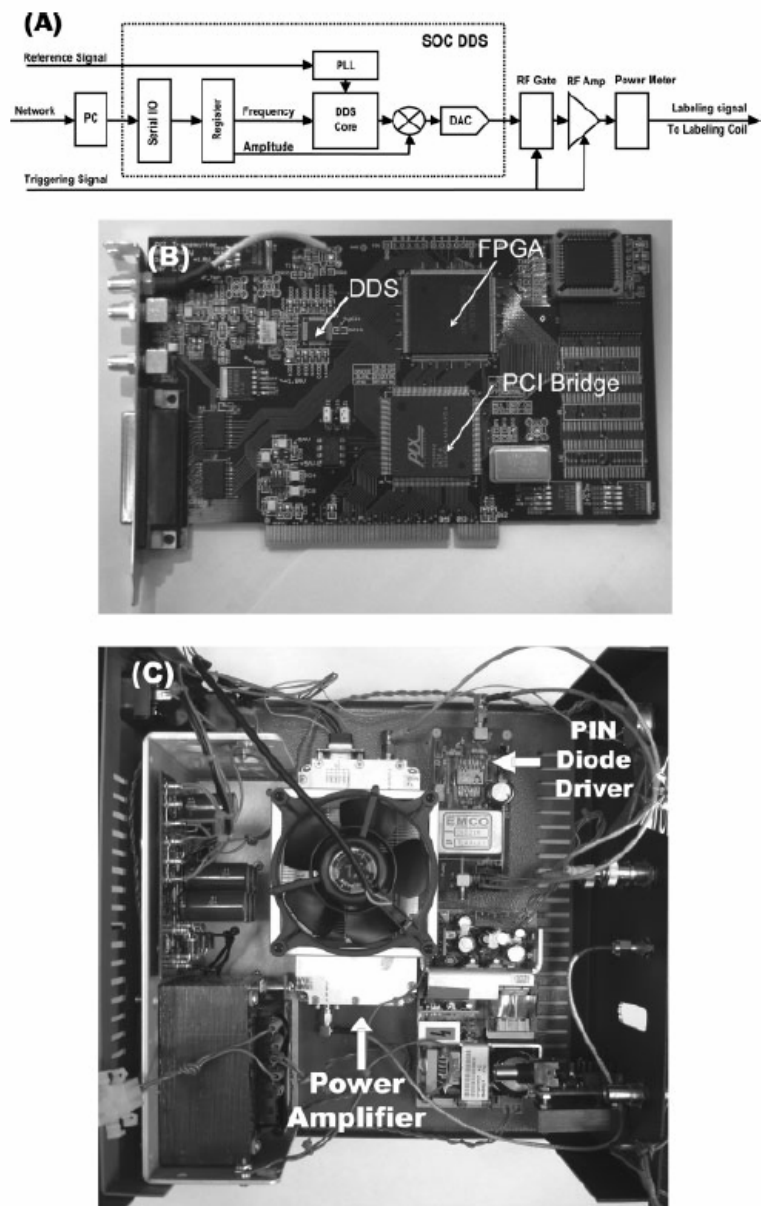


Fig. 4.1: (A) The hardware block diagram of the two-coil CASL system (B) A photograph of the homebuilt DDS RF transmitter. (C) A photograph of RF power amplifier and PIN diode driver.

A newly introduced integrated circuit (IC), AD9954 (Analog Devices, Norwood, MA), is used to generate the labeling RF signal. The DDS core in the AD9954 provides 32-bit frequency resolution (0.01 Hz tuning steps) and 14-bit phase resolution (0.028 tuning steps) for a sinusoidal output in the digital domain. A 400 mega samples per second (MSPS) digital-to-analog converter (DAC) is used to convert the digital signal to an analog RF waveform. The output frequency can range from DC to 180 MHz when referenced to a 400-MHz system clock, covering Larmor frequencies for fields up to 4 T. An amplitude modulation block is inserted between the DDS core and the DAC enabling control of RF output amplitude. A 14-bit digital amplitude scaling register and a digital multiplier are integrated in this amplitude modulation block. The value of this register that is used to scale the RF signal amplitude can be provided by control software according to the arterial labeling power. The DDS chip is driven by the 10-MHz external reference clock from the scanner console. Because the frequency of this reference is lower than 20 MHz, the minimum allowable reference input for AD9954, a passive coaxial frequency multiplier (Model: MK-2, Mini-Circuits, Brooklyn, NY) is used to convert the scanner 10-MHz signal to meet the AD9954 reference input specification. An onboard phase-lock loop (PLL) in AD9954 is used to permit the multiplication of the reference clock 20 times to 400 MHz.

This SOC chip also provides a flexible 4-line serial configuration protocol allowing programming with a computer parallel/serial port or microcontroller unit (MCU). In this implementation, this DDS is connected to a Pentium III control personal computer (PC) via PCI bus. A PCI9052 (PLX tech, Sunnyvale, CA) and a Spartan II (Xilinx, San Jose, CA) Field Programmable Gate Array (FPGA) are used for data transfer

and logic control between the DDS and the PC. This computer is remotely controlled by the scanner's host computer through a network (Microsoft remote desktop connection). On the control PC, a program written in C++ automatically calculates the desired labeling frequency according to

$$f_{labeling} = f_0 + \gamma G \Delta r \quad [4.1]$$

where f_0 is the center resonance frequency of the scanner γ is the gyromagnetic ratio of proton, G is the labeling gradient, and Δr is the distance between centers of the labeling coil and scanner field. The program subsequently configures the DDS by storing the frequency tuning word (FTW) in the DDS frequency register using

$$FTW = (f_{labeling} \times 2^N) / SYSCLK \quad [4.2]$$

where N is the frequency resolution (32 bits in present design) and $SYSCLK$ is the system clock. The labeling RF power is also controlled by this program as the scaled RF signal

$$S(t) = A \cdot \cos(2\pi f_{labeling} t + \theta) \quad [4.3]$$

where A is the amplitude controlled by a 14-bit digital register in AD9954 and θ is the initial phase offset of the DDS. Instead of manually adjusting the RF in the MR equipment room as previous implementations (112-114) required, the program allows remote control of the labeling RF parameters from the scanner console.

The SOC chip contains all the necessary functional blocks including DDS Core, high speed DAC, amplitude modulation block, PLL and serial configuration port integrated into a single chip. In addition, it can provide 95 dB spur free dynamic range at 1 MHz span and -110 dBc/KHz phase noise performance. Compared with costly commercial RF instruments, this single chip design significantly reduces the cost of the labeling system without sacrificing the RF signal quality.

Following the DDS, a single-pole double-throw RF switch with 80dB isolation capability at 120 MHz (AD8180, Analog Devices, Norwood, MA) is used to gate the RF signal. This switch is controlled by the triggering signal from the scanner. Subsequently, the RF signal is filtered and amplified by a 120 MHz center frequency band pass filter and a mini-size 10 MHz – 500 MHz 10-Watt power amplifier (Model: HD17070, HD Comm. Corp, NY). The labeling RF is delivered to the labeling coil through a power meter. A webcam (Model: VX3000, Logitech Inc, Fremont, CA) remotely monitors the value of the power meter through the network. As a result, the user can conveniently monitor the RF power to ensure safety throughout the scanning duration.

The circuit diagram of the labeling coil is shown in Fig. 4.2. The individual coil loops (L1) containing series coupling capacitors (C1, C2 and C3) are tuned by a variable capacitor (C4). Variable capacitors C5 and C6 are used for coil matching. The PIN diode actively switches the coil between labeling (tuned) and isolated (detuned) working states according to the triggering signal from the scanner. Inductor L2 and capacitor C4 form a parallel resonance circuit to detune the coil when the PIN diode is short circuited. A single chip PIN diode driver (Model: 9351, Impellimax Inc, Nashua, NH) is used to transfer the triggering pulse from TTL protocol to a +5V/-12V PIN diode switching

signal. To prevent RF interference with the PIN diode driver, RF chokes are placed in series with the control signal loops. All of the electronic components and coil loops are placed on one side of the printed circuit board (PCB). To ensure subject safety, all components are shielded by high impedance plastic covers. The Q factor of the labeling coil and the insertion loss of the coaxial cables were measured using a network analyzer (Model: 8753D Hewlett Packard, Palo Alto, CA).

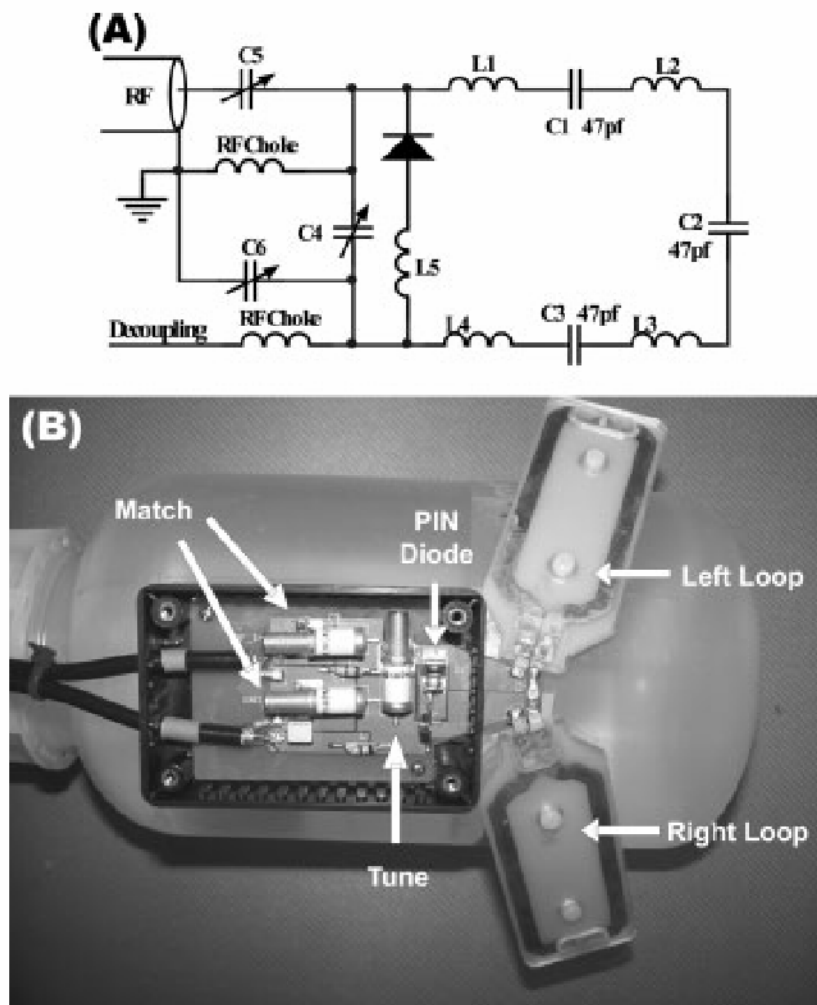


Fig. 4.2: (A) and (B) present the circuit diagram and the butterfly surface labeling coil, respectively.

4.3 Methods

One healthy subject (29 years) and five healthy male subjects (27-32 years) were scanned for stand-alone SE and simultaneous sequence initiatives, respectively. All recruiting and scanning conformed to guidelines set by the Emory University Institutional Review Board.

4.3.1 Image Acquisition

Data were acquired on a Siemens 3 Tesla Tim Trio scanner (Siemens Medical Solutions, Erlangen, Germany) utilizing a volume TEM head coil for excitation and reception of the images. A homebuilt 65 mm \times 30 mm de-tunable butterfly surface labeling coil was placed on the neck approximately 18 cm away from the isocenter of the scanner to continuously invert the blood flowing bilaterally in the carotid and vertebral arteries.

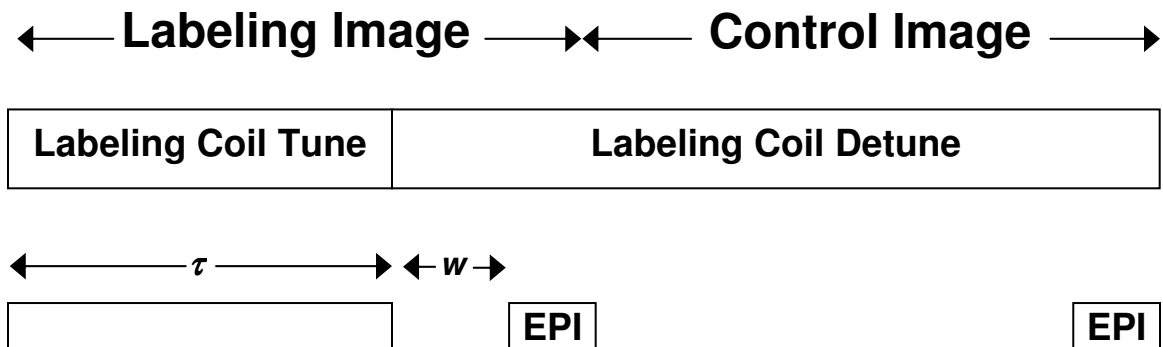


Fig. 4.3: Two-coil CASL stand-alone SE sequence diagram. RF labeling applied during τ period is followed by a post-labeling delay (w) before a multislice SE EPI acquisition. The labeling coil is only tuned in the τ period.

4.3.1.1 Image Acquisition: Data Quality Validation of Stand-Alone SE Sequence

To evaluate the two-coil CASL system, two types of scans were acquired in a healthy 29 year old male subject. Both utilized a stand-alone SE sequence acquiring a single CBF-weighted contrast (TR/TE = 4.4 s/27 ms, FOV = 25 cm, resolution = 64 x 64, slice thickness = 5 mm, 11 ascending slices). A diagram of the two-coil CASL sequence is shown in Fig. 4.3. Labeled (applying RF before acquisition) and control images (no applied RF) are interleaved. Adiabatic flow driven RF labeling (127) was achieved with a 3 second pulse with a simultaneous 2.5 mT/m labeling gradient and was followed by a post labeling delay (w) of 700 ms. All pulse sequences utilized EPI readouts and were programmed in the Siemens IDEA environment.

First, a resting scan was acquired with 60 averages (120 images raw images in 8.8 minutes) covering the sensorimotor cortex while the subject closed his eyes. Second, a functional scan was acquired with 80 perfusion images (160 images raw images in 11.7 minutes) covering the visual cortex.

4.3.1.2 Image Acquisition: Simultaneous Sequence

Once data quality of the stand-alone SE sequence was confirmed, a simultaneous sequence acquiring CBF, GE BOLD and SE BOLD was developed and evaluated in a separate study consisting of 5 subjects. First, 5 minute resting scans were acquired using the stand-alone SE CBF sequence (125) as well as a simultaneous sequence (Fig. 4.4). Both sequences acquired 5 ascending slices using a TR of 4500 ms, 3.43 x 3.43 x 5 mm

resolution covering 75% of k-space with TE1/TE2/TE3 of 12/35/105 ms (simultaneous sequence) and TE of 27 ms (stand-alone SE CBF). Subjects were instructed to close their eyes during the resting scans and both sequences were used to assess resting CBF and SNR for the simultaneous sequence relative to standard CBF acquisition with a single readout. Arterial blood was labeled with the same home-built butterfly labeling coil (125) (labeling duration of 3 s, post-label delay of 700 ms) and control and labeled images were interleaved. For the simultaneous sequence, two acquisitions for CBF and GE BOLD were acquired at short and long TE, respectively. After a subsequent 180° refocusing pulse, the SE BOLD image was acquired. Echo times were optimized for each contrast; CBF utilized the shortest possible TE to minimize BOLD contamination, GE BOLD matched TE to gray matter T2* and SE BOLD readout is symmetric about the echo (to minimize extravascular sensitivity) at a TE close to gray matter T2. Following the two resting scans, four scans were acquired with the simultaneous sequence during visual stimuli using the same imaging parameters as the resting scan. Finally, a T1-weighted anatomical image was acquired with 1 mm³ resolution.

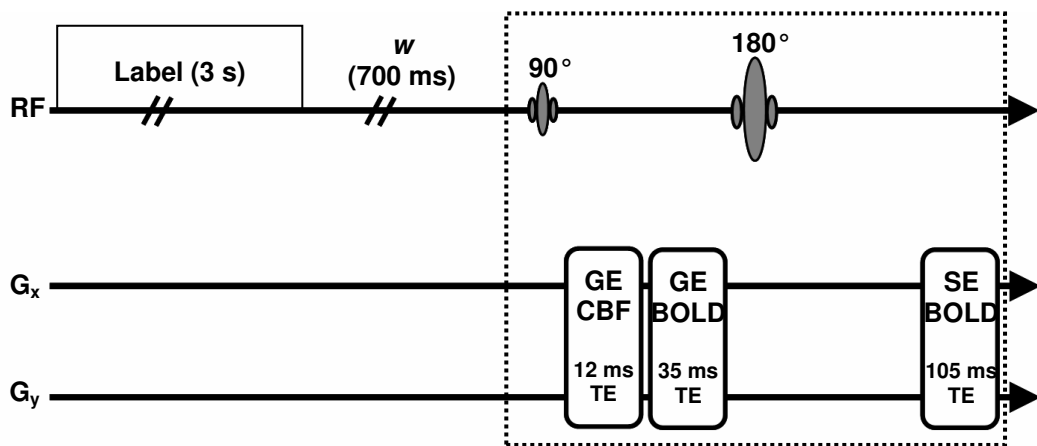


Fig. 4.4: Simultaneous sequence acquires CBF, GE BOLD and SE BOLD following a 3 second label and 700 ms post-label delay (w).

4.3.2 Visual Stimuli

Visual stimuli were presented using a block design with a flashing checkerboard covering 8 radial visual field degrees and reversing contrast at 8 Hz. For the first initiative, stand-alone SE data evaluation, four 88 second fixation blocks were interleaved with four 88 second blocks of flashing checkerboard stimulus. For the second initiative, simultaneous sequence validation, each scan consisted of two 63 second fixation blocks interleaved with two 63 second visual stimuli blocks.

4.3.3 Data Analysis

All functional data were analyzed using SPM2 (Wellcome Department, University College of London, London, UK) and custom MATLAB (MathWorks, Natick, MA).

4.3.3.1 Preprocessing and Analysis: Stand-Alone SE Evaluation

Following motion correction, control and labeled images were subtracted for CBF and quantified under the assumption that MT was absent using (128)

$$CBF = \frac{\lambda \Delta S}{2\alpha_1 T_{1,BLOOD} M_0} \cdot \frac{1}{e^{ATT/T_{1,GRAY}} e^{-(w-ATT)/T_{1,GRAY}} (1 - e^{-\tau/T_{1,BLOOD}})} \quad [4.4]$$

where λ is the water brain-blood partition coefficient, ΔS denotes the difference between control and labeled images, α_i represents labeling efficiency, $T_{1,GRAY}$ is the longitudinal relaxation of gray matter, M_0 is the equilibrium magnetization of the brain, ATT is the arterial transit time, $T_{1,BLOOD}$ is the T1 of arterial blood, τ is the labeling duration and w is the slice-specific post-labeling delay. M_0 was approximated by the control images and α_i of 0.75, $T_{1,GRAY}$ and $T_{1,BLOOD}$ of 1.33 and 1.49 s, respectively (113), λ of 0.98 ml/g (129) and ATT of 0.98 s (130) were used.

Next, all functional data were coregistered to the corresponding high resolution anatomical image, normalized to an MNI template and spatially smoothed (6 mm FWHM kernel). For resting scans, CBF data were masked with segmented anatomical gray matter mask. Resting CBF data for gray matter voxels was assessed for each sequence by quantifying resting CBF and calculating SNR with mean control – label (ΔS) divided by the mean control signal ($S_{CONTROL}$). Functional data were analyzed using a general linear model (GLM) with correction for a false discovery rate (FDR) using a threshold of $p < 0.05$ (85).

4.3.3.2 Preprocessing and Analysis: Simultaneous Sequence Evaluation

All CBF data acquired with the stand-alone SE and simultaneous sequences in this initiative were preprocessed using the same steps as the stand-alone SE data evaluation with two exceptions: data were smoothed with 5 mm FWHM kernel due to smaller in-plane resolution and activation maps were also generated in original image space to avoid potential interpolation confounds when converting images to MNI space.

Similarly, SE and GE BOLD data were motion corrected; control and labeled images were added, normalized to MNI space, spatially smoothed (5 mm FWHM kernel). SPM2's GLM was applied to smoothed data in original and MNI coordinates. Additionally, the GLM was applied to unsmoothed data in MNI space to evaluate overlap of activation with voxels containing large vessels.

4.3.4 Region of Interest (ROI) Selection: Simultaneous Sequence Data

For data acquired in the second experimental phase (simultaneous sequence validation) two methods of ROI selection were used for analysis of task-related data. First, CBF activation was determined using a threshold of $p < 0.05$ with FDR correction (85). This ROI provided a “CBF localizer” for each subject and contrast. ROI selection based on CBF is known to be more specific to neuronal activity than BOLD and has been shown to reduce variation of CBF and BOLD signals (87). Second, SE and GE BOLD ROIs were estimated by matching suprathreshold voxel counts to the CBF localizer for each subject. These ROIs served as the “matched voxel count localizer” for each subject.

4.3.5 Assessment of Reproducibility

Inter-subject variation for relative signal changes were evaluated for each contrast. Mean signal changes between visual stimuli and rest were calculated for each subject and contrast using both the CBF and matched voxel count localizers. Coefficient of variation (CV) was calculated across subjects for each contrast (7):

$$CV_{INTER} = (100\%) \cdot \frac{\sigma_i}{x_{avg}} \quad [4.5]$$

Where x_{avg} and σ_i are the average and standard deviation of percent signal change across subjects for a given contrast.

4.3.6 Assessment of Linear Coupling

For data acquired with the simultaneous sequence, the relationship of relative signal changes between contrasts was compared across subjects. To increase the number of data points for linear fitting, each subject's activation was divided into two ROIs (left and right occipital lobe). For each ROI approach and pair of contrasts, linear regression analysis was applied and the extent of linear coupling was assessed.

4.3.7 Proximity to Large Vessels

Center of gravity coordinates were calculated as the weighted average (by t score) of each subject's MNI activation maps for each contrast. Voxels containing large veins are known to have high variance due to changing levels of CBF and CBV and low signal intensity due to relatively high deoxyhemoglobin levels (131-133). To select voxels that contain large vessels, voxel-wise variance maps normalized to mean intensity were calculated for resting state GE BOLD data in MNI space (133). The top 5% of these voxels were identified as "high-variance" and used as a mask for large vessels. Next, Euclidean distance from center of gravity coordinates to the closest large vessel was

calculated for each subject and contrast to assess proximity of each contrast to large vessels. Finally, paired two-tailed t-tests of these distances were used to assess significance for each pair of contrasts using a threshold of $p < 0.05$. Similarly, percent overlap between activation and large vessel maps were compared for each subject and contrast.

4.4 Results

4.4.1 Results: Stand-Alone SE Data Validation

The circuit and coil were evaluated on the bench prior to connection to the scanner. The insertion loss of the coaxial cable from power meter to the coil was 3 dB. The actual RF power delivered to the labeling coil was approximately 1.4 W. The unloaded and loaded Q factors of the surface labeling coil were found to be ~75 and ~40, respectively. Therefore, approximately 47% of the RF power applied to the coil was deposited in the tissue (134) which is well below FDA safety regulations.

Figure 4.5 presents the resting state perfusion-weighted imaging results. For gray matter, the mean ratio of the subtracted image to the control image ($\Delta S/S_{CONTROL}$) is 0.95% reflecting similar SNR to other two-coil systems (0.4-1.3% (114) and 0.8% (112)). Average gray matter CBF was 52.6 ml/100g/min, within previously reported physiological range (80 ml/100g/min (114) and 48-62 ml/100g/min (113)). Fig. 4.6 shows the visual activation results from the same volunteer. As expected, suprathreshold

voxels are located in the occipital regions of both hemispheres, consistent with the bilateral visual stimuli. The absence of spurious activation in unrelated brain regions also confirms the specificity of CBF to brain function, demonstrating the applicability of current system to functional studies.

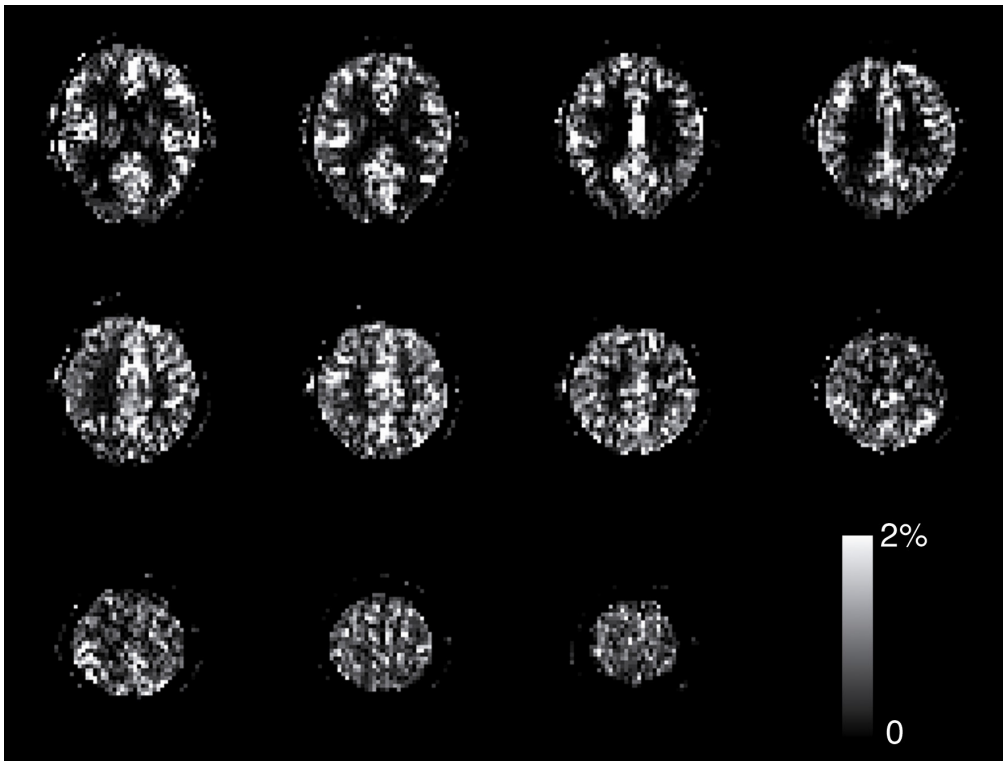


Fig. 4.5: $\Delta S/S_{CONTROL}$ for resting state data acquired with stand-alone SE sequence.

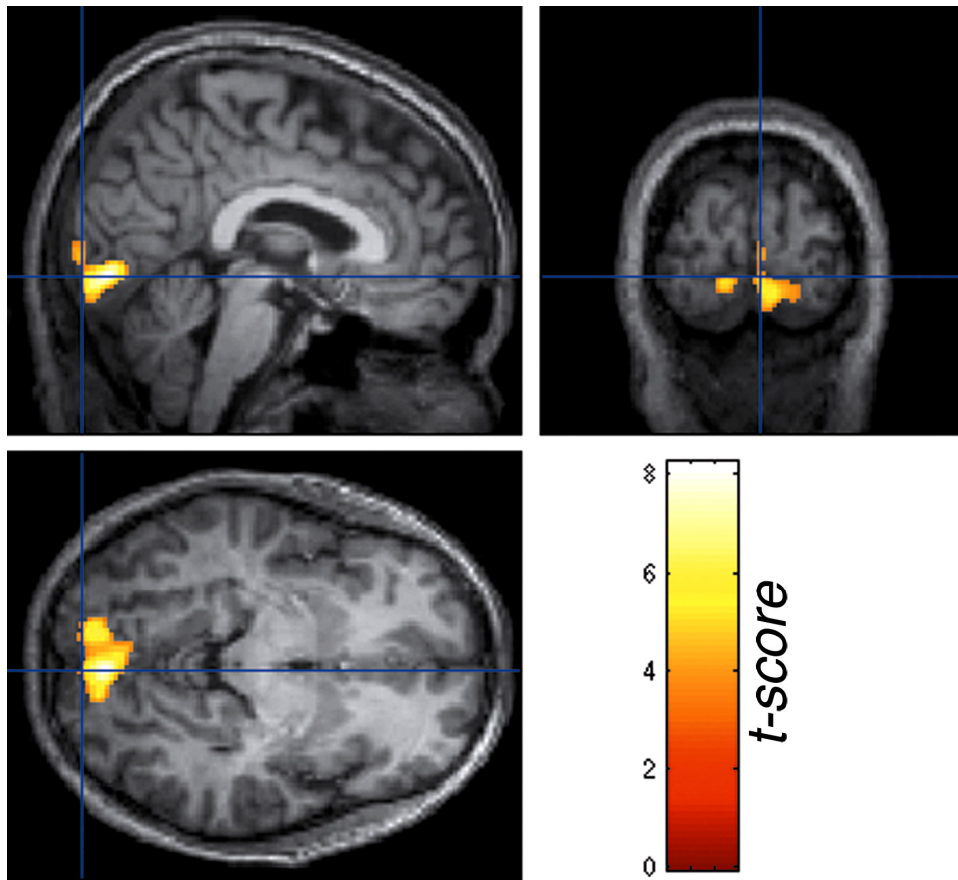


Fig. 4.6: Activation in visual cortex from 8 Hz flashing checkerboard presented to bilateral visual field.

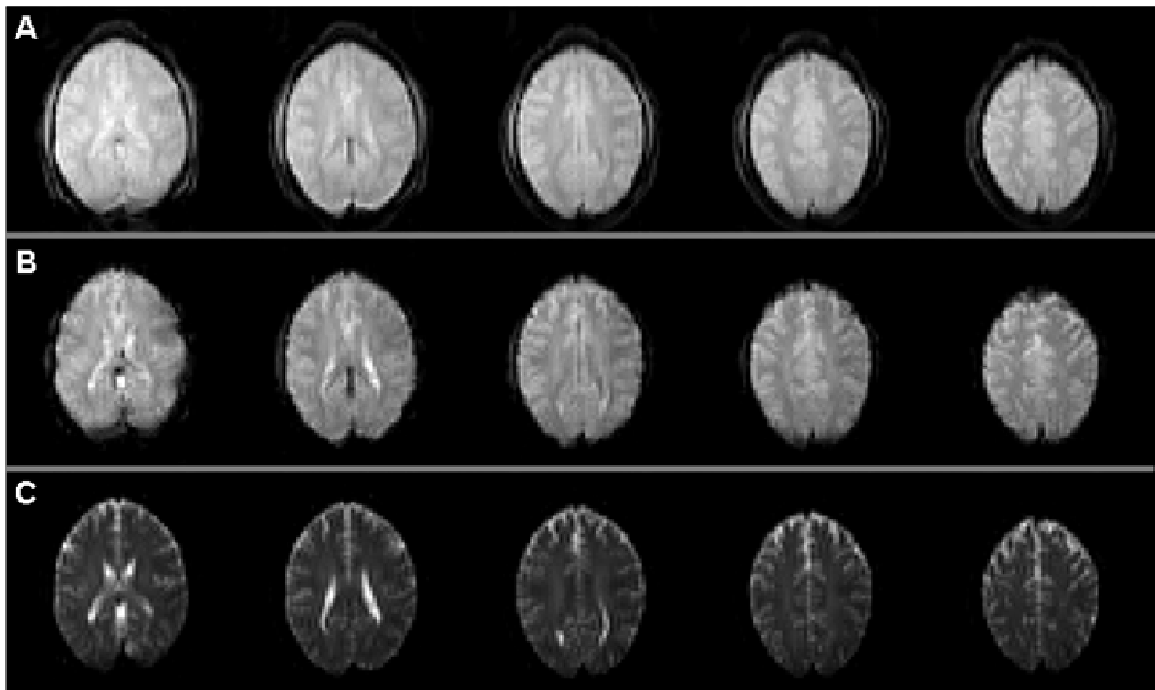


Fig. 4.7: Simultaneously acquired (A) control image for CBF, (B) GE BOLD and (C) SE BOLD data.

4.4.2 Results: Simultaneous Data Validation

Images for each contrast show the expected contrasts of minimal T2/T2* decay for echo 1, T2* weighting for echo 2 and T2 weighting for echo 3 (Fig. 4.7). Activation maps also reflect the expected trend for each contrast when a common statistical threshold (FDR < 0.05) is used for all contrasts. Specifically, CBF shows the most localized activation, reflecting the highest specificity and lowest sensitivity of the 3 contrasts (Fig 4.8). In contrast, GE BOLD shows the largest activation region, consistent with expectations of high sensitivity (Fig 4.8B). SE BOLD demonstrates a compromise of the features of CBF and GE BOLD. While GE BOLD is sensitive to extravascular susceptibility, SE BOLD is known to be dominated by intravascular sensitivity, consistent with more localized activation (Fig. 4.8C). Still, SE BOLD has higher SNR and is more sensitive than CBF. To control for different sensitivities of each contrast, CBF activation maps were generated using a threshold of $p < 0.05$ corrected for FDR and suprathreshold voxels were matched for GE and SE BOLD (Fig. 4.9).

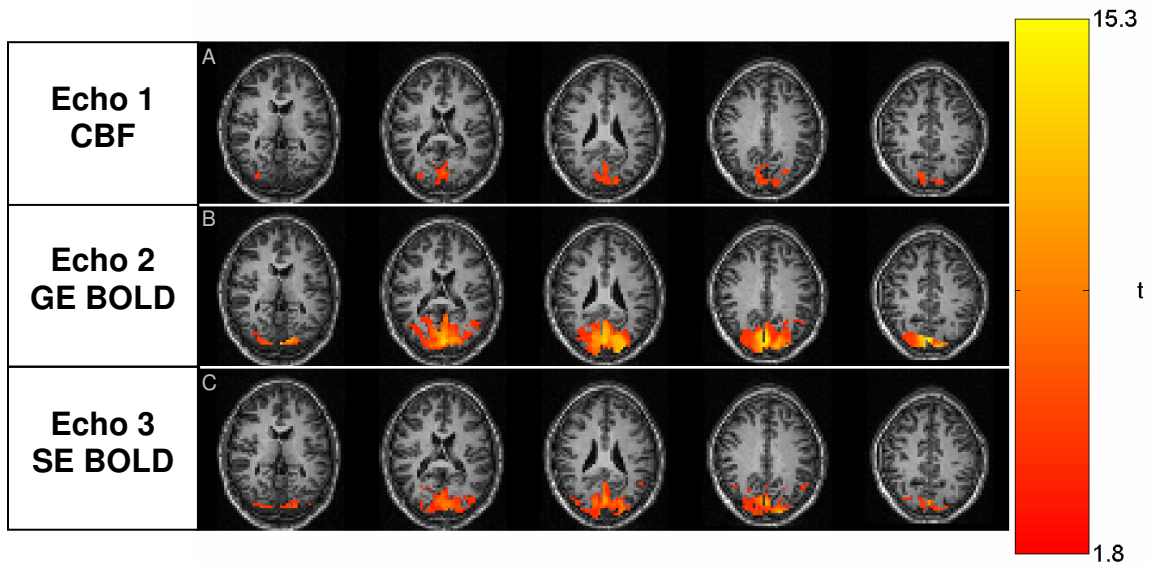


Fig. 4.8: Activation for subject 4 ($p < 0.05$ corrected for FDR) for all contrasts.

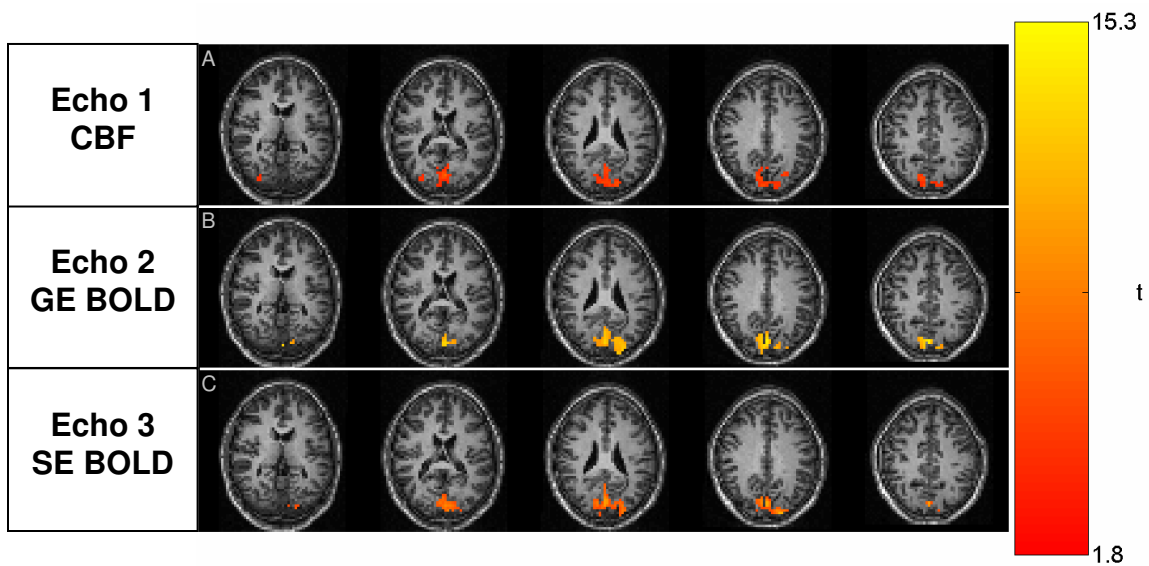


Fig. 4.9: Activation for subject 4 ($p < 0.05$ corrected for FDR) for (A) CBF and matching voxel counts for (B) SE and (C) GE BOLD.

Using the CBF localizer, time courses (Fig. 4.10) reflect similar forms for all three contrasts. As shown in Table 4.1, mean percent signal changes of 71.1%, 2.0% and 0.9% (71.1%, 3.8% and 2.0%) for CBF, GE BOLD and SE BOLD, respectively, when using the CBF localizer (matched voxel count localizer). Furthermore, resting CBF SNR is comparable for stand-alone SE and simultaneous sequences (Table 4.1). Quantified gray matter CBF is actually slightly higher for the simultaneous sequence (54.9 and 49.2 mL blood / 100 g tissue /min, respectively). $\Delta S/S_{\text{CONTROL}}$ images show good contrast between highly perfused gray matter and other structures for both sequences (Fig. 4.11).

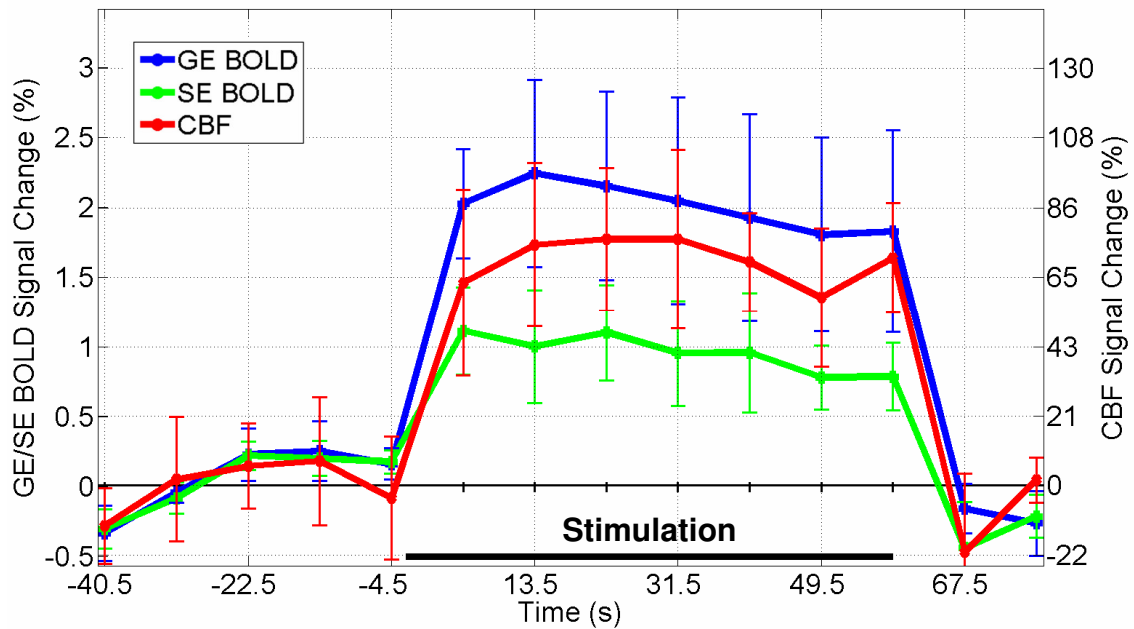


Fig. 4.10: Mean time course (across subjects) using CBF localizer.

Table 4.1: Relative task-related changes and inter-subject coefficient of variation for task-related data acquired with the simultaneous sequence

| Subject | CBF Localizer | | | Matched Voxel Localizer | |
|-----------------------------------|-----------------|--------------------|--------------------|-------------------------|--------------------|
| | % Δ CBF | % Δ GE BOLD | % Δ SE BOLD | % Δ GE BOLD | % Δ SE BOLD |
| 1 | 78.6 | 1.8 | 1 | 2.3 | 2 |
| 2 | 67.7 | 1.9 | 0.7 | 4.5 | 2.3 |
| 3 | 62.5 | 1.7 | 1.1 | 6.1 | 2.4 |
| 4 | 93.3 | 3.2 | 1.3 | 4.7 | 2.2 |
| 5 | 53.4 | 1.4 | 0.6 | 1.7 | 1 |
| Mean \pm S.D. | 71.1 \pm 15.4 | 2.0 \pm 0.7 | 0.9 \pm 0.3 | 3.8 \pm 1.8 | 2.0 \pm 0.6 |
| CV_{INTER} (%) | 21.7 | 33.6 | 32.4 | 47.7 | 30.1 |

Table 4.2: SNR and CBF_{GRAY} for stand-alone SE and simultaneous sequences

| Subject | Rest: Stand-alone SE | | Rest: Simultaneous | |
|-----------------------------------|------------------------------|---------------------------------|------------------------------|---------------------------------|
| | Sequence | | Sequence | |
| | % Δ S / $S_{CONTROL}$ | CBF_{GRAY} (ml / 100 g / min) | % Δ S / $S_{CONTROL}$ | CBF_{GRAY} (ml / 100 g / min) |
| 1 | 1 | 52.6 | 1 | 60.5 |
| 2 | 0.6 | 31.3 | 0.5 | 31.3 |
| 3 | 1.1 | 56.7 | 1 | 59.2 |
| 4 | 0.8 | 42.2 | 0.8 | 49.2 |
| 5 | 1.2 | 63.1 | 1.2 | 74.2 |
| Mean \pm S.D. | 0.92 \pm 0.24 | 49.2 \pm 12.6 | 0.91 \pm 0.27 | 54.9 \pm 15.9 |

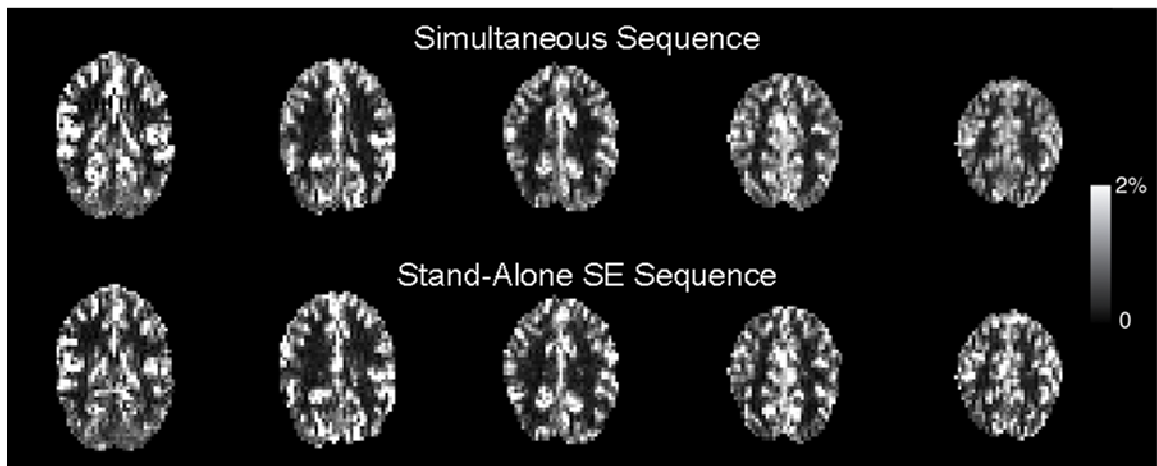


Fig. 4.11: $\Delta S/S_{CONTROL}$ for CBF data acquired with simultaneous sequence (top row) and stand-alone SE sequence (bottom row).

4.4.2.1 Reproducibility Assessment

Reproducibility assessment of relative signal changes reflects the proportion of standard deviation to the mean across subjects. As shown in Table 4.1, CV_{INTER} was relatively low for CBF (21.7%), moderate for SE BOLD (30.1%) and highest for GE BOLD (47.7%) when using the matched voxel count localizer. Similarly, CV_{INTER} was lowest for CBF (21.7%) but virtually the same for GE and SE BOLD (33.6 and 32.4%, respectively) when using the CBF localizer.

4.4.2.2 Linear Coupling Assessment

Linear regression of CBF and GE BOLD ($r=0.70$) and CBF and SE BOLD ($r=0.78$) using the CBF localizer were quite strong (Fig. 4.12A,B). Linear correlation between CBF and BOLD contrasts is weaker when using the matched voxel count localizer (CBF and GE BOLD: $r=0.66$, CBF and SE BOLD: $r=0.60$, Fig. 4.12D,E). However, SE and GE BOLD maintain similar coupling for this ROI relative to the CBF localizer ($r=0.72$ for both localizers, Fig. 4.12C,F). For contrast pairs that include CBF,

the CBF localizer improves linear coupling, but the choice of localizer does not impact extent of linear coupling for SE BOLD and GE BOLD (Table 4.3).

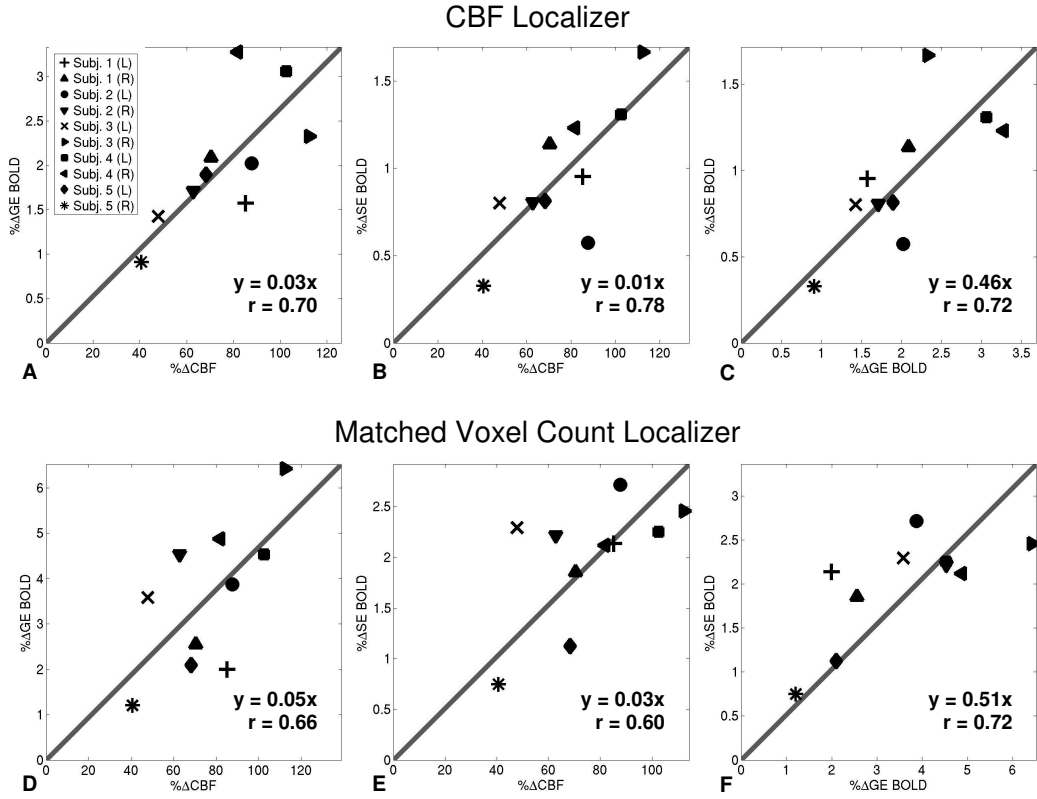


Fig. 4.12: Linear coupling reflects stronger fits for CBF localizer when fitting CBF and BOLD contrasts (A,B,D,E) but comparable fits for both localizers when fitting SE and GE BOLD contrasts.

Table 4.3: Relative to the matched voxel localizer, CBF localizer improves linear coupling for CBF\GE and CBF\SE.

| Localizer | Contrasts | r |
|-------------------|-----------|------|
| CBF Localizer | CBF\GE | 0.70 |
| Matched Localizer | CBF\GE | 0.66 |
| CBF Localizer | CBF\SE | 0.78 |
| Matched Localizer | CBF\SE | 0.60 |
| CBF Localizer | SE\GE | 0.72 |
| Matched Localizer | SE\GE | 0.72 |

4.4.2.3 Proximity to Large Vessels

Group mean Euclidean distance between center of gravity coordinates and the closest large vessel were significantly larger for CBF (4.7 ± 1.6 mm) than GE BOLD (2.4 ± 1.3 mm) ($p = 0.018$, two-tailed, Table 4.4). Although SE BOLD distances from large vessels (2.7 ± 1.2 mm) were comparable to those of GE BOLD, results were not significantly different from CBF ($p = 0.094$). Distances between center of gravity of activation and the closest large vessel were greater for CBF than GE BOLD for all subjects and SE BOLD for 4 of 5 subjects (Fig. 4.13).

Table 4.4: Proximity of center of gravity for CBF, GE BOLD and SE BOLD to closest large vessel.

| Subject | CBF Distance (mm) | GE BOLD Distance (mm) | SE BOLD Distance (mm) |
|-----------------------------------|--------------------------|------------------------------|------------------------------|
| 1 | 6.6 | 4.7 | 3.0 |
| 2 | 4.6 | 2.2 | 4.4 |
| 3 | 5.0 | 1.4 | 1.1 |
| 4 | 5.2 | 1.8 | 2.2 |
| 5 | 2.1 | 1.8 | 2.7 |
| Mean \pm S.D. | 4.7 ± 1.6 | 2.4 ± 1.3 | 2.7 ± 1.2 |

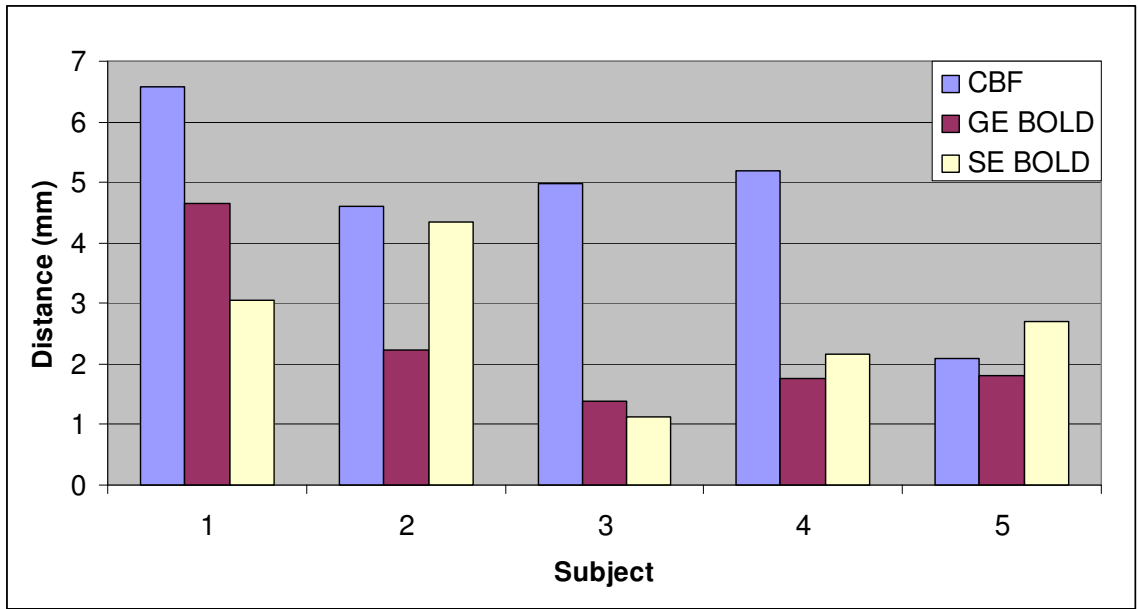


Fig. 4.13: Proximity of each contrast's center of gravity to the closest large vessel.

Percent overlap between active voxels and large vessels provides insight to the extent of large vessel bias for each contrast. As shown in Table 4.5, CBF had minimal overlap with large vessels (~1.9%), SE BOLD had moderate overlap (~16.7%) and GE BOLD had the most overlap (~29.7%). Due to inter-subject variation in percent overlap and the small number of subjects, two-tailed paired t-tests did not reveal significant differences between contrasts. However, one-tailed paired t-tests (based on the hypothesis that CBF, SE BOLD and GE BOLD have increasing overlap with macrovasculature) are significant (CBF < GE BOLD: $p=0.046$ and SE BOLD < GE BOLD: $p=0.046$).

Table 4.5: Percent overlap of active voxels with large vessels.

| Subject | CBF (%) | GE BOLD (%) | SE BOLD (%) |
|-----------------|---------------|-----------------|-----------------|
| 1 | 2.6 | 3.3 | 14.5 |
| 2 | 0.0 | 66.7 | 0.0 |
| 3 | 0.0 | 28.6 | 25.0 |
| 4 | 2.9 | 44.8 | 37.9 |
| 5 | 4.0 | 5.1 | 6.2 |
| Mean \pm S.D. | 1.9 \pm 1.8 | 29.7 \pm 26.9 | 16.7 \pm 15.1 |

4.5 Discussion

4.5.1 Two-Coil ASL and Stand-Alone SE Sequence Data Acquisition

Although two-coil CASL has been successfully used for several years, costly MR hardware and complicated implementation have limited its use as a routine perfusion imaging method. While the cost can be reduced by modifying the scanner's RF channel (115), this modification is complicated by the need to work with the manufacturer's RF system and possible limitation of RF on time. The SOC DDS presented in the first part of this chapter inexpensively addresses the need for an additional RF channel without requiring scanner hardware modification. The only connections with the scanner, the RF reference and TTL triggering signals, are available on most clinical scanners for device synchronization and fMRI stimulus triggering, respectively. In this regard, the proposed

CASL system provides an inexpensive and general solution, independent of the specific architecture of the scanner RF chain, making it affordable and portable.

Another advantage of using the DDS for the two-coil CASL system is its high level of integration and its relevance to recent MRI hardware development. Several studies have demonstrated the principles and feasibility of applying DDS to MR applications (116,135). Recent increase in demand for high performance communications applications have led to DDS integration of all necessary functional blocks into one SOC chip with higher phase/amplitude resolution and system clock. These developments improve signal quality and enable simplified hardware design of the CASL RF transmitter since many on-board discrete components can be omitted.

In addition, DDS also provides a programmable interface for setting the RF signal frequency, amplitude and phase. For example, the user can easily program the AD9954 via the 4-line serial configuration interface using PC parallel/serial port or MCU. This feature enables the user to remotely control the DDS via network for easy set-up and sequence debugging.

Furthermore, taking advantage of the rapidly growing semiconductor industry, several individual SOC DDS are being integrated into a single coin-sized chip. This can dramatically simplify the MR transmitter design. For example, the AD9959 integrates 4 independent 500MSPS DDS channels. This feature provides a potential application for parallel excitation which requires multiple RF channels, with independent control of RF phase and amplitude for each channel.

Generally, most MR applications require strong MR RF power amplifier with very fast RF on/off switching transient response. For example, peak B1 amplitudes

between 15 and 30 μT inside a whole-body transmit coil require a peak power of 15 to 20 KW on a typical 1.5 T whole-body MRI system (136). Because the RF power requirement is proportional to the square of the B_0 strength, higher field strength scanners require much stronger RF power. This will be a main consideration for two-coil CASL systems designed for simultaneous acquisition of multiple contrasts at higher fields; this application would be advantageous due to SE BOLD's increasing specificity to microvasculature at higher fields.

In addition, to minimize TE and TR, the duration of the RF excitation pulse should be as short as one millisecond. As a result, MR RF power amplifiers have a very fast RF on/off switching transient response. However, for the CASL application, instead of using an expensive MR RF power amplifier, an inexpensive 10 W mini-size communication RF power amplifier with RF ON/OFF control option is used for two reasons. First, for two-coil CASL application, due to the localization of labeling by a neck surface coil, the second proton RF channel only requires a relatively low output (several Watts) (112-114). Second, compared with several seconds of RF labeling, the 50 ms RF on and 1 μs RF off transient response time of this mini-size RF power amplifier is sufficiently short. In addition, unlike conventional MR RF amplifiers which are operated in a pulse mode, the labeling RF power amplifier described here works in a continuous wave mode, making it unlimited by the duty cycle.

The increased cost efficiency does not reduce data quality, as demonstrated by the resting and functional data presented in the first part of this chapter. However, gray matter CBF obtained in these experiments, while within the expected physiological range, is in the low range of values reported by previous studies (113,114). One potential

source of underestimation could be the increased number of slices compared to ASL studies with reduced coverage; a recent study demonstrated that increasing the number of slices could excite blood spins in transit and reduce CBF in dorsal slices (137). Future work will investigate the dependence on slice number and optimize the imaging parameters for more accurate CBF measurements.

4.5.2 Simultaneous Sequence Data Acquisition

This chapter mainly stresses a new pulse sequence that can simultaneously obtain CBF, SE BOLD and GE BOLD. Implementation of this approach is combined with a separate labeling coil to improve CBF SNR by virtually eliminating effects of MT. To validate that CBF data quality is preserved when acquiring multiple readouts, CBF data from the simultaneous sequence can be compared to data from the stand-alone SE sequence (125) during rest. CBF SNR in gray matter voxels is virtually the same for each sequence. Furthermore, $\Delta S/S_{\text{CONTROL}}$ of 0.91 – 0.92 % is comparable to other studies using a separate labeling coil (0.4-1.3% (108) and 0.8% (138)). Furthermore, gray matter CBF 49.2 and 54.9 ml/100 g/min for stand-alone SE and the simultaneous sequence, respectively, was within the expected range of 48-62 ml/100 g/min (108). Slightly higher CBF for the simultaneous sequence relative to the stand-alone SE sequence could relate to comparable $\Delta S/S_{\text{CONTROL}}$ with longer interslice time. The optimization of SE versus GE for ASL can be further explored in future studies as the tradeoff between T2*-weighted BOLD contamination and increased SNR of raw images enabled with significantly shorter TE in GE CBF requires empirical evaluation. As mentioned above, CBF underestimation is possible due to multiple slice acquisition.

Once CBF data quality was validated using resting state data, task-related activation and percent signal change were assessed. When using a common statistical threshold for all three contrasts, activation extent was least extensive for CBF, moderate for SE BOLD, and most extensive for GE BOLD. This is consistent with the reduced sensitivity of the CBF contrast relative to BOLD (139) as well as the suppression of macrovascular contributions in SE BOLD relative to GE BOLD (120-122). Furthermore, time courses reflect signal dynamics within the expected ranges for all subject and contrasts (32).

While inter-subject variation of relative signal changes has been shown to be lower for CBF than GE BOLD in one study (7) but lower for GE BOLD than CBF in another study(87), this is the first study comparing SE BOLD to these contrasts in this regard. Higher BOLD variability can be expected for two reasons. First, it reflects a mix of CBF, CBV and $CMRO_2$ while CBF serves as a more direct measurement. This explains why both GE BOLD and SE BOLD reflect higher inter-subject variability than CBF. Second, signal contribution from macrovasculature with large deoxyhemoglobin changes, such as draining veins, could lead to less stable signal changes. SE BOLD is less susceptible to macrovasculature (117), so this factor likely affects GE BOLD more than SE BOLD. This reasoning is consistent with reduced inter-subject variation of CBF relative to BOLD, and SE BOLD's reduced variation to GE BOLD for the matching voxel localizer. Furthermore, the consistent inter-subject variation between SE BOLD and GE BOLD when using a CBF localizer, which reduces or eliminates inclusion of large draining veins, suggests that the confounding effect of a physiological mix is a main factor of BOLD variation; increased GE BOLD relative to SE BOLD variation when

using the matched voxel localizer suggests that macrovasculature contributions, which are less problematic in SE BOLD, further exacerbate signal inconsistencies between subjects.

Using a CBF localizer to reduce macrovascular contribution for BOLD signal changes also improved linear coupling between BOLD and CBF contrasts. Previous studies have demonstrated linear coupling across subjects relating BOLD and CBF changes for visual stimuli similar to the paradigm used in this study (140,141). When a CBF localizer is used, GE and SE BOLD signal changes are linearly coupled with CBF to a high degree, likely due to CBF's reduced macrovascular contribution. However, linear coupling between CBF and each BOLD contrast is less prominent when using the matched voxel count localizer, likely because BOLD includes more macrovascular signal contribution. The improved linear coupling of the CBF localizer compared to the matched voxel localizer is consistent with previous findings that utilizing a CBF localizer can decrease variance across a subject pool for GE BOLD (87). In that study, Leontiev *et al.* also suppressed intravascular GE BOLD signal using diffusion gradients to improve inter-subject variation. The simultaneous sequence presented in this chapter could therefore be enhanced with the inclusion of bipolar diffusion gradients to further minimize intravascular contributions in the SE BOLD contrast as previous, single contrast approaches have demonstrated (122,142,143).

Signal contribution from large vessels likely plays a significant role in GE BOLD. To demonstrate this, each contrast's activation center of gravity was compared to the closest voxel with large vessel contribution. CBF activation was significantly farther

from large vessels than GE BOLD, suggesting that CBF can provide more accurate localization to neuronal activity. Although SE BOLD center of gravity coordinates were closer to large vessels relative to CBF, results were not significantly different. Applying the simultaneous sequence at higher magnetic fields, where the T2 of venous blood is substantially shorter minimizing its contribution to SE BOLD (117,123), could potentially show more similar localization of SE BOLD and CBF activation.

The simultaneous sequence presented in this chapter can be improved with the utilization of bipolar gradients to minimize intravascular BOLD contributions and implementation at higher magnetic fields. However, favorable results suggest that the image acquisition approach in its current form is well suited for clinical research in which repeated measures are utilized to study disease progression or treatment effects. With this goal in mind, future studies can evaluate inter-session variability within subjects to compare the three contrasts.

4.6 Conclusion

In the first part of this chapter, a system for performing two-coil CASL has been validated. Relative to previous systems using expensive MR RF instruments, the present design utilizes a low-cost SOC DDS and mini-size communication RF power amplifier to generate the labeling RF waveform without sacrificing RF performance, reducing the total cost to ~\$2500. Compared with a single RF channel approach, this design requires

minimal scanner hardware modifications, making the proposed system portable. Moreover, this design offers a programmable interface for easy sequence setup and debugging. The performance and ease of use has been validated experimentally, demonstrating its potential for widespread applications.

The main focus of this chapter enhances the two-coil system with the development of a new sequence that simultaneously acquires CBF, GE BOLD and SE BOLD. Images show expected weightings and activation maps are consistent with known qualities of each contrast. Next, this sequence can be applied to further compare intra- and inter-session reproducibility without inter-scan variability that confounds comparison using separate acquisitions for each contrast. Furthermore, scanning time can be significantly reduced relative to traditional protocols using separate acquisition of multiple contrasts.

CHAPTER 5

CONCLUSIONS

5.1 Problem Statement

As fMRI using BOLD contrast becomes more commonly applied to clinical and preclinical applications, the extent to which it conveys actual neuronal dynamics must be explored. As described in previous chapters, BOLD consists of a physiological mix of CBF, CBV and $CMRO_2$ so measuring and estimating these quantitative markers can provide additional information of neuronal dynamics. As recent research seeks to complement BOLD with these quantitative measures, techniques must be improved and assessed, including evaluating image quality and reproducibility in patient populations (Chapter 2), image analysis and modeling (Chapter 3) and image acquisition (Chapter 4).

5.2 Overview of Findings

While this work focuses on the application and development of quantitative fMRI in the context of rehabilitation studies, much of the work is applied to the healthy population. After evaluating the feasibility and improved reproducibility of CBF in

patients with central visual impairment (Chapter 2), subsequent work studies normal controls to illustrate method development. However, the improvements demonstrated by these methods are specifically designed for eventual utilization in patients. For instance, Chapter 3 enhances modeling of CBF, VASO and BOLD data acquired using a simultaneous sequence. While CBV data based on the VASO contrast has been demonstrated, CBV quantification based on this method has not been appropriate for rehabilitation studies because it has limited slice coverage, was confounded by the inflow of fresh blood and assumed CBV_{REST} . The model developed in Chapter 3 addresses each of these concerns and combines this approach with simultaneous acquisition of BOLD and CBF contrasts. These developments provide estimation of $CMRO_2$ with reduced assumptions.

Similarly, Chapter 4 develops image acquisition to facilitate future rehabilitation studies. Specifically, CBF is known to be less sensitive than BOLD which can lead to difficulties in detecting activation, particularly when neuronal activity is less prominent. Hemodynamic response to stimuli can be reduced in patients with visual field impairment because parts of the visual cortex can be considered “silent” or devoid of input from the retina or lateral geniculate nucleus. Therefore, it is important for all applications but necessary in patient populations for ASL to have improved SNR. A two-coil ASL system built at Emory University by Dr. Qin Xu is assessed and compared to standard ASL to demonstrate improved SNR and activation localization. Most of Chapter 4 focuses on the development and evaluation of a new pulse sequence that complements two-coil ASL with two types of BOLD contrast, SE and GE. The demonstrated feasibility of this approach will facilitate simultaneous CBF and multiple BOLD measurements in a variety

of contexts. Several examples of how this acquisition technique can be used to improve basic understanding of these contrast mechanisms are introduced in this dissertation. Specifically, inter-subject variation, linear coupling between contrasts and proximity of activation to large vessels are evaluated for a small group of subjects. The consideration of CBF and SE BOLD will be increasingly prominent as two-coil ASL becomes more readily available and studies move to higher static magnetic fields, which will improve SNR and increase SE BOLD's specificity to smaller vessels. Future work can benefit from simultaneous acquisition of the contrasts in patient populations; in particular, CBF and SE BOLD are more specific to smaller vessels and presumably have better reproducibility for repeated measures.

5.3 Future Implications

There are several motivating factors for the work presented in this dissertation. First, the demonstrated ability to acquire CBF and estimate $CMRO_2$ in patients with visual impairment provides a foundation for expansion of these methods in rehabilitation studies. Second, the presented approach for CBV quantification based on VASO, as well as incorporation of simultaneous CBF and BOLD measurement, seeks to combine developing fMRI analysis methods with applications that require relaxed assumptions. Finally, the improvement of CBF data quality and incorporation with more common measures in rehabilitation studies, SE and GE BOLD, facilitate expanded use in patient

studies. In summary, this dissertation presents significant improvement to quantitative fMRI methods for the application to patient populations and rehabilitation studies.

REFERENCES

1. Ogawa S, Tank DW, Menon R, Ellermann JM, Kim S, Merkle H, Ugurbil K. Intrinsic Signal Changes Accompanying Sensory Stimulation: Functional Brain Mapping with Magnetic Resonance Imaging. *PNAS* 1992;89(13):5951-5955.
2. Kwong KK, Belliveau JW, Chesler DA, Goldberg IE, Weisskoff RM, Poncelet BP, Kennedy DN, Hoppel BE, Cohen MS, Turner R, et al. Dynamic magnetic resonance imaging of human brain activity during primary sensory stimulation. *Proc Natl Acad Sci U S A* 1992;89(12):5675-5679.
3. Bandettini PA, Wong EC, Hinks RS, Tikofsky RS, Hyde JS. Time course EPI of human brain function during task activation. *Magn Reson Med* 1992;25(2):390-397.
4. Matthews PM, Jezzard P. Functional magnetic resonance imaging. *J Neurol Neurosurg Psychiatry* 2004;75(1):6-12.
5. Buckner Randy L, Bandettini Peter A, O'Craven Kathleen M, Savoy Robert L, Petersen Steven E, Raichle Marcus E, Rosen Bruce R. Detection of cortical activation during averaged single trials of a cognitive task using functional magnetic resonance imaging. *PNAS* 1996;93(25):14878-14883.
6. Friston KJ, Frith CD, Turner R, Frackowiak RSJ. Characterizing Evoked Hemodynamics with fMRI. *NeuroImage* 1995;2(2, Part 1):157-165.
7. Tjandra T, Brooks JC, Figueiredo P, Wise R, Matthews PM, Tracey I. Quantitative assessment of the reproducibility of functional activation measured with BOLD and MR perfusion imaging: implications for clinical trial design. *Neuroimage* 2005;27(2):393-401.
8. Ogawa S, Menon RS, Tank DW, Kim SG, Merkle H, Ellermann JM, Ugurbil K. Functional brain mapping by blood oxygenation level-dependent contrast magnetic resonance imaging. A comparison of signal characteristics with a biophysical model. *Biophys J* 1993;64(3):803-812.
9. Wong EC. Potential and pitfalls of arterial spin labeling based perfusion imaging techniques for MRI. *Functional MRI* 1999:63-69.
10. Edelman RR, Siewert B, Darby DG, Thangaraj V, Nobre AC, Mesulam MM, Warach S. Qualitative mapping of cerebral blood flow and functional localization with echo-planar MR imaging and signal targeting with alternating radio frequency. *Radiology* 1994;192(2):513-520.

11. Kwong KK, Chesler DA, Weisskoff RM, Donahue KM, Davis TL, Ostergaard L, Campbell TA, Rosen BR. MR perfusion studies with T1-weighted echo planar imaging. *Magn Reson Med* 1995;34(6):878-887.
12. Kim SG. Quantification of relative cerebral blood flow change by flow-sensitive alternating inversion recovery (FAIR) technique: application to functional mapping. *Magn Reson Med* 1995;34(3):293-301.
13. Yang Y, Frank JA, Hou L, Ye FQ, McLaughlin AC, Duyn JH. Multislice imaging of quantitative cerebral perfusion with pulsed arterial spin labeling. *Magn Reson Med* 1998;39(5):825-832.
14. Ye FQ, Mattay VS, Jezzard P, Frank JA, Weinberger DR, McLaughlin AC. Correction for vascular artifacts in cerebral blood flow values measured by using arterial spin tagging techniques. *Magn Reson Med* 1997;37(2):226-235.
15. Alsop DC, Detre JA. Reduced transit-time sensitivity in noninvasive magnetic resonance imaging of human cerebral blood flow. *J Cereb Blood Flow Metab* 1996;16(6):1236-1249.
16. Wong EC, Buxton RB, Frank LR. Quantitative imaging of perfusion using a single subtraction (QUIPSS and QUIPSS II). *Magn Reson Med* 1998;39(5):702-708.
17. Wong EC, Buxton RB, Frank LR. Quantitative perfusion imaging using arterial spin labeling. *Neuroimaging Clin N Am* 1999;9(2):333-342.
18. Hoge RD, Atkinson J, Gill B, Crelier GR, Marrett S, Pike GB. Linear coupling between cerebral blood flow and oxygen consumption in activated human cortex. *Proc Natl Acad Sci U S A* 1999;96(16):9403-9408.
19. Davis TL, Kwong KK, Weisskoff RM, Rosen BR. Calibrated functional MRI: mapping the dynamics of oxidative metabolism. *Proc Natl Acad Sci U S A* 1998;95(4):1834-1839.
20. Grubb RL, Jr., Raichle ME, Eichling JO, Ter-Pogossian MM. The effects of changes in PaCO₂ on cerebral blood volume, blood flow, and vascular mean transit time. *Stroke* 1974;5(5):630-639.
21. Hoge RD, Franceschini MA, Covolan RJ, Huppert T, Mandeville JB, Boas DA. Simultaneous recording of task-induced changes in blood oxygenation, volume, and flow using diffuse optical imaging and arterial spin-labeling MRI. *Neuroimage* 2005;25(3):701-707.
22. Lu H, Golay X, Pekar JJ, Van Zijl PC. Functional magnetic resonance imaging based on changes in vascular space occupancy. *Magn Reson Med* 2003;50(2):263-274.

23. Yang Y, Gu H, Stein EA. Simultaneous MRI acquisition of blood volume, blood flow, and blood oxygenation information during brain activation. *Magn Reson Med* 2004;52(6):1407-1417.
24. Gu H, Lu H, Ye FQ, Stein EA, Yang Y. Noninvasive quantification of cerebral blood volume in humans during functional activation. *Neuroimage* 2006;30(2):377-387.
25. Shulman RG, Hyder F, Rothman DL. Biophysical basis of brain activity: implications for neuroimaging. *Q Rev Biophys* 2002;35(3):287-325.
26. Hyder F. Neuroimaging with calibrated fMRI. *Stroke* 2004;35(11 Suppl 1):2635-2641.
27. Uludag K, Dubowitz DJ, Yoder EJ, Restom K, Liu TT, Buxton RB. Coupling of cerebral blood flow and oxygen consumption during physiological activation and deactivation measured with fMRI. *Neuroimage* 2004;23(1):148-155.
28. Xu G, Wu G, Xu Y, Li S-J. Decrease in CMRO₂ for Memory-Encoding Tasks in the Hippocampus of Mild Cognitive Impairment Subjects. *Proc Intl Soc Mag Reson Med* 2006:1108.
29. Chiarelli PA, Bulte DP, Piechnik S, Jezzard P. Sources of systematic bias in hypercapnia-calibrated functional MRI estimation of oxygen metabolism. *NeuroImage* 2007;34(1):35-43.
30. Yang Y, Gu H, Silbersweig DA, Stern E. Simultaneous perfusion and blood-oxygenation-level-dependent measurements using single-shot interleaved z-shim echo-planar imaging. *Magn Reson Med* 2005;53(5):1207-1211.
31. Kruger G, Kastrup A, Takahashi A, Glover GH. Simultaneous monitoring of dynamic changes in cerebral blood flow and oxygenation during sustained activation of the human visual cortex. *Neuroreport* 1999;10(14):2939-2943.
32. Lu H, Golay X, Pekar JJ, Van Zijl PC. Sustained poststimulus elevation in cerebral oxygen utilization after vascular recovery. *J Cereb Blood Flow Metab* 2004;24(7):764-770.
33. Lin A-L, Fox PT, Gao J-H. fMRI Measurement of CMRO₂ Using a Comprehensive Biophysical Model: Compared with PET. *Proc Intl Soc Mag Reson Med* 2006:539.
34. Gupta AK, Hutchinson PJ, Fryer T, Al-Rawi PG, Parry DA, Minhas PS, Kett-White R, Kirkpatrick PJ, Mathews JC, Downey S, Aigbirhio F, Clark J, Pickard JD, Menon DK. Measurement of brain tissue oxygenation performed using positron emission tomography scanning to validate a novel monitoring method. *J Neurosurg* 2002;96(2):263-268.

35. Heeger DJ, Huk AC, Geisler WS, Albrecht DG. Spikes versus BOLD: what does neuroimaging tell us about neuronal activity? *Nat Neurosci* 2000;3(7):631-633.
36. Rees G, Friston K, Koch C. A direct quantitative relationship between the functional properties of human and macaque V5. *Nat Neurosci* 2000;3(7):716-723.
37. Logothetis NK, Pauls J, Augath M, Trinath T, Oeltermann A. Neurophysiological investigation of the basis of the fMRI signal. *Nature* 2001;412(6843):150-157.
38. Smith AJ, Blumenfeld H, Behar KL, Rothman DL, Shulman RG, Hyder F. Cerebral energetics and spiking frequency: the neurophysiological basis of fMRI. *Proc Natl Acad Sci U S A* 2002;99(16):10765-10770.
39. Hyder F, Rothman DL, Shulman RG. Total neuroenergetics support localized brain activity: implications for the interpretation of fMRI. *Proc Natl Acad Sci U S A* 2002;99(16):10771-10776.
40. Sicard KM, Duong TQ. Effects of hypoxia, hyperoxia, and hypercapnia on baseline and stimulus-evoked BOLD, CBF, and CMRO₂ in spontaneously breathing animals. *Neuroimage* 2005;25(3):850-858.
41. Leibowitz HM, Krueger DE, Maunder LR, Milton RC, Kini MM, Kahn HA, Nickerson RJ, Pool J, Colton TL, Ganley JP, Loewenstein JI, Dawber TR. The Framingham Eye Study monograph: An ophthalmological and epidemiological study of cataract, glaucoma, diabetic retinopathy, macular degeneration, and visual acuity in a general population of 2631 adults, 1973-1975. *Surv Ophthalmol* 1980;24(Suppl):335-610.
42. Friedman DS, O'Colmain BJ, Munoz B, Tomany SC, McCarty C, de Jong PT, Nemesure B, Mitchell P, Kempen J. Prevalence of age-related macular degeneration in the United States. *Arch Ophthalmol* 2004;122(4):564-572.
43. Guez JE, Le Gargasson JF, Rigaudiere F, O'Regan JK. Is there a systematic location for the pseudo-fovea in patients with central scotoma? *Vision Res* 1993;33(9):1271-1279.
44. Cummings RW, Whittaker SG, Watson GR, Budd JM. Scanning characters and reading with a central scotoma. *Am J Optom Physiol Opt* 1985;62(12):833-843.
45. Cheung SH, Legge GE. Functional and cortical adaptations to central vision loss. *Vis Neurosci* 2005;22(2):187-201.
46. Timberlake GT, Mainster MA, Peli E, Augliere RA, Essock EA, Arend LE. Reading with a macular scotoma. I. Retinal location of scotoma and fixation area. *Invest Ophthalmol Vis Sci* 1986;27(7):1137-1147.

47. Fletcher DC, Schuchard RA. Preferred retinal loci relationship to macular scotomas in a low-vision population. *Ophthalmology* 1997;104(4):632-638.
48. Whittaker SG, Budd J, Cummings RW. Eccentric fixation with macular scotoma. *Invest Ophthalmol Vis Sci* 1988;29(2):268-278.
49. Nilsson UL, Frennesson C, Nilsson SE. Patients with AMD and a large absolute central scotoma can be trained successfully to use eccentric viewing, as demonstrated in a scanning laser ophthalmoscope. *Vision Res* 2003;43(16):1777-1787.
50. Sunness JS, Liu T, Yantis S. Retinotopic mapping of the visual cortex using functional magnetic resonance imaging in a patient with central scotomas from atrophic macular degeneration. *Ophthalmology* 2004;111(8):1595-1598.
51. Ramachandran VS, Hirstein W. The perception of phantom limbs. The D. O. Hebb lecture. *Brain* 1998;121 (Pt 9):1603-1630.
52. Pons TP, Garraghty PE, Ommaya AK, Kaas JH, Taub E, Mishkin M. Massive cortical reorganization after sensory deafferentation in adult macaques. *Science* 1991;252(5014):1857-1860.
53. Merzenich MM, Nelson RJ, Stryker MP, Cynader MS, Schoppmann A, Zook JM. Somatosensory cortical map changes following digit amputation in adult monkeys. *J Comp Neurol* 1984;224(4):591-605.
54. Kaas JH, Krubitzer LA, Chino YM, Langston AL, Polley EH, Blair N. Reorganization of retinotopic cortical maps in adult mammals after lesions of the retina. *Science* 1990;248(4952):229-231.
55. Gilbert CD, Wiesel TN. Receptive field dynamics in adult primary visual cortex. *Nature* 1992;356(6365):150-152.
56. Gilbert CD, Hirsch JA, Wiesel TN. Lateral interactions in visual cortex. *Cold Spring Harb Symp Quant Biol* 1990;55:663-677.
57. Gilbert CD. Adult cortical dynamics. *Physiol Rev* 1998;78(2):467-485.
58. Darian-Smith C, Gilbert CD. Topographic reorganization in the striate cortex of the adult cat and monkey is cortically mediated. *J Neurosci* 1995;15(3 Pt 1):1631-1647.
59. Horton JC, Hocking DR. Monocular core zones and binocular border strips in primate striate cortex revealed by the contrasting effects of enucleation, eyelid suture, and retinal laser lesions on cytochrome oxidase activity. *J Neurosci* 1998;18(14):5433-5455.

60. Murakami I, Komatsu H, Kinoshita M. Perceptual filling-in at the scotoma following a monocular retinal lesion in the monkey. *Vis Neurosci* 1997;14(1):89-101.
61. Baker CI, Peli E, Knouf N, Kanwisher NG. Reorganization of visual processing in macular degeneration. *J Neurosci* 2005;25(3):614-618.
62. Smirnakis SM, Brewer AA, Schmid MC, Tolias AS, Schuz A, Augath M, Inhoffen W, Wandell BA, Logothetis NK. Lack of long-term cortical reorganization after macaque retinal lesions. *Nature* 2005;435(7040):300-307.
63. Calford MB, Chino YM, Das A, Eysel UT, Gilbert CD, Heinen SJ, Kaas JH, Ullman S. Neuroscience: rewiring the adult brain. *Nature* 2005;438(7065):E3; discussion E3-4.
64. Eysel UT. Functional reconnections without new axonal growth in a partially denervated visual relay nucleus. *Nature* 1982;299(5882):442-444.
65. Das A, Gilbert CD. Receptive field expansion in adult visual cortex is linked to dynamic changes in strength of cortical connections. *J Neurophysiol* 1995;74(2):779-792.
66. Darian-Smith C, Gilbert CD. Axonal sprouting accompanies functional reorganization in adult cat striate cortex. *Nature* 1994;368(6473):737-740.
67. Calford MB, Wright LL, Metha AB, Taglianetti V. Topographic plasticity in primary visual cortex is mediated by local corticocortical connections. *J Neurosci* 2003;23(16):6434-6442.
68. Council NAE. Vision Research, a National Plan. Bethesda, MD: NIH. Volume 93; 1993.
69. Flannery JG, Farber DB, Bird AC, Bok D. Degenerative changes in a retina affected with autosomal dominant retinitis pigmentosa. *Invest Ophthalmol Vis Sci* 1989;30(2):191-211.
70. Santos A, Humayun MS, de Juan E, Jr., Greenburg RJ, Marsh MJ, Klock IB, Milam AH. Preservation of the inner retina in retinitis pigmentosa. A morphometric analysis. *Arch Ophthalmol* 1997;115(4):511-515.
71. Pardue MT, Ball SL, Phillips MJ, Faulkner AE, Walker TA, Chow AY, Peachey NS. Status of the feline retina 5 years after subretinal implantation. *J Rehabil Res Dev* 2006;43(6):723-732.
72. Pardue MT, Phillips MJ, Hanzlicek B, Yin H, Chow AY, Ball SL. Neuroprotection of photoreceptors in the RCS rat after implantation of a subretinal implant in the superior or inferior retina. *Adv Exp Med Biol* 2006;572:321-326.

73. Chow AY, Chow VY, Packo KH, Pollack JS, Peyman GA, Schuchard R. The artificial silicon retina microchip for the treatment of vision loss from retinitis pigmentosa. *Arch Ophthalmol* 2004;122(4):460-469.
74. Pardue MT, Stubbs EB, Jr., Perlman JI, Narfstrom K, Chow AY, Peachey NS. Immunohistochemical studies of the retina following long-term implantation with subretinal microphotodiode arrays. *Exp Eye Res* 2001;73(3):333-343.
75. Chow AY, Chow VY. Subretinal electrical stimulation of the rabbit retina. *Neurosci Lett* 1997;225(1):13-16.
76. Chow AY, Pardue MT, Perlman JI, Ball SL, Chow VY, Hetling JR, Peyman GA, Liang C, Stubbs EB, Jr., Peachey NS. Subretinal implantation of semiconductor-based photodiodes: durability of novel implant designs. *J Rehabil Res Dev* 2002;39(3):313-321.
77. Chow AY, Pardue MT, Chow VY, Peyman GA, Liang C, Perlman JI, Peachey NS. Implantation of silicon chip microphotodiode arrays into the cat subretinal space. *IEEE Trans Neural Syst Rehabil Eng* 2001;9(1):86-95.
78. Schuchard R, Dagnelie G, Pollack JS, Kotowski J, Chow AY. Evaluation of the ASR Device® for the Treatment of Vision Loss From Retinitis Pigmentosa: Phase II Study. 2007; Fort Lauderdale, FL.
79. Laatsch L, Krisky C. Changes in fMRI activation following rehabilitation of reading and visual processing deficits in subjects with traumatic brain injury. *Brain Inj* 2006;20(13-14):1367-1375.
80. Marshall RS, Ferrera JJ, Barnes A, Xian Z, O'Brien KA, Chmayssani M, Hirsch J, Lazar RM. Brain activity associated with stimulation therapy of the visual borderzone in hemianopic stroke patients. *Neurorehabil Neural Repair* 2008;22(2):136-144.
81. Small SL, Flores DK, Noll DC. Different neural circuits subserve reading before and after therapy for acquired dyslexia. *Brain Lang* 1998;62(2):298-308.
82. Schumacher EH, Jacko JA, Primo SA, Main KL, Moloney KP, Kinzel EN, Ginn J. Reorganization of visual processing is related to eccentric viewing in patients with macular degeneration. *Restor Neurol Neurosci* 2008;26(4-5):391-402.
83. Alsop DC, Detre JA. Multisection cerebral blood flow MR imaging with continuous arterial spin labeling. *Radiology* 1998;208(2):410-416.
84. Wang J, Alsop DC, Song HK, Maldjian JA, Tang K, Salvucci AE, Detre JA. Arterial transit time imaging with flow encoding arterial spin tagging (FEAST). *Magn Reson Med* 2003;50(3):599-607.

85. Genovese CR, Lazar NA, Nichols T. Thresholding of statistical maps in functional neuroimaging using the false discovery rate. *Neuroimage* 2002;15(4):870-878.
86. Kim SG, Rostrup E, Larsson HB, Ogawa S, Paulson OB. Determination of relative CMRO₂ from CBF and BOLD changes: significant increase of oxygen consumption rate during visual stimulation. *Magn Reson Med* 1999;41(6):1152-1161.
87. Leontiev O, Buxton RB. Reproducibility of BOLD, perfusion, and CMRO₂ measurements with calibrated-BOLD fMRI. *Neuroimage* 2007;35(1):175-184.
88. Schwarzbauer C. Simultaneous detection of changes in perfusion and BOLD contrast. *NMR Biomed* 2000;13(1):37-42.
89. Donahue MJ, Lu H, Jones CK, Edden RA, Pekar JJ, van Zijl PC. Theoretical and experimental investigation of the VASO contrast mechanism. *Magn Reson Med* 2006;56(6):1261-1273.
90. Kastrup A, Kruger G, Neumann-Haefelin T, Glover GH, Moseley ME. Changes of cerebral blood flow, oxygenation, and oxidative metabolism during graded motor activation. *Neuroimage* 2002;15(1):74-82.
91. Hoge RD, Atkinson J, Gill B, Crelier GR, Marrett S, Pike GB. Investigation of BOLD signal dependence on cerebral blood flow and oxygen consumption: the deoxyhemoglobin dilution model. *Magn Reson Med* 1999;42(5):849-863.
92. Lin AL, Fox PT, Yang Y, Lu H, Tan LH, Gao JH. Time-dependent correlation of cerebral blood flow with oxygen metabolism in activated human visual cortex as measured by fMRI. *Neuroimage* 2009;44(1):16-22.
93. Wang J, Aguirre GK, Kimberg DY, Roc AC, Li L, Detre JA. Arterial spin labeling perfusion fMRI with very low task frequency. *Magn Reson Med* 2003;49(5):796-802.
94. Lazar NA, Luna B, Sweeney JA, Eddy WF. Combining brains: a survey of methods for statistical pooling of information. *Neuroimage* 2002;16(2):538-550.
95. Gu H, Stein EA, Yang Y. Nonlinear responses of cerebral blood volume, blood flow and blood oxygenation signals during visual stimulation. *Magn Reson Imaging* 2005;23(9):921-928.
96. Rodbard D. Statistical quality control and routine data processing for radioimmunoassays and immunoradiometric assays. *Clin Chem* 1974;20(10):1255-1270.
97. Chiarelli PA, Bulte DP, Wise R, Gallichan D, Jezard P. A calibration method for quantitative BOLD fMRI based on hyperoxia. *Neuroimage* 2007;37(3):808-820.

98. Detre JA, Wang J. Technical aspects and utility of fMRI using BOLD and ASL. *Clinical Neurophysiology* 2002;113(5):621-634.
99. Lu H, Clingman C, Golay X, van Zijl PC. Determining the longitudinal relaxation time (T1) of blood at 3.0 Tesla. *Magn Reson Med* 2004;52(3):679-682.
100. Wu WC, Buxton RB, Wong EC. Vascular space occupancy weighted imaging with control of residual blood signal and higher contrast-to-noise ratio. *IEEE Trans Med Imaging* 2007;26(10):1319-1327.
101. Lu H, Law M, Johnson G, Ge Y, van Zijl PC, Helpert JA. Novel approach to the measurement of absolute cerebral blood volume using vascular-space-occupancy magnetic resonance imaging. *Magn Reson Med* 2005;54(6):1403-1411.
102. Rostrup E, Knudsen GM, Law I, Holm S, Larsson HB, Paulson OB. The relationship between cerebral blood flow and volume in humans. *Neuroimage* 2005;24(1):1-11.
103. Lu H, van Zijl PC. Experimental measurement of extravascular parenchymal BOLD effects and tissue oxygen extraction fractions using multi-echo VASO fMRI at 1.5 and 3.0 T. *Magn Reson Med* 2005;53(4):808-816.
104. Chanarin I, Brozovic M, Tidmarsh E, Waters D. *Blood and its disease*. New York: Churchill Livingstone; 1984.
105. Besarab A, Bolton WK, Browne JK, Egrie JC, Nissenson AR, Okamoto DM, Schwab SJ, Goodkin DA. The effects of normal as compared with low hematocrit values in patients with cardiac disease who are receiving hemodialysis and epoetin. *N Engl J Med* 1998;339(9):584-590.
106. Cirillo M, Laurenzi M, Trevisan M, Stamler J. Hematocrit, blood pressure, and hypertension. The Gubbio Population Study. *Hypertension* 1992;20(3):319-326.
107. Eykyn TR, Payne GS, Leach MO. Inversion recovery measurements in the presence of radiation damping and implications for evaluating contrast agents in magnetic resonance. *Phys Med Biol* 2005;50(22):N371-376.
108. Talagala SL, Ye FQ, Ledden PJ, Chesnick S. Whole-brain 3D perfusion MRI at 3.0 T using CASL with a separate labeling coil. *Magn Reson Med* 2004;52(1):131-140.
109. van Zijl PC, Eleff SM, Ulatowski JA, Oja JM, Ulug AM, Traystman RJ, Kauppinen RA. Quantitative assessment of blood flow, blood volume and blood oxygenation effects in functional magnetic resonance imaging. *Nat Med* 1998;4(2):159-167.
110. Barbier EL, Lamalle L, Decors M. Methodology of brain perfusion imaging. *J Magn Reson Imaging* 2001;13(4):496-520.

111. Detre JA, Leigh JS, Williams DS, Koretsky AP. Perfusion imaging. *Magn Reson Med* 1992;23(1):37-45.
112. Zaharchuk G, Ledden PJ, Kwong KK, Reese TG, Rosen BR, Wald LL. Multislice perfusion and perfusion territory imaging in humans with separate label and image coils. *Magn Reson Med* 1999;41(6):1093-1098.
113. Talagala SL, Ye FQ, Ledden PJ, Chesnick S. Whole-brain 3D perfusion MRI at 3.0 T using CASL with a separate labeling coil. *Magn Reson Med* 2004;52(1):131-140.
114. Mildner T, Trampel R, Moller HE, Schafer A, Wiggins CJ, Norris DG. Functional perfusion imaging using continuous arterial spin labeling with separate labeling and imaging coils at 3 T. *Magn Reson Med* 2003;49(5):791-795.
115. Papadakis N, Devonshire I, He J, Mayhew J. Continuous arterial spin labeling with separate labeling and imaging coils: implementation using a single RF channel and amplifier. *Magn Reson Eng B* 2006;29(3):145-152.
116. Jiang Y, Jiang Y, Tao H, Li G. A complete digital radio-frequency source for nuclear magnetic resonance spectroscopy. *Rev Sci Instrum* 2002;73(9):3329-3331.
117. Duong TQ, Yacoub E, Adriany G, Hu X, Ugurbil K, Vaughan JT, Merkle H, Kim SG. High-resolution, spin-echo BOLD, and CBF fMRI at 4 and 7 T. *Magn Reson Med* 2002;48(4):589-593.
118. Norris DG, Zysset S, Mildner T, Wiggins CJ. An investigation of the value of spin-echo-based fMRI using a Stroop color-word matching task and EPI at 3 T. *Neuroimage* 2002;15(3):719-726.
119. Thulborn KR, Chang SY, Shen GX, Voyvodic JT. High-resolution echo-planar fMRI of human visual cortex at 3.0 tesla. *NMR Biomed* 1997;10(4-5):183-190.
120. Boxerman JL, Hamberg LM, Rosen BR, Weisskoff RM. MR contrast due to intravascular magnetic susceptibility perturbations. *Magn Reson Med* 1995;34(4):555-566.
121. Kennan RP, Zhong J, Gore JC. Intravascular susceptibility contrast mechanisms in tissues. *Magn Reson Med* 1994;31(1):9-21.
122. Parkes LM, Schwarzbach JV, Bouts AA, Deckers RH, Pullens P, Kerskens CM, Norris DG. Quantifying the spatial resolution of the gradient echo and spin echo BOLD response at 3 Tesla. *Magn Reson Med* 2005;54(6):1465-1472.
123. Lee SP, Silva AC, Ugurbil K, Kim SG. Diffusion-weighted spin-echo fMRI at 9.4 T: microvascular/tissue contribution to BOLD signal changes. *Magn Reson Med* 1999;42(5):919-928.

124. Yacoub E, Shmuel A, Pfeuffer J, Van De Moortele PF, Adriany G, Andersen P, Vaughan JT, Merkle H, Ugurbil K, Hu X. Imaging brain function in humans at 7 Tesla. *Magn Reson Med* 2001;45(4):588-594.
125. Xu Q, Glielmi C, Zhou L, Choi K, Hu X. An inexpensive and programmable RF transmitter setup for two-coil CASL. *Concepts in Magnetic Resonance Part B (Magnetic Resonance Engineering)* 2008;33B(4):228-235.
126. Yang Y, Gu H, Zhan W, Xu S, Silbersweig DA, Stern E. Simultaneous perfusion and BOLD imaging using reverse spiral scanning at 3T: characterization of functional contrast and susceptibility artifacts. *Magn Reson Med* 2002;48(2):278-289.
127. Dixon WT, Du LN, Faul DD, Gado M, Rossnick S. Projection angiograms of blood labeled by adiabatic fast passage. *Magn Reson Med* 1986;3(3):454-462.
128. Ye FQ, Smith AM, Yang Y, Duyn J, Mattay VS, Ruttimann UE, Frank JA, Weinberger DR, McLaughlin AC. Quantitation of regional cerebral blood flow increases during motor activation: a steady-state arterial spin tagging study. *Neuroimage* 1997;6(2):104-112.
129. Herscovitch P, Raichle M. What is the correct value for the brain-blood partition coefficient for water? *J Cereb Blood Flow Metab* 1985;5:65-69.
130. Ye FQ, Mattay VS, Jezzard P, Frank JA, Weinberger DR, McLaughlin AC. Correction for vascular artifacts in cerebral blood flow values measured by using arterial spin tagging techniques. *Magn Reson Med* 1997;37(2):226-235.
131. Duyn JH, Frank JA, Ramsey NR, Mattay VS, Sexton RH. Effects of large vessels in functional magnetic resonance imaging at 1.5 T. *Int J Imaging Sys Technol* 1995;6:245-252.
132. Lee AT, Glover GH, Meyer CH. Discrimination of large venous vessels in time-course spiral blood-oxygen-level-dependent magnetic-resonance functional neuroimaging. *Magn Reson Med* 1995;33(6):745-754.
133. Olman CA, Inati S, Heeger DJ. The effect of large veins on spatial localization with GE BOLD at 3 T: Displacement, not blurring. *Neuroimage* 2007;34(3):1126-1135.
134. P. M, G. MP. *NMR imaging in biomedicine*. New York: Academic Press; 1986. p 313.
135. Momo F, Sotgiu A, Testa L, Zanin A. Digital frequency synthesizers for nuclear magnetic resonance spectroscopy. *Rev Sci Instrum* 1994;65(10):3291-3292.
136. Edelman RR HJ, Zlatkin MB, Cruess JV. *Clinical Magnetic Resonance Imaging*. Philadelphia: Elsevier; 2005. p 125.

137. Borogovac A KJ, Brown TR, Asliani L. Dependence of Functional ASL MRI Signal on Number of Slice Acquisitions. 2008; Toronto. Proceedings of the 16th Annual Meeting of ISMRM. p 3577.
138. Mildner T, Trampel R, Moller HE, Schafer A, Wiggins CJ, Norris DG. Functional perfusion imaging using continuous arterial spin labeling with separate labeling and imaging coils at 3 T. *Magn Reson Med* 2003;49(5):791-795.
139. Aguirre GK, Detre JA, Zarahn E, Alsop DC. Experimental design and the relative sensitivity of BOLD and perfusion fMRI. *Neuroimage* 2002;15(3):488-500.
140. Hoge RD, Atkinson J, Gill B, Crelier GR, Marrett S, Pike GB. Stimulus-dependent BOLD and perfusion dynamics in human V1. *Neuroimage* 1999;9(6 Pt 1):573-585.
141. Zhu XH, Kim SG, Andersen P, Ogawa S, Ugurbil K, Chen W. Simultaneous oxygenation and perfusion imaging study of functional activity in primary visual cortex at different visual stimulation frequency: quantitative correlation between BOLD and CBF changes. *Magn Reson Med* 1998;40(5):703-711.
142. Jochimsen TH, Norris DG, Mildner T, Moller HE. Quantifying the intra- and extravascular contributions to spin-echo fMRI at 3 T. *Magn Reson Med* 2004;52(4):724-732.
143. Duong TQ, Yacoub E, Adriany G, Hu X, Ugurbil K, Kim SG. Microvascular BOLD contribution at 4 and 7 T in the human brain: gradient-echo and spin-echo fMRI with suppression of blood effects. *Magn Reson Med* 2003;49(6):1019-1027.